Development and Optimization of Sodium Magnetic Resonance Advanced Techniques in the *In Vivo* Assessment of Human Musculoskeletal Tissue

DEVELOPMENT AND OPTIMIZATION OF SODIUM MAGNETIC RESONANCE ADVANCED TECHNIQUES IN THE *IN VIVO* ASSESSMENT OF HUMAN MUSCULOSKELETAL TISSUE

BY

ALIREZA AKBARI, M.Eng.

A THESIS

SUBMITTED TO THE SCHOOL OF BIOMEDICAL ENGINEERING

AND THE SCHOOL OF GRADUATE STUDIES

OF MCMASTER UNIVERSITY

IN PARTIAL FULFILMENT OF THE REQUIREMENTS

FOR THE DEGREE OF

DOCTOR OF PHILOSOPHY

Doctor of Philosophy (2016) McMaster University

(School of Biomedical Engineering) Hamilton, Ontario, Canada

TITLE:	Development and Optimization of Sodium Magnetic Resonance Advanced Techniques in the *In Vivo* Assessment of Human Musculoskeletal Tissue
AUTHOR:	Alireza Akbari M.Eng., (Electrical and Computer Engineering) McMaster University, Hamilton, Canada
SUPERVISOR:	Dr. Michael D. Noseworthy
NUMBER OF PAGES:	xxvi, 120

Abstract

Sodium (^{23}Na) plays a pivotal role in cellular homeostasis throughout all life forms. In the human body it has a plethora of physiological functions including regulation of bodily fluids, muscle contraction, neuronal transmission, and connective tissue integrity. The ^{23}Na nucleus can be visualized using magnetic resonance imaging (MRI) because it has spin 3/2 and is the 100% naturally abundant isotope of sodium. However, unlike hydrogen (^{1}H), the nucleus of choice for MRI scanning, ^{23}Na MR clinical applications are almost non-existent, even though it is the second most MR visible nucleus after ^{1}H. This is primarily because ^{23}Na requires its own customized hardware (i.e. radiofrequency RF coil) and software (i.e. pulse sequence/acquisition and image reconstruction techniques). Additionally, ^{23}Na MR is challenging because of significantly lower signal-to-noise ratio (SNR), which translates to a requirement for lengthy scans and lower spatial resolution. Hence, development and optimization of ^{23}Na MR acquisition techniques is an ongoing subject of research. In this dissertation development and optimization of approaches that exploit sodium as a biomarker for musculoskeletal health are described. Specifically, discussions of advanced ^{23}Na MR techniques fall into two main categories: magnetic resonance imaging (MRI) and spectroscopy (MRS).

The work first explored development of a MRI compatible electrical muscle stimulation (EMS) system that could be used as a consistent alternative to voluntary muscle contraction. A variety of MRI methods were used to confirm the similarity between stimulation and voluntary activation of muscles of the lower leg. In a follow-up study quantum filtered (QF) ^{23}Na MRS was used to assess dynamic changes in skeletal muscle before, during and following voluntary exercise. Total (single quantum filtered, SQF) and bound intracellular sodium (triple quantum filtered, TQF) were measured in 9 healthy subjects with a 12s temporal resolution. Total sodium (SQF) significantly increased 4% ($p < 0.01$), while bound intracellular sodium content decreased 7% ($p < 0.01$) with exercise. Both returned to baseline following exercise; TQF after a few seconds and SQF after approximately 12 minutes ($p < 0.05$). In a preliminary study the MR-compatible EMS unit demonstrated similar QF ^{23}Na MRS results.

Sodium MR imaging, like typical ^{1}H-MRI scanning, can be performed by rasterizing k-space. However, this approach is both temporally and SNR inefficient. Therefore newer optimized ^{23}Na MRI pulse sequence approaches have been developed. The cost-benefit of extending the acquisition window length in terms of SNR gain and blurring in the *in vivo* ^{23}Na MRI of the human knee was explored in 3 healthy subjects using a density adapted 3-dimensional projection reconstruction (DA-3DPR) sequence. Mean SNR doubled when the acquisition window was increased from 4 to 25ms. Concurrently, the FWHM, as a measure of cartilage blurring, increased by only 1$\pm$0mm across three different sections of articular cartilage. In a second imaging experiment, a pseudo-random 3D non-Cartesian k-space acquisition scheme for ^{23}Na MRI was introduced. This scheme was highly effective in minimizing the aliasing

artifacts leading to 9 times less number of shots required to cover k-space compared to a fully-sampled acquisition scheme. Hence, this resulted in a 9-fold reduction in scan time to cover k-space. Images of a resolution phantom and healthy human knee, with 3mm isotropic resolution (zero padded to 1mm isotropic resolution), were reconstructed using a non-uniform fast Fourier transform (NUFFT).

Acknowledgements

It is interesting to realize that although this section takes only a couple of pages of the entire my PhD dissertation it actually makes up 99% of the work. It is true that I was the main player. However, it would be selfish and ignorant if I claim I have achieved this point without an incredibly dedicated support team that has always stood behind me every step of the way.

There are many people who deserve to be thanked here and I would like to start with thanking my supervisor Dr. Michael D. Noseworthy. He has always been exceptionally encouraging, flexible, and supportive throughout my graduate training. It is difficult to classify him as merely as a supervisor for he treats students like colleagues and seeks to foster the development of confidence and ability to pursue independent ideas. He has been more than a prefect fit for what I could have asked for in a supervisor.

I also would like to thank my supervisory committee: Drs. Alex Bain, Hubert de Bruin, and Dinesh Kumbhare. Each one of them offered me with their years of knowledge and expertise in order to perfect my PhD work. Dr. Bain helped me with understanding quantum physics; thanks for the guidance especially the unique tutorial on that topic. Dr. de Bruin shared his expertise on understanding muscle stimulation. Dr. Kumbhare provided many discussion sessions on understanding

muscle physiology and how to efficiently conduct muscle stimulation. Thank you all.

I would like to thank the Senior Scientific Research Officer, Norm Konyer, at St. Joseph's IRC. He was my teacher and mentor for building MR radiofrequency coils. The knowledge I gained from him has become an indispensable skill and integral part of my career in MR world.

I do not know how to thank my life mentor, Dr. Reza Nejat. In the past fourteen years of my life, he has been one of the most influential people by giving me fatherly advice whenever I needed it. His mentorship has been beyond academic matters, he has nurtured my personal life and character. It would not be an exaggerated statement if I say he has been a complementary dad to me. Thanks for your continued unsparing support for every step of the way.

Let me not forget to thank all my great friends a long the way for being there for me whenever I needed a break away from research. They definitely made my graduate life rich and full of fun times. Special thanks go to one of my best friends Amin Hosseini. Amin, it has been nearly a decade of friendship, dude! So much fun and unforgettable travels and trips we have had besides school. The discussions and contemplations on life as a bigger picture have been extremely valuable in terms of finding who we are and the life's purpose and its philosophy.

Although Ali Fatemi-Ardekani left the IRC when I joined the lab he gave me a very valuable advice: "Take the ownership of your research"! I have kept that in my mind at all times during my graduate training. It helped me a lot. Thank you Ali!

Last, but definitely not least, I would like to thank my lovely family. My parents and siblings' tremendous care, support, and encouragement kept me steadfast on the track. A very special thanks goes to my lovely sister Roya. She was the one who

brought me here to Canada giving me an opportunity to thrive. Today, I can proudly tell her that I did not waste the opportunity she provided me. Thanks a lot!

Alireza Akbari

Hamilton, Ontario

July 18, 2016

"Each small candle lights a corner of the dark
When the wheel of pain stops turning
And the branding iron stops burning
When the children can be children
When the desperados weaken
When the tide rolls into greet them
And the natural law of science
Greets the humble and the mighty
And the billion candles burning
Lights the dark side of every human mind ..."

Roger Waters, Each Small Candle

"Life is a waterfall

we're one in the river

and one again after the fall

swimming through the void

we hear the word

we lose ourselves

but we find it all

cause we are the ones that want to play

always want to go

but you never want to stay

and we are the ones that want to choose

always want to play

but you never want to lose ..."

System of a Down, Aerials

Notation and abbreviations

^{1}H	Hydrogen
^{23}Na	Sodium
3DPR	3-Dimensional Projection Reconstruction
^{31}P	Phosphorus
ADP	Adenosine d-phosphage
ATP	Adenosine triphosphage
BMI	Body Mass Index
BOLD	Blood-Oxygen Level Dependent
CS	Compressed Sensing
DA 3DPR	Density-Adapted 3-Dimensional Projection Reconstruction
DCF	Density Compensation Function
DQF	Double Quantum Filtered
EFG	Electric Field Gradient
EMS	Electrical Muscle Stimulation
FID	Free Induction Decay
FOV	Field Of View
FWHM	Full-Width-at-Half Maximum
GAG	Glycosaminoglycan

IFFT	Inverse Fast-Fourier Transform
ISTO	Irreducible Spherical Tensor Operator
MQF	Multiple Quantum Filtered
MR	Magnetic Resonance
MRI	Magnetic Resonance Imaging
MRS	Magnetic Resonance Spectroscopy
MVC	Maximum Voluntary Contraction
NADPH	Nicotinamide adenine dinucleotide phosphate
NMR	Nuclear Magnetic Resonance
NUFFT	Non-Uniform Fast-Fourier Transform
OA	Osteoarthritis
PCr	Phosphocreatine
PR	Projection Reconstruction
PSF	Point Spred Function
QF	Quantum Filtered
RF	Radiofrquency
SAR	Specific Absorption Rate
SD	Standard Deviation
SNR	Signal-to-Noise Ratio
SQF	Single Quantum Filtered
T_2	Transverse relaxation time
T_2^*	Transverse relaxation time in the presence of magnetic field inhomogeneity
T_{2f}	Fast transverse relaxation time component
T_{2s}	Slow transverse relaxation time component

T_{aq}	Acquisition window duration
TPI	Twisted Projection Imaging
TQF	Triple Quantum Filtered
TR	Repetition Time
TSC	Total Sodium Concentration

Contents

List of Figures

Chapter 1

Introduction

Sodium (^{23}Na) magnetic resonance spectroscopy/imaging (MRS/MRI) is a powerful technique that provides a way to non-invasively assess tissue sodium content, *in vivo*. Sodium MRS offers a relatively high temporal resolution, on the order of seconds, compared to sodium MRI which is the on order of minutes to tens of minutes. This makes MRS an ideal candidate for monitoring dynamic physiological changes in tissues, such as contracting skeletal muscle. Sodium MRI allows visualization of bulk tissue sodium content. Although highly useful, ^{23}Na MR approaches are not routinely used in clinical settings. The major obstacles facing sodium MRI are low signal-to-noise ratio (SNR) and low image resolution, both of which contribute disadvantageously to long acquisition times. Because ^{23}Na is the most abundant free cation in the body, and because of its tremendous importance in biological systems, there is considerable interest in optimizing and improving ^{23}Na MR techniques.

1.1 Outline

It should be noted that this thesis is formatted as a 'Sandwich Thesis', indicating a McMaster University style that is made up of some introductory chapters followed by published, or submitted manuscripts, and concluding with a summary and conclusions chapter. There were three overall goals for this PhD dissertation, all focused on the improvement and application of ^{23}Na MR methodologies:

1. To modify a commercially available electrical muscle stimulation (EMS) unit to permit muscle activation during MRI scanning, and monitor the resulting changes using MR techniques such as ^{23}Na MRS.

2. To develop a rapid ^{23}Na MRS approach to allow near real-time assessment of dynamically contracting human skeletal muscles.

3. To optimize ^{23}Na MRI acquisition of human knee articular cartilage MRI, in order to improve image quality.

In this dissertation, Chapter 2 provides a discussion on the biological aspects and MR properties of ^{23}Na. The ^{23}Na nucleus is quadrupolar and this discussion details the MRS/I techniques that exploit this property in order to assess both intracellular and total *in vivo* sodium content. More specifically the chapter describes how human musculoskeletal tissues can be evaluated using ^{23}Na MR techniques.

Chapter 3 outlines the hypotheses and objectives that this dissertation focuses on.

The study of muscle dynamics is easily, and typically accomplished through voluntary exercise. However, repeated voluntary motion, through an exercise task, is not perfectly consistent; there is always variability in range of motion, acceleration/deceleration and force generated. To drive muscle in a consistent fashion, reliance on voluntary contraction is avoided. As an alternative, Chapter 4 describes

the modification and utilization of a standard clinical electrical muscle stimulation (EMS) system. The system was modified to allow muscle stimulation while a subject is being scanned inside an MRI scanner. Modifications are essential to avoid RF interference from the outside world into MR images, and also to ensure the EMS system is safe and will avoid harming anyone. This type of system can be used to consistently assess muscle function and would be of perfect utility in the evaluation of individuals with muscle impairment. In Chapter 4 an MR-compatible electrical muscle stimulation (EMS) unit is tested with concurrent ^{31}P spectroscopy and blood oxygen level dependent (BOLD) acquisitions.

Chapter 5 describes a new approach to non-invasively perform dynamic functional tissue measures. It is well understood in the scientific community that if one wants to assess dynamic non-invasive metabolic changes in tissues then an assessment of high energy phosphates using ^{31}P-MRS is the method most often considered. The study of muscle energetics using phosphorous ^{31}P MRS has been thoroughly described and used over the many years since its first usage. This method is valuable in providing information on intracellular pH (pH_i) and magnesium (Mg^+), and high energy phosphates phosphocreatine (PCr), adenosine triphosphate (ATP), phosphate mono- and di-esters, and to a lesser extent adenosine diphosphate (ADP) and nicotinamide adenine dinucleotide phosphate (NADPH). Even though it provides a wealth of information ^{31}P MRS suffers from difficulties in spatial localization and extremely poor resolution during imaging. The utility of ^{31}P is often discussed because of its high natural abundance (100%), relatively high concentration and high gyromagnetic ratio (17.235MHz/T). On the other hand ^{23}Na is also a nucleus worth consideration. Sodium-23 also is 100% percent naturally abundant and has a high concentration,

being the most abundant free cation in the body. Furthermore, maintenance of the high intra to extracellular sodium gradient is ATP dependent (it has been estimated that 50% of energy used by cells is for maintenance of this gradient). With these key features for ^{23}Na it is a highly worthy candidate for providing physiological information about muscle contraction. The knowledge of sodium changes in intra- and extracellular compartments could be useful in better understanding the Na^+/K^+-ATPase function (or malfunction), which is the active cellular membrane protein complex that maintains the sodium gradient keeping intracellular ^{23}Na low and extracellular approximately 10x higher. For the first time, in chapter 5, details about a novel methodology that enables monitoring of dynamic changes in the total and intracellular sodium in contracting muscle are presented.

Chapter 6 explores the feasibility of applying the methodology described in chapter 5 in conjunction with EMS to provide a means of muscle condition assessment for subjects with impaired muscle motor function.

Chapter 7 discusses how sodium MR image quality can be improved as a consequence of lengthening the acquisition window. Sodium magnetic resonance imaging (MRI) is signal-to-noise (SNR) limited. The SNR improves by the square root of the acquisition window (T_{aq}) length. However, when T_{aq} is increased it leads to image blurring. Thus the purpose of this component of the dissertation was to investigate effects of varying T_{aq} length on density adapted 3-dimensional projection reconstruction (DA-3DPR) articular cartilage ^{23}Na image quality. The results indicate that the SNR benefit from increasing T_{aq} duration outweighs the adverse effects of blurring in the images.

One way to reduce ^{23}Na MRI scan time is to reduce the number of k-space trajectories required to cover whole k-space. However, reducing the projections may lead to under-sampling and increased aliasing artifacts. Chapter 8 discusses a novel pseudo-random non-Cartesian k-space acquisition that significantly minimizes the aliasing artifacts as compared to under-sampled Cartesian acquisition scheme.

Chapter 9 summarizes the work discussed in this dissertation and suggests future direction on what has been accomplished here.

Chapter 2

Sodium Biological and Magnetic Resonance Aspects

2.1 Sodium in Biological Tissues

As the most prevalent cation in the body, sodium is involved in many active cellular processes, including muscle contraction, nerve impulse conduction, cellular homeostasis, etc. There are predominantly two pools of sodium in a biological tissue: intra- and extracellular pools. The normal tissue extracellular sodium concentration ($[Na]_e$) is about 145 mM, mostly in the form of free Na^+ in the aqueous extracellular milieu, whereas, intracellular concentration ($[Na]_i$), mainly bound to glycosides and proteins, is approximately 12 to 20 mM (Maudsley and Hilal (1984)). This concentration gradient across the cell membrane is maintained by energy consuming Na^+/K^+-ATPase (Fig.2.1). For example, in neurons, it has been estimated that maintenance of this gradient takes up to 50% of the intracellular energy (Rolfe and Brown (1997)). It is essential for carrying out several vital cellular processes such as regulating osmosis,

electrical conduction and balancing pH. Maintenance of the intra- and extracellular concentrations of sodium is indicative of cellular and metabolic integrity (Seshan and Bansal (1996) ,Madelin *et al.* (2014)). Study of the alterations in transmembrane sodium concentrations helps investigate normal and disease conditions such as skeletal myopathies, exercising muscle, cellular proliferations during oncogenesis, and ischemic heart disease (Constantinides *et al.* (2000)).

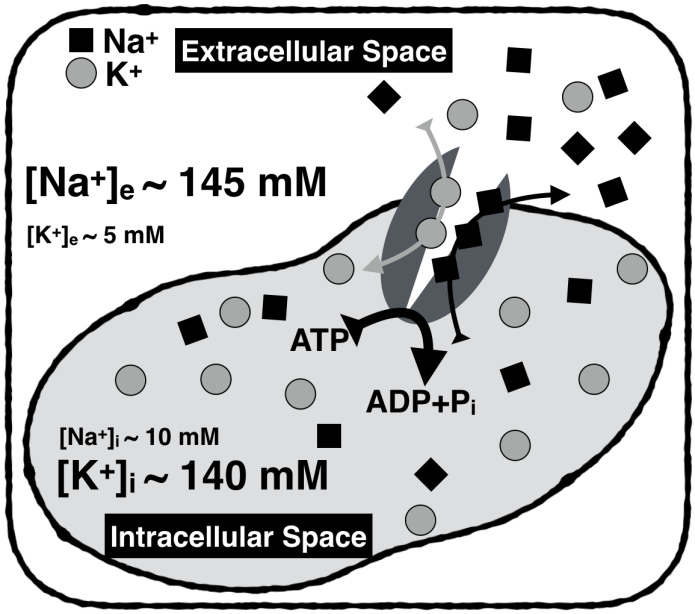

Figure 2.1: Schematic of sodium concentration gradient across membrane and how Na^+/K^+-ATPase constantly pumps sodium out of the cell.

2.2 Sodium Magnetic Resonance Properties

Sodium, ^{23}Na (spin, S = 3/2), is one of many biologically relevant quadrupolar nuclei such as ^{7}Li, ^{35}Cl, ^{37}Cl, ^{39}K (S = 3/2), ^{17}O, ^{25}Mg, ^{27}Al, ^{69}Zn (S = 5/2), and ^{43}Ca (S = 7/2) (Jaccard *et al.* (1986)). Even though the gyromagnetic ratio (γ) for ^{23}Na is roughly 1/4 of that of proton (11.262 MHz/T vs. 42.576 MHz/T) it is still the

second most visible NMR nucleus considering its relative natural abundance (100%) and *in vivo* concentration. ^{23}Na relative NMR sensitivity is about 9.25% that of ^{1}H considering the same concentration of element (Nagel *et al.* (2013)). Since the natural abundance of both nuclei are almost the same (100% for ^{23}Na, and 99.99% for ^{1}H) the most important factor for relatively low NMR sensitivity of ^{23}Na is due to low gyromagnetic ratio. This is because (Levitt (2001)):

1. The nuclear magnetic moment is proportional to the nuclear gyromagnetic ratio. Hence, the larger the γ of a nucleus, the larger its macroscopic magnetic moment, and consequently the larger its NMR signal.

2. The nuclear Larmor frequency is proportional to the gyromagnetic ratio. The bigger the gyromagnetic ratio of a nucleus, the bigger its Larmor frequency, and this leads to a bigger current induced in the coil (hence greater NMR signal detected).

3. Lastly, the Zeeman energy level splitting is proportional to the gyromagnetic ratio. The bigger the gyromagnetic ratio of the nucleus the bigger the Zeeman energy level splitting and hence the greater the NMR signal.

Electromagnetic Interactions

The ^{23}Na nucleus interacts with a surrounding external magnetic field, through its magnetic moment, and with an electric field, through its positive electric charge. Sodium with nuclear spin S = 3/2 produces four distinct energy levels when exposed to an external magnetic field. This is referred to as Zeeman splitting or interaction. The energy levels for a spin 3/2 nucleus are shown in figure 2.2a. As depicted in the

figure, there are three possible single quantum transitions i.e. $\Delta m = \pm 1$; $3/2 \leftrightarrow 1/2$, $1/2 \leftrightarrow -1/2$, and $-1/2 \leftrightarrow -3/2$. The transition $1/2 \leftrightarrow -1/2$ is called central transition and the other two are called outer or satellite transitions. The central transition contains 40% of the signal and the two satellite transitions each contain 30% of the signal.

The electric charge distribution within the ^{23}Na nucleus is spherically asymmetric leading to its electric quadrupolar moment that interacts with the surrounding electric field gradient (EFG). This type of interaction is referred to as quadrupolar interaction and affects the satellite transitions more strongly than inner transition. The extent of the quadrupolar interaction depends on the orientation, magnitude and temporal duration of EFG arising from the quadrupole moment of the nucleus and surrounding environment. Thus, it is important to consider the environment to which the nucleus is exposed. Generally, the quadrupolar interactions average to zero in liquids while they are non-zero in solids. In liquids, the ^{23}Na system is considered an "isotropic" system, where quadrupolar nuclei "tumble" very fast, i.e. the rotational correlation time is much shorter than the Larmor period; the central and outer transitions show the same relaxation times. This will result in a relatively long monoexponential transverse, T_2, relaxation and the compound would be 100% NMR visible. In biological tissues (an intermediate regime between liquid and solid states) quadrupolar nuclei interact with macromolecules EFG and tumble relatively slowly. In this case, the satellite transitions decay faster than the central transitions leading to biexponential relaxation. Under this condition, the energy states of the sodium pool interacting with the macromolecules, "transiently bound" Na^+, will be altered and double quantum (DQ) transitions (-3/2 $\leftrightarrow$ 1/2 and -1/2 $\leftrightarrow$ 3/2) and

triple quantum (TQ) transitions (-3/2 $\leftrightarrow$ 3/2) become possible (Fig.2.2b). The DQ and TQ transitions are not NMR visible. However, techniques have been developed that allow their detection (discussed below).

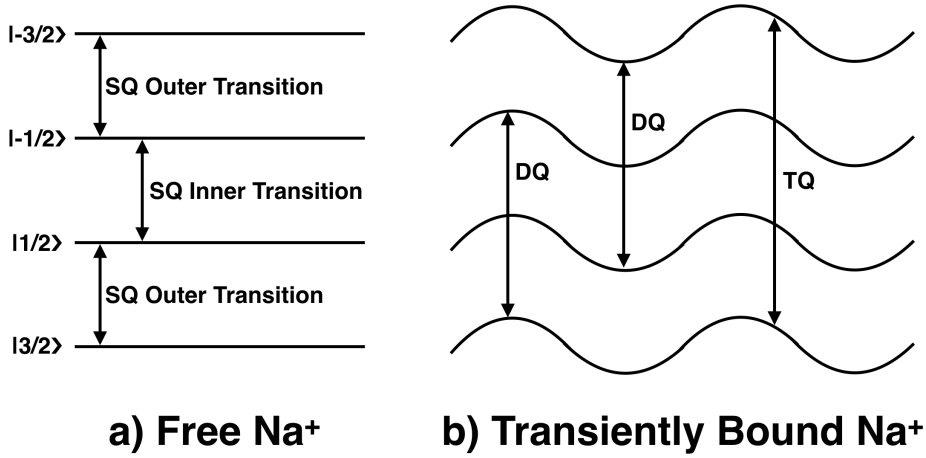

Figure 2.2: Four energy states of a) free and b) transiently bound sodium. Free sodium experiences SQ transitions with quadrupolar interactions averaged to zero. The transiently bound sodium experiences DQ and TQ transitions due to non-zero quadrupolar interactions with macromolecular EFG.

2.3 Sodium Multiple Quantum Magnetic Resonance Spectroscopy

Conventional single radiofrequency (RF) pulse sodium NMR experiments create single quantum transitions ($\Delta m = \pm 1$) that lead to observable transverse magnetization. However, multiple quantum transitions do not lead to observable magnetization. In order to create and convert the MQ transitions ($\Delta m \neq \pm 1$) to observable magnetization, a series of RF pulses is required that is referred to as a "*multiple quantum filter (MQF)*"(Navon *et al.* (2001)). The MQF consists of at least three non-selective

Table 2.1: Irreducible spherical Tensor Operator for ^{23}Na

ISTO	**Definition**
T_{10}	Longitudinal magnetization
$T_{1\pm1}$	Rank 1 SQC
$T_{2\pm1}$	Rank 2 SQC
$T_{3\pm1}$	Rank 3 SQC
$T_{2\pm2}$	Rank 2 DQC
$T_{3\pm2}$	Rank 3 DQC
$T_{3\pm3}$	Rank 3 TQC

SQC, DQC, TQC are single, double, triple quantum coherences, respectively.

pulses as depicted in figure 2.3.

Before explaining how MQF detects MQ transitions, the notation by which the state of a system of spins is represented should be introduced. A density matrix is a mathematical means to describe the dynamics of a system of spins and is elegantly called irreducible spherical tensor operator (ISTO) basis (Madelin *et al.* (2014)). It is denoted by T_{nm},where n is the rank of the matrix and m is the coherence of the tensor with $|m| < n$. The coherence m is changed by applying a non-selective RF pulse while the relaxation and quadrupolar interaction can change the rank n. The definition of each tensor used in here is given in table 2.1.

The first RF pulse brings the longitudinal magnetization T_{10} into the transverse plane creating transverse magnetization $T_{1\pm1}$. The transverse magnetization $T_{1\pm1}$ evolves to single quantum coherences (SQC) with different ranks $T_{1\pm1}, T_{2\pm1}, T_{3\pm1}$ as a result of relaxation and quadrupolar interactions during preparation time τ. The second RF pulse converts the SQC into multiple quantum coherences (MQC) of ranks $T_{2\pm2}, T_{3\pm2}, T_{3\pm3}$. The third RF pulse brings the MQCs into SQCs of ranks $T_{1\pm1}, T_{2\pm1}, T_{3\pm1}$, which then evolve to detectable SQC with rank $T_{1\pm1}$. The evolution

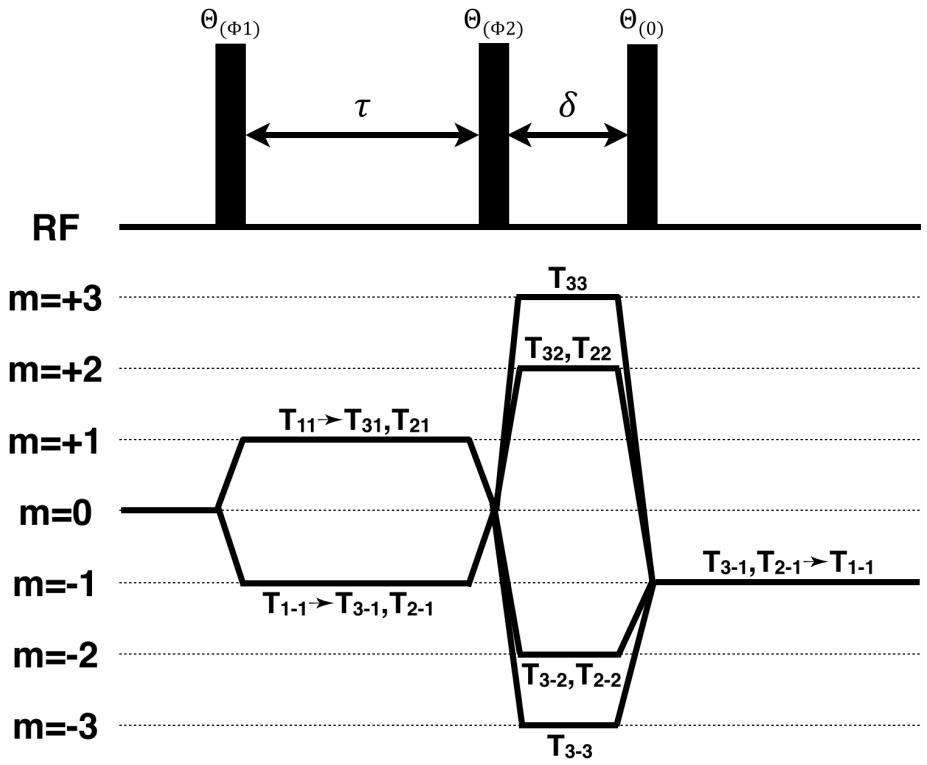

Figure 2.3: Multiple quantum filtered (MQF) pulse sequence and the possible coherence transfer pathways. With proper phase cycling DQCs or TQCs could be detected. A DQF scheme with four-component phase cycling would follow the following parameters: $\theta = 90°, \phi_1 = 0°, 90°, 180°, 270°, \phi_2 = \phi_1, \phi_3 = 0$. A TQF scheme with six-component phase cycling would follow the following parameters: $\theta = 90°, \phi_1 = 30°, 90°, 150°, 210°, 270°, 300°, \phi_2 = \phi_1 + 90°, \phi_3 = 0$.

time, δ, between the second and third RF pulse is kept as short as possible to minimize MQC signal decay. In order to detect either double or triple quantum coherences, DQC or TQC, a proper phase cycling scheme is required which is noted in figure 2.3. The difference between DQF and TQF is that the former detects the contribution of $T_{2\pm1}, T_{3\pm1}$ that is due to biexponential decay and/or quadrupolar splitting, while the latter detects only the contribution of $T_{3\pm1}$ that is only due to biexponential decay,

i.e. slow motion regime. The signal generated by this scheme is of the form

$$M_{xy} = M_0 K_{MQ}(e^{-\tau/T_{2s}} - e^{-\tau/T_{2f}})e^{-\delta/T_{MQ}} cos(p\omega\sigma)(e^{-t_{acq}/T_{2s}} - e^{-t_{acq}/T_{2f}})e^{j\omega t} \quad (2.1)$$

where M_0 is the longitudinal magnetization, K_{MQ} is MQF-specific constant that is 3/20 for DQF and 9/40 for TQF, T_{2s} and T_{2f} are the slow and fast transverse relaxation times, respectively, T_{QM} is MQ transverse relaxation time, p is the QF order, 2 for DQF and 3 for TQF, ω is the resonance offset, and T_{acq} is the acquisition window duration (Seshan and Bansal (1996)). It is interesting to note that the MQF FID is the difference between the fast and slow components of the transverse magnetization with equal weighting. In contrast, the SQF signal is the weighted sum of the two transverse magnetization components (Clayton and Lenkinski (2003)). Examples of SQF and TQF signals, referred to as free induction decays (FIDs), along with their transverse magnetization components and spectra are depicted in figure 2.4.

In the work presented in this dissertation the use of TQF was chosen over DQF due to the following reasons:

1. According to equations 2.1, the TQF signal is 1.5 times greater than that of DQF.

2. The loss in TQF signal is smaller than DQF during the evolution time, δ. This is because the TQF transverse relaxation, T_2, is dominated by the slow SQ T_2, whereas DQF T_2 is affected by both slow and fast components of QF T_2.

3. The TQF signal is less sensitive to flip angle than DQF (Reddy *et al.* (1994)). This becomes important in the applications, such as the one presented in chapter 5, that utilize a surface coil.

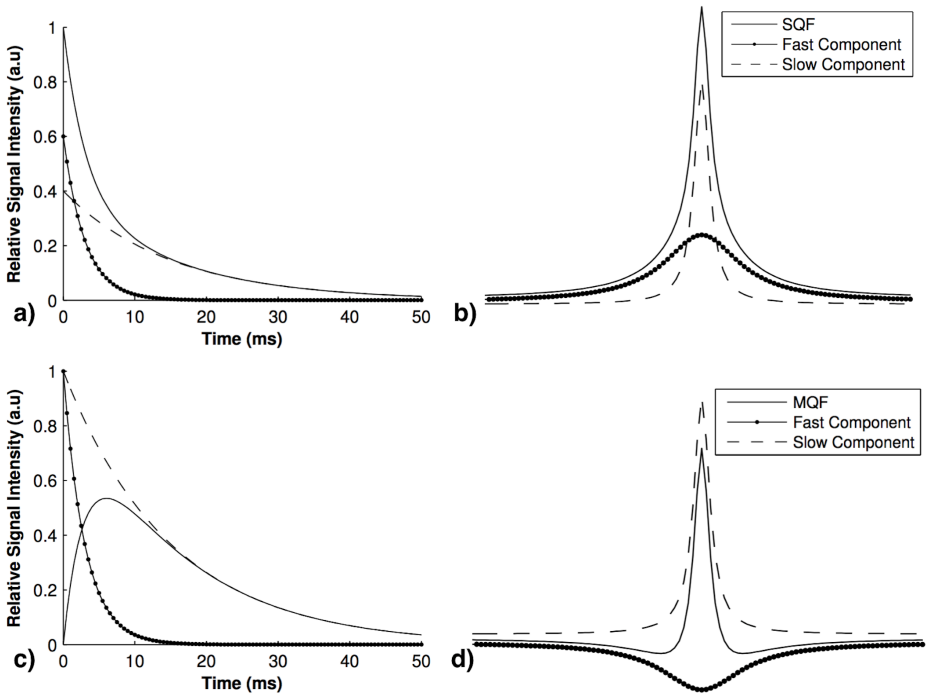

Figure 2.4: Examples of a) SQ and c) MQ filtered FIDs with nominal $T_{2f} = 3ms$ and $T_{2s} = 15ms$ and their corresponding absorption spectra b and d, respectively. The SQF FID is the result of a weighted sum of the fast and slow components while the MQF FID is the result of subtraction of the two components equally weighted. The slow component absorption curve is already inverted, indicative of subtraction, in d.

4. Since the TQF signal is only due to biexponential relaxation, i.e. TQC $T_{3\pm1}$, the interpretation of TQF is simpler than the DQF signal, which contains both the contribution of biexponential relaxation and quadrupolar splitting. This is significant in the application of QF in the study of the effects of exercise contracting muscle sodium content (Chapter 3).

2.4 Sodium Magnetic Resonance Imaging

In the previous section, the NMR properties of sodium was discussed. SQF, DQF, and TQF pulse sequences generate a time signal, i.e FID. The FID represents the

signal detected by the RF coil and does not contain any specific spatial information; i.e. one object, one signal, one spectrum. In order to create an image, where the signal localization is manifested as image pixel intensity, the FID needs to be spatially encoded. This idea was introduced in 1973 by Paul Lauterbur that led to the magnetic resonance imaging phenomenon (Lauterbur (1973)).

In this section, the concept of MR signal spatial encoding is briefly described and then advanced sodium MR image acquisition methods are introduced.

2.4.1 Spatial Encoding

Suppose an RF pulse has created a transverse magnetization in a heterogeneous sample, denoted by $M_{xyz}(x, y, z, 0^+)$, in a uniform magnetic field. Variables x, y, and z represent the location of the magnetization within the sample and 0^+ denotes the time immediately after the RF excitation. The signal detected by the RF coil, i.e. FID, is then an integral over the entire field of view (FOV) of the coil and is given by

$$S(t) = A \int_{-\infty}^{+\infty} \int_{-\infty}^{+\infty} \int_{-\infty}^{+\infty} M_{xyz}(x, y, z, 0^+) e^{-j(\gamma B_0 t - \phi_0)} e^{t/T_2(x,y,z)} dx dy dz, \qquad (2.2a)$$

where the constant, A, represents gain due to physics and instrumentation, γ is the gyromagnetic ratio (specific to the nucleus), B_0 is main magnetic field strength, and ϕ_0 the initial signal phase (assumed zero). The quantity γB_0 is referred to as the Larmor frequency, ω, that is the frequency at which the spin magnetic moment is precessing around the main magnetic field. The Larmor frequency is the same across

the object under uniform B_0. After a slight rearrangement $S(t)$ is written as:

$$S(t) = e^{-j\gamma B_0 t} \int_{-\infty}^{+\infty} \int_{-\infty}^{+\infty} \int_{-\infty}^{+\infty} AM_{xyz}(x, y, z, 0^+) e^{t/T_2(x,y,z)} dxdydz \tag{2.2b}$$

The term under the integral is an MR quantity referred to as the *effective spin density* and is defined as

$$f(x, y, z) = AM_{xyz}(x, y, z, 0^+) e^{t/T_2(x,y,z)} \tag{2.3}$$

With the above definition, the received signal is given by

$$S(t) = e^{-j\gamma B_0 t} \int_{-\infty}^{+\infty} \int_{-\infty}^{+\infty} \int_{-\infty}^{+\infty} f(x, y, z) dxdydz \tag{2.4}$$

The MR signal is always demodulated in the receiver chain resulting in a baseband signal

$$s_0(t) = e^{+j\gamma B_0 t} s(t) \tag{2.5a}$$

$$= \int_{-\infty}^{+\infty} \int_{-\infty}^{+\infty} \int_{-\infty}^{+\infty} f(x, y, z) dxdydz, \tag{2.5b}$$

that is the integral of all effective spin densities within the sample and contains no spatial information.

Now, suppose a gradient field, G_x, along x-direction is applied across the object. As a result, the Larmor frequency across the object in the x-direction is no longer uniform and is spatially dependant:

$$\omega(x) = \gamma(B_0 + G_x x). \tag{2.6}$$

This will change the FID signal representation in equation 2.2a as the following:

$$S(t) = A \int_{-\infty}^{+\infty} \int_{-\infty}^{+\infty} \int_{-\infty}^{+\infty} M_{xyz}(x, y, z, 0^+) e^{-j(\gamma(B_0 + G_x x)t)} e^{t/T_2(x,y,z)} dxdydz, \quad (2.7a)$$

$$= e^{-j\gamma B_0 t} \int_{-\infty}^{+\infty} \int_{-\infty}^{+\infty} \int_{-\infty}^{+\infty} A M_{xyz}(x, y, z, 0^+) e^{-j\gamma G_x x t} e^{t/T_2(x,y,z)} dxdydz. \quad (2.7b)$$

Considering the effective spin density definition (eq. 2.3), the baseband signal is given by:

$$s_0(t) = \int_{-\infty}^{+\infty} \int_{-\infty}^{+\infty} \int_{-\infty}^{+\infty} f(x, y, z) e^{-j\gamma G_x x t} dxdydz. \quad (2.8)$$

The term $\gamma G_x t$ in the above equation represents the spatial frequency and can be presented by variable k_x as following

$$k_x = \gamma G_x t \quad (2.9)$$

and consequently, the baseband signal can be written as

$$s_0(t) = \int_{-\infty}^{+\infty} \int_{-\infty}^{+\infty} \int_{-\infty}^{+\infty} f(x, y, z) e^{-jk_x x} dxdydz. \quad (2.10)$$

Introducing gradients along y- and z-directions, will change the Larmor frequency to

$$\omega(x) = \gamma(B_0 + G_x x + G_y y + G_z z) \quad (2.11)$$

leading to k_y and k_z spatial frequencies

$$k_y = \gamma G_y t \quad (2.12a)$$

$$k_z = \gamma G_z t \tag{2.12b}$$

and, in a similar fashion, the baseband signal could be presented as

$$s_0(t) = \int_{-\infty}^{+\infty} \int_{-\infty}^{+\infty} \int_{-\infty}^{+\infty} f(x, y, z) e^{-j(k_x x + k_y y + k_z z)} dx dy dz. \tag{2.13}$$

Representing the FID in the form of equation 2.13 is important. The triple integral on the right hand side can be interpreted as a 3-dimensional Fourier transform. Taking the inverse Fourier transform of equation 2.13 will give $f(x, y, z)$. This reveals an important concept in MR imaging, that is the FID can be spatially encoded using gradients and the signal location would be recovered by taking the inverse Fourier transform of the encoded FID leading to an MR image. The encoded signal is in Fourier space and, by convention, this space is called *k-space*. The letter k is chosen for naming this space because the signal is a function of spatial frequencies that are denoted by letter k in physics.

2.4.2 Advanced Sodium MRI Pulse Sequences

There are three standard gradient coils that are available on any conventional MRI system; x-, y-, and z-gradients. The spatial encoding is achieved through the gradient waveforms generated by these coils. The design of the gradient waveforms depends on how the k-space is filled and is restricted by the maximum gradient amplitude available on a given MRI system, and by the maximum allowable slew rate that can cause peripheral nerve stimulation. The timing and the shape of the RF pulses and gradient waveforms are described by what is called a MRI *pulse sequence*.

Conventional MRI pulse sequences follow rectilinear, i.e. Cartesian, sampling of

the k-space as depicted in figure 2.5a. This method is conventionally preferred because it is easy to implement and the k-space data can be easily reconstructed into images by performing Inverse Fast Fourier transform (IFFT). However, this method requires the spatial encoding to be performed in two sequential steps: 1) phase encoding, and 2) frequency encoding. Phase encoding occurs prior to data acquisition while the frequency encode step is performed concurrent to acquisition. Although this method in widely used in proton imaging it is not a suitable method for MRI of low-SNR, and short-T_2 species such as sodium. This is because the phase encoding step duration is comparable to sodium short T_2s that leads to signal loss prior to data acquisition. With the advancement of MRI hardware and availability of MRI at higher field (≥ 3 T), non-Cartesian *k-space* sampling methods emerged, such as radial sampling (figure 2.5b). These methods eliminate the phase encode step and allows for data acquisition right at the end of the RF pulse, hence, facilitating the acquisition of the short-lived T_2 species and improving SNR.

There are two main families of non-Cartesian sampling methods used in sodium MRI: 3-dimensional projection reconstruction (3DPR) and twisted projection imaging (TPI) (Boada *et al.* (1997)). Projection reconstruction was the first non-Cartesian method. It consists of radial trajectory lines starting from the centre of the k-space. This method is very easy to implement. However, it is not an efficient method to cover k-space and, hence, it requires many trajectories. It also suffers from what is called SNR-efficiency, denoted by η. This is because PR non-uniformly samples k-space. This PR intrinsic property arises from its design. The sampling density is much higher at the centre compared to the periphery of k-space and needs to be corrected for by what is referred to as a density compensation function (DCF).

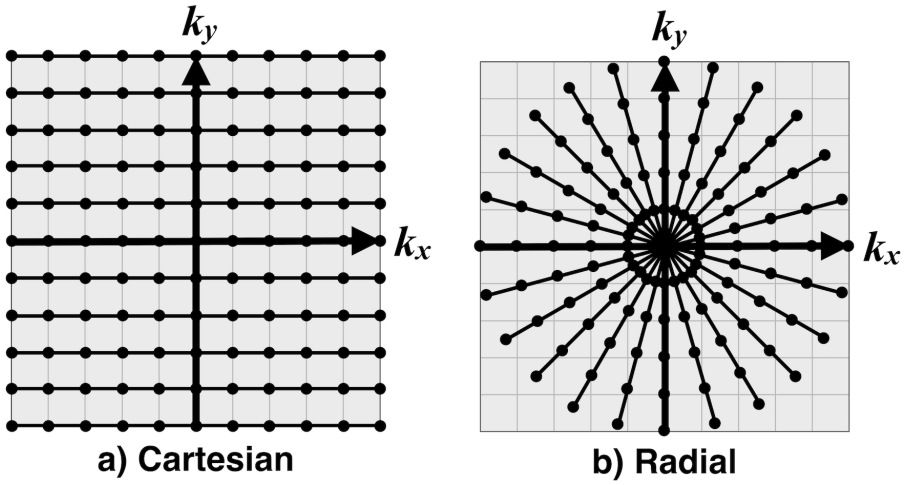

Figure 2.5: A general 2-dimensional a) Cartesian, and b) radial k-space sampling scheme. The horizontal and radial solid dots along the lines represent the sampled trajectories in Cartesian and radial schemes, respectively. In a conventional scheme, the phase encoding is performed prior to data acquisition, within each repetition time (TR), Whereas, in non-Cartesian sampling, the phase encoding step is eliminated within each TR; instead, phase encoding happens between each TR.

TPI was implemented in response to addressing the shortcomings of PR, i.e. huge number of trajectories and non-uniform k-space sampling. TPI consists of a twisted trajectory that spirals out of the centre of k-space on a surface of a cone. The twist property allows for sampling a larger portion of the k-space per trajectory and, therefore, requiring less number of trajectories to cover the entire k-space. This design also provides a much more uniform sampling of the k-space leading to a high SNR efficiency that is very close to that of Cartesian sampling. However, this design is much more complicated to implement. It is also more demanding on the gradient hardware in terms of slew rate and gradient amplitude.

A more recent variation of 3DPR is called density-adapted 3DPR (DA-3DPR) (Nagel *et al.* (2009)). This design improves the 3DPR SNR efficiency that matches that of TPI while not being as hardware demanding as TPI. At the same time, its

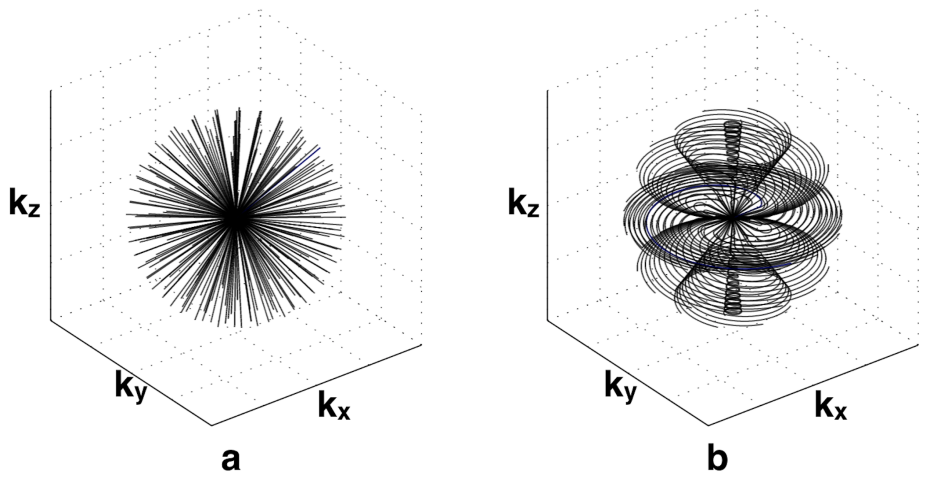

Figure 2.6: Two main families of non-uniform k-space sampling used for sodium MRI: a) 3-dimensional projection reconstruction (3DPR) and b) Twisted projection imaging (TPI)

implementation is as easy as that of 3DPR. In addition, the implementation gives full control to the pulse sequence designer in terms of readout acquisition duration; an important property that is not available in the current implementation of TPI. DA-3DPR has been selected as the k-space sampling scheme of choice for the work presented in chapter 7 because it allows the optimization of the pulse sequence by varying the acquisition window duration while keeping the rest of the pulse sequence parameters the same.

Since SNR efficiency is an important factor in sodium pulse sequence design it needs to be introduced here. Non-uniform k-space acquisition leads to SNR loss by a factor denoted as η. In MR literature, η is referred to as either 'SNR efficiency' (Gurney *et al.* (2006), Tsai and Nishimura (2000)) or 'efficiency factor' (Nagel *et al.* (2009)). SNR efficiency is the term used to refer to η throughout this dissertation.

Non-uniform sampling of k-space inherently leads to increased noise variance in

the image according to (Liao *et al.* (1997))

$$\sigma_i^2 = \int_{V_k} \frac{\sigma^2}{D(k)} dV_k$$

where σ_i is the image noise standard deviation (SD), σ^2 is the noise variance in each k-space data point, and *D(k)* is the local sampling density. The SNR loss due to a non-uniform sampling scheme can be quantified by defining SNR efficiency as

$$\eta = \frac{\sigma_{i,uniform}}{\sigma_{i,non-uniform}} \leq 1$$

where $\sigma_{i,uniform}$, and $\sigma_{i,non-uniform}$ are the image noise SD in the uniform and non-uniform k-space sampling schemes, respectively. SNR efficiency, η, is equal to 1 when the sampling scheme is uniform. In order to demonstrate how image noise SD is affected by the type of k-space sampling scheme, numerical evaluation of these schemes were performed by reconstructing Gaussian noise in k-space. The effect of non-uniform sampling on image SD using different acquisitions methods are compared to uniform sampling in figure 2.7. The measured noise SD in the images reconstructed from the 3DPR scheme was highest while TPI and DA-3DPR produced the same level of noise as Cartesian sampling scheme due to uniform sampling.

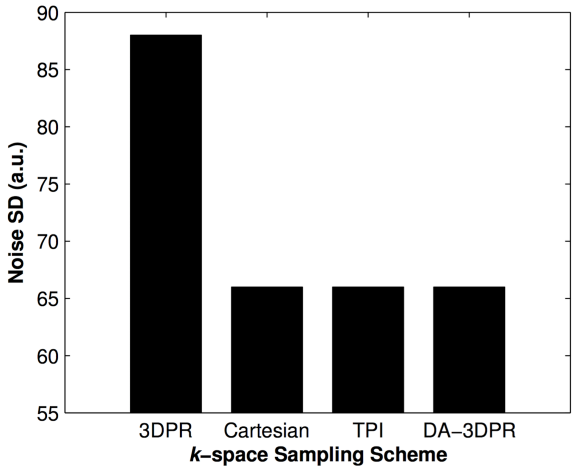

Figure 2.7: Measured noise SD in the images reconstructed from simulated Gaussian noise in *k-space* using different sampling schemes. TPI and DA-3DPR noise performance is the same as Cartesian scheme due to uniform sampling.

Chapter 3

Hypotheses and Objectives

The physiological role and importance of sodium in health, along the sodium magnetic resonance (MR) properties and techniques were discussed in the previous chapter. The overall hypotheses addressed in this dissertation are:

a) Electrical muscle stimulation (EMS) provides a reliable alternative means of producing controlled and repeatable human skeletal muscle contraction and can be safely used concurrently in the bore of a magnetic resonance imaging (MRI) scanner.

b) Quantum filtered sodium MR signals could be sensitive to acute dynamic changes induced by skeletal muscle exercise. The single quantum filtered signal, indicative of total sodium concentration, and triple quantum filtered signal, indicative of bound intracellular concentration, would be differentially affected by exercise due to environment-dependent sodium MR properties.

c) Increasing the acquisition window duration would enhance sodium MRI signal-to-noise ratio (SNR) at the cost of blurring. The goal here was to investigate whether the SNR benefits outweigh adverse effects of blurring.

d) Pseudo-random non-Cartesian k-space sampling would lead to minimized (i.e.

benign) aliasing artifacts compared to conventional Cartesian under-sampling schemes. Under-sampled pseudo-random non-Cartesian acquisition may produce sodium MR images with comparable image quality despite low-SNR limitation in sodium MRI.

The objectives of this dissertation were:

1. To modify a commercially available electrical muscle stimulation (EMS) unit to induce muscle contraction during MRI scanning, and monitor the resulting changes using MR techniques such as ^{23}Na MR spectroscopy (MRS).

2. To develop a rapid ^{23}Na MRS approach to allow near real-time assessment of dynamically contracting human skeletal muscles.

3. To optimize ^{23}Na MRI acquisition of human knee articular cartilage MRI, in order to improve image quality.

Chapter 4

A Safe MRI-Compatible Electrical Muscle Stimulation (EMS) System

Alireza Akbari M.Eng., Conrad P. Rockel B.Sc., Dinesh A. Kumbhare MD, M.Sc., FRCPC, and Michael D. Noseworthy Ph.D., P.Eng.

4.1 Context of the Paper

This paper discusses an alternative means of inducing muscle contraction, alternative to voluntary exercise, while being imaged inside the bore of a magnetic resonance imaging (MRI) scanner. The motivation behind this work was initially driven by a need to eliminate/minimize human variation in contraction behaviour. Essentially it was hypothesized the EMS unit would result in highly reproducible (temporally and amplitude) contractions. It was also thought that if it could work this solution would be ideal for assessment of muscle contractility in subjects with impaired muscle motor function. Since a commercially available EMS unit is not MRI compatible, this study

provides a simple MRI-compatible solution to this problem. Then, validation of the efficacy was performed using 31P MR spectroscopy and muscle blood oxygen level dependent (BOLD) imaging, comparing these methods to the same obtained during voluntary calf muscle exercise.

4.2 Declaration Statement

Alireza Akbari developed, built, and validated the MRI-compatible section of the EMS unit, built the ^{31}P radiofrequency (RF) coil and with the help of Conrad Rockel upgraded the custom-built MRI-compatible wooden ergometer to fit in the new MRI upgrade. Alireza Akbari also, as principle author, wrote the first draft of the article, collected the data and performed analysis and created figures and tables as appropriate. Michael D. Noseworthy, as corresponding author, provided the concept for the paper, funding and advice, and performed statistical analysis and substantial editing and submission of the manuscript for publication. Conrad Rockel helped with methodology development, data collection, BOLD analysis, and proofreading. Dr. Kumbhare helped with clinical relevance/methodology development, proofreading/editing, guidance and commentary and also provided the EMS unit itself.

This paper has been accepted for publication in The Journal of Magnetic Resonance Imaging (JMRI).

4.3 Paper

A Safe MRI-Compatible Electrical Muscle Stimulation (EMS) System

Alireza Akbari MEng[1,2], Conrad P. Rockel BSc[1,2], Dinesh A. Kumbhare MD, MSc, FRCPC[1,3] and Michael D. Noseworthy PhD PEng[1,2,4]

[1]*School of Biomedical Engineering, McMaster University, Hamilton, Ontario, Canada;*
[2]*Imaging Research Centre, St. Joseph's Healthcare, Hamilton, Ontario, Canada;*
[3]*Toronto Rehabilitation Institute, Faculty of Medicine, University of Toronto, Toronto, Ontario, Canada;*
[4]*Electrical and Computer Engineering, McMaster University, Hamilton, Ontario, Canada;*

Address for correspondence:

Dr. Michael D. Noseworthy, PhD PEng

Electrical and Computer Engineering

Engineering Technology Building, Room 406

McMaster University

1280 Main Street West., Hamilton, Ontario, Canada. L8S 4K1

VOICE: (905) 525-9140 x23727

EMAIL: nosewor@mcmaster.ca

Running Title: Concurrent MRI and Electrical Stimulation

4.3.1 Abstract

Purpose: To develop an inexpensive MRI-compatible electrical muscle stimulation (EMS) unit and test it for safety and efficacy.

Materials and Methods: A simple MRI-compatible EMS device was developed using radiofrequency (RF) translucent electrodes. RF heating concerns were assessed using optical temperature measurements at electrode sites, during scanning of a phantom. EMS efficacy and consistency was investigated through *in vivo* (n=5) measures of ^{31}P-MRS phosphocreatine (PCr) reduction, and altered blood oxygen level dependent (BOLD) signal and the results were compared to effects from equivalent voluntary effort on the same subjects.

Results: The presence of an EMS pulse did not affect the T2* signal in a phantom. However the presence of the EMS electrodes reduced SNR by 70% at electrode sites which improved to a 10% loss 4cm distally. Neither BOLD scanning nor ^{31}P spectral acquisition resulted in significant temperature changes in the presence of active or passive EMS electrodes. *In vivo* muscle stimulation resulted in 13.5±1.8% reduction in phosphocreatine (PCr), which was not significantly ($p<0.195$) different from voluntary contraction. Reproducible muscle BOLD signal changes following EMS were noted, with maximal increase of 10.0±2.6% seen in the central soleus. For soleus and gastrocnemius compartments EMS produced significantly higher BOLD signal change compared to voluntary contraction ($p<0.05$).

Conclusions: A safe and inexpensive MRI-compatible EMS unit can be easily built for evaluating muscle function and metabolism within a 3T MRI scanner. Clinical applications include evaluating skeletal muscle function in patients with limited or

absent voluntary skeletal motor function or inadequate exercise capacity to allow conventional methods of analysis.

Key words Skeletal Muscle, MRI, electrical muscle stimulation (EMS), ^{31}P-MRS, blood oxygen level dependent (BOLD)

4.3.2 Introduction

Electrical muscle stimulation (EMS) is a technique used to induce skeletal muscle contraction by means of applying electric current. This method has been widely used in applications such as strength training [1, 2] and enhancement of skeletal muscle rehabilitation [3, 4] where electrodes are placed on the skin surface over either a nerve trunk or muscle motor point [5]. Experiments assessing dynamic aspects of muscle physiology have shown EMS to be a quantitative and reproducible means to contract muscle [6]. Thus, EMS could serve as a reliable tool in the study of muscle dynamics in magnetic resonance imaging (MRI) and spectroscopy (MRS) studies.

Phosphorous (^{31}P) MRS has been widely used to assess muscle metabolism at rest and with exercise. The method allows measurement of high energy phosphates including ATP and phosphocreatine, which are highly correlated with the energy state of the muscle cell during exercise [7, 8]. Even though EMS is a potentially consistent and reproducible means to activating muscle it has only been used infrequently with MR methods, primarily in studying (^{31}P PCr dynamics in basic pulse-acquire surface-coil-localized spectroscopy. For example, 31P MRS has been performed during nerve stimulation of the forearm [9, 10], and during direct quadriceps stimulation

[11]. Other MRI techniques such as T2 mapping and T2-weighted imaging have also been used in localization [12] and efficacy assessment [13] of EMS. However, dynamic studies using MRI approaches such as blood oxygen level dependent (BOLD) signal and diffusion tensor imaging (DTI) [14], which could take advantage of EMS in the dynamic assessment of muscle physiology, are absent.

The development of a complete MRI-compatible EMS system would be highly customized, and invariably expensive. However, a simple solution is to modify an existing non-MRI compatible unit. Such a system would need to be cleared for image artifacts and safety (i.e. RF burns due to the presence of electrodes and wires). Therefore the purpose of this work was to modify a commercially-available EMS unit for MRI compatibility so EMS pulses can be safely delivered from the MRI control room to a subject in the bore of a 3T MRI. The resulting modified unit was tested for safety by direct temperature measurement at the site of electrode placement. Lastly EMS efficacy of the modified system was evaluated by assessing dynamic physiological changes in temporal BOLD signal and PCr acquired using ^{31}P-MRS in calf muscle.

4.3.3 Materials and Methods

Instrumentation

A commercial EMG/EMS unit (XLTEK, NeuroMax 1004, Oakville, Canada), used routinely in clinical practice, was used for generating muscle stimulation pulses. Adhesive gel electrodes (Cleartrace REF2700-003, Danlee Medical Products, Inc., Syracuse, New York USA) attached to 30-cm radiofrequency-translucent clip electrode leads (Biopac, LEAD108C, Montreal Quebec, Canada) were used for all stimulation experiments. Since the adhesive gel electrodes did not provide the adequate

stimulation surface area similar to electrodes used in other muscle stimulation studies [11,15], two copper strips of dimension 4.5x9cm2 and 4.5x7cm2 were used to extend the stimulation surface area. The copper strips were attached on the skin surface using protective barrier wipes (AllKare, ConvaTec Inc., Skillman, New Jersey USA). Two 9-metre long coaxial cables were used to relay stimulation pulses from the EMS unit through an 8cm diameter x 30cm long waveguide to the electrode leads (shown in **Fig.4.1a-c**). All imaging experiments were performed using a GE 3T MR750 MRI scanner (General Electric Healthcare, Milwaukee WI). An 8-channel knee coil (3T HD T/R Knee Array, In vivo Corp., Gainesville FL) was used for both phantom T2* and *in vivo* BOLD experiments while an in-house custom designed and built 3-inch diameter transmit/receive surface coil was used for ^{31}P measurements.

Phantom Experiments

Prior to any human experimentation safety concerns due to RF heating near electrodes, and also the effect of electrode placement on image quality (e.g. SNR and geometric distortion), were assessed. These measurements were performed on a 12cm diameter x 25cm long vendor-provided QA/QC cylindrical phantom containing dimethyl silicone fluid, gadolinium and colorant. To study potential RF heating effects, electrodes were placed on the phantom, in a similar orientation to that when used on muscle. Two optical temperature probes (ReFlex-4 RFX273A, Neoptix, Quebec, Canada) were placed under each of the electrodes. The phantom was imaged using Fast Imaging Employing STeady state Acquisition (FIESTA; Axial FOV 26cm, Slice Thickness 5mm, 15 slices, TE/TR/flip = 1.8/4.1ms/90°, matrix=256x256, 64NEX, receiver bandwidth = 125kHz, Scan Time = 16:48), an RF intensive sequence, while temperature was recorded first in the absence of electrodes,

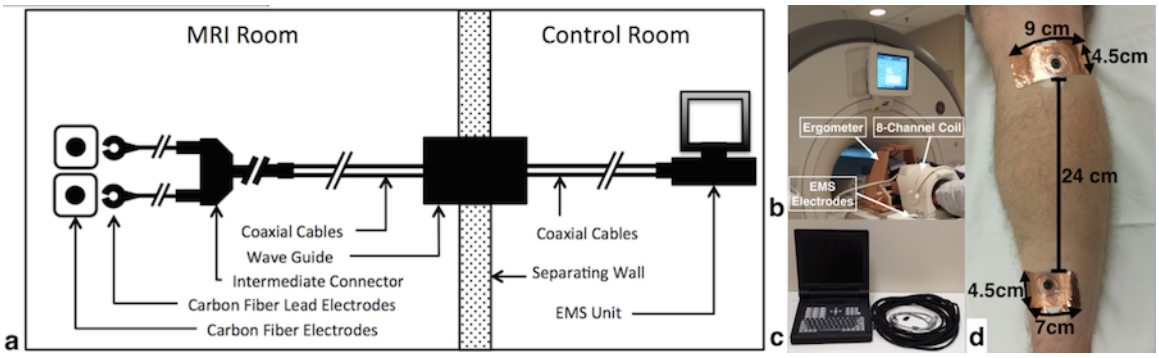

Figure 4.1: Instrumentation setup: **(a)** schematic of the experiment setup showing the modified electrodes and leads proceeding through the MRI waveguide to the clinical EMS unit. **(b)** subject setup with respect to the MRI, ergometer, the coil, and EMS electrodes, **(c)** the EMS unit along the cables, and **(d)** the location of the electrodes on subject's lower leg posterior.

and then in the presence of the electrodes, both with and without stimulatory current (Pulse width: 0.1 ms, 50 mA, and a frequency of 40 Hz). A FIESTA sequence was chosen as it would have one of the highest specific absorption rates (SAR). If electrode placement did not result in heating there would unquestionably be no heating concerns for *in vivo* MRS or BOLD imaging, both of which have significantly lower SAR than FIESTA.

The quality of axial T2* images (TE/TR/flip=35/250ms/33°, 10mm thick, 0mm skip FOV/matrix=16cm/64x64) was assessed temporally and spatially. To investigate whether EMS pulses would interfere with T2* signal, 3 axial slices were prescribed right at the electrode site and 8-minute T2* scans were acquired in the absence of EMS electrodes, and with electrodes and a stimulation regime. The stimulation started 4 minutes into the scan, and was switched off and on in alternating 1-second intervals for 2 minutes to mimic the same EMS paradigm for in vivo scans. Mean T2* signal time-course for both scenarios, over a region of interest (ROI) close to the electrode site, were compared. The T2* signal quality was evaluated to determine whether

EMS pulses could interfere with in vivo BOLD signal acquisition. This is important to set a baseline for the in vivo comparisons. The spatial T2* signal loss due to the presence of electrodes was evaluated as a function of slice-distance from the electrode site. For this purpose, two electrodes were placed about 10 cm away from each other on the phantom. A total of 14 axial slices were prescribed to cover the electrodes and the distance between them and a 4.25-minute axial T2* scan with TR=850 ms was acquired with and without inactive electrodes. Mean T2* image signal from ROIs drawn in 11 slices, starting from one electrode and ending at the other, was compared for both with and without electrodes. From this the SNR change as a function of distance between the two electrodes was calculated for each.

***In vivo* Experiments**

All in vivo experiments were approved by our institutional research ethics board. An in-house built wooden ergometer was used to carry out ankle dynamic plantar flexion in the magnet bore. A total of 5 healthy volunteers (26±2.3 years old) were recruited for both 31P and BOLD MR imaging experiments.

As a proof of concept on the functionality of our modified EMS system, the effects of EMS-induced and voluntary dynamic plantar flexion on PCr in ^{31}P MRS and BOLD signal were compared. The subject's maximum voluntary contraction (MVC) load for ankle dynamic plantar flexion was determined a few days prior to the scan. The location of the motor points were pre- determined using the stimulus threshold contour mapping technique [16,17]. However, because the location of the motor points were on the belly of the muscle and, hence, in the field of view of the imaging plane, it was decided to conduct the muscle contraction by stimulating the tibial never instead. This also helped a more uniform muscle contraction. Copper strips

were placed about 24 cm away from each other on motor points of the superior and inferior heads of the medial gastrocnemius muscle (**Fig.4.1d**). The RF-translucent gel electrodes were placed on top of the copper tape and the subject's foot was fixed in the ergometer. The EMS frequency was set at 40Hz and both the current intensity and muscle load were increased until comfortable dynamic flexion was accomplished producing a 4cm displacement with each contraction. Then the stimulus intensity was increased to 125% and maintained at that level for the stimulation paradigm. The EMS parameters determined for the subject were pulse-width = 0.1ms, frequency = 40 Hz with a load =12% MVC. The ankle dynamic plantar flexion was performed such that it took 1 second to push against the load and 1 second for the foot to go back to rest position i.e. contraction rate of 0.5Hz. In the voluntary exercise, the subjects were asked to replicate the same plantar flexion as EMS at the same rate and load to keep things consistent.

To assess EMS efficacy on muscle metabolism, dynamic ^{31}P-MRS was performed. Spectra of ^{31}P (hard pulse, 6 averages, TR=2 seconds, number of spectral points = 1024, spectral bandwidth = 2000 Hz, 50 temporal points, scan length=10 minutes) were obtained, allowing a time resolution of 12 seconds per time point. The EMS and exercise scanning order was randomized amongst the subjects to rule out any order effect in the results. Muscle activation (i.e. EMS or exercise) was applied at 2 minutes into the dynamic spectral acquisition and continued for 2 minutes, and then 6 minutes of post-stimulation (i.e. rest) ^{31}P data were acquired. A 15-minute rest time was allotted between the EMS and exercise scans. Phosphorous spectra were analyzed using SAGE (GE Healthcare, Milwaukee WI), using 5Hz spectral line broadening and calculating the PCr peak intensity. Changes in the PCr [11], normalized to the

baseline average, were measured for each one-minute time-point in order to compare dynamic changes in high energy phosphates with muscle activation from either EMS and voluntary effort.

In separate acquisitions, BOLD scans were also acquired during EMS and exercise paradigms. The BOLD scan parameters were identical to those used in phantom experiments with TR=250 ms and 4 axial slices placed on the belly of the calf muscle. The EMS and voluntary exercise paradigms consisted of 1.5minutes of baseline images followed by 3 cycles of 2 minutes plantar flexion alternating with 1.5minutes rest. The EMS and exercise scan order was randomized across subjects with 15 minutes of rest between the two scans to avoid order effects. Following acquisition, image motion correction was done using MCFLIRT (www.fmrib.ox.ac.uk/fsl) [18] and mean BOLD signal time-course, averaged over the middle two slices, was measured for different lower leg muscle compartments. The BOLD time course was normalized to the average baseline signal. The 1.5minute post-muscle activation rest periods were normalized to the end of each rest period. In order to compare the EMS BOLD effects to that of voluntary effort, each muscle mean BOLD signal from all three post-muscle activation rest- periods were averaged and standard error calculated.

4.3.4 Results

Under the RF intensive imaging sequence (16min of FIESTA), the temperature increased by 0.7 degrees at the electrode placement site in the absence of the electrodes. In the presence of electrodes, the temperature increased 4.7°C (**Table 4.1**). Figure 4.2a shows the T2* signal during the EMS regime as compared to the signal time-course when electrodes are absent. No interferences are observed from the pulsing

Table 4.1: Test on safety of electrodes with respect to potential RF induced temperature increase. Temperature changes were measured with optical temperature probes placed under each of the electrodes, through 16minutes of an RF intensive high specific absorption rates (SAR) pulse sequence. In the absence of EMS electrodes there was a very small change in temperature of 0.7 degrees C, but in the presence of EMS electrodes a 4.7°C increases over 16 minutes.

Time	EMS Electrodes Absent			STIM Electrodes Non-Active			STIM Electrodes Active		
(min)	Ch1 (°C)	Ch2 (°C)	SAR*	Ch1 (°C)	Ch2 (°C)	SAR*	Ch1 (°C)	Ch2 (°C)	SAR*
0	22.3	22.3	-	21.0	21.0	-	21.8	21.8	-
2	22.4	22.4	5.3	23.4	21.3	5.3	24.2	22.1	5.3
4	22.5	22.5	5.3	24.2	21.5	5.3	25.2	22.5	5.3
6	22.5	22.5	5.3	24.5	21.7	5.3	25.6	22.7	5.3
8	22.6	22.6	5.3	25.0	21.8	5.4	25.9	22.8	5.3
10	22.7	22.7	5.4	25.2	21.9	5.4	26.1	23.9	5.4
12	22.8	22.8	5.4	25.3	22.1	5.4	26.2	23.1	5.4
14	22.9	22.9	5.4	25.6	22.4	5.4	26.4	23.2	5.4
16	23.0	23.0	5.4	25.7	22.5	5.4	26.5	23.3	5.4
ΔT (°C)	0.7	0.7		4.7	1.5		4.7	1.5	

*(W/Kg/10 sec)

EMS on the T2* signal. In terms of image quality the electrodes resulted in a reduction in the T2* signal intensity from the phantom (**Fig.4.2b**). The SNR reduction was highest closest to the electrode site however this improved markedly (only a 10% SNR reduction compared to without electrodes) in slices 4cm or more away from the electrodes (**Fig.4.2b**).

With the safety and image quality understood for our device we were confident our in vivo experiments could be performed. From phosphorous spectra the PCr peak decreased markedly during both EMS (**Fig.4.3a**) and voluntary activation (**Fig.4.3b**), as demonstrated from our temporally acquired ^{31}P spectra. The PCr peak decreased by an average of 13.5±1.8% (n=5), relative to baseline, over a 2-minute period of EMS (**Fig.4.3c**). Similar behaviour in PCr (9.9±0.8% reduction; n=5) was observed

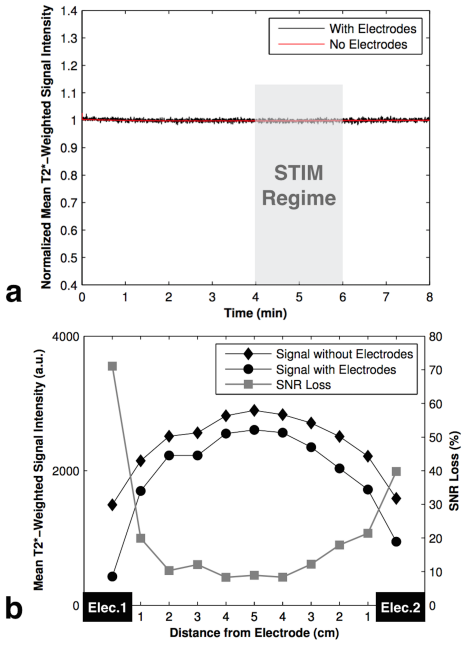

Figure 4.2: The effects of EMS on T2* signal in the absence of physiological confounds. **(a)** Mean T2* signal time-course obtained from an ROI at the electrode site on a phantom with and without electrodes. The shaded area indicates the EMS regime. There was no effect in T2* signal from the EMS activity. **(b)** Mean T2* signal and SNR as a function of presence and absence of electrodes.

when voluntary exercise was performed (**Fig.4.3d**). There was no significant difference in peak changes in PCr when comparing EMS to voluntary muscle activation, based on a paired 2-tailed t-test ($p<0.195$). In the same subjects the BOLD signal reproducibly changed with the three successive bouts of EMS (**Fig.4.4a-f**). This was similar to that seen with the voluntary effort (**Fig.4.5a-f**). Although the temporal trends in BOLD signal changes were similar for both muscle activation strategies, and similar with each muscle, the EMS notably showed a greater increase signal change for both the gastrocnemius (medial, $p<0.03$; and lateral, $p<0.02$) and central soleus ($p<0.03$) (**Fig.4.6**). Even though there were subtle BOLD signal changes ($\sim$2-3%) in the peroneus and anterior tibialis muscles following both EMS and voluntary muscle contraction, no difference between these approaches were noted for these muscles. The greatest percent change in BOLD signal, following contraction, was seen for the central soleus during EMS (10.1$\pm$2.5%). This was notably greater than the voluntary activation done in the same muscle (4.9$\pm$1.2% increase) (**Fig.4.6**).

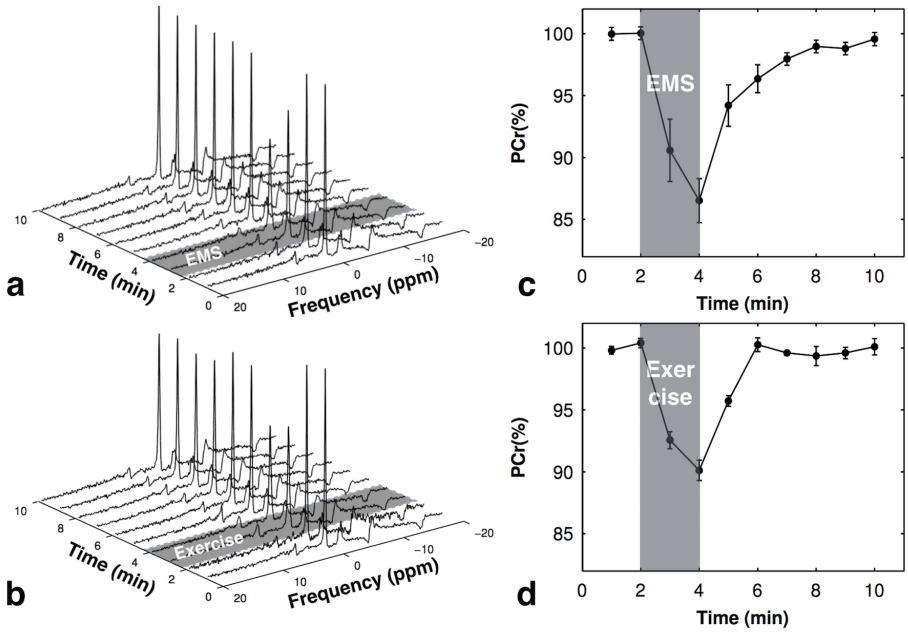

Figure 4.3: ^{31}P time course. Mean ^{31}P spectra obtained from calf muscles of healthy volunteers (n=5, three replicates each) before, during, and following **a)** EMS and **b)** exercise. Mean±SE PCr intensity time curves obtained from 5 subjects before, during, and following **c)** EMS and **d)** exercise. The EMS and exercise periods are indicated with the shaded areas.

4.3.5 Discussion

Any time a device is modified for use in an MRI environment, issues such as patient safety, potential impact of the device on the MR signal, and maintaining the device efficacy post- modification become a concern. The EMS unit used in this study (pre-modification) was approved by regulatory bodies (CSA, Health Canada, FDA) governing the usage of electrical devices with humans. So the primary concern was that of the modification (i.e. electrodes, and extension wires) used. Conventional clinically used EMS electrodes are generally made of silver/silver chloride, which leads to increased RF deposition and potential tissue heating and reduced B0 field homogeneity. Our design made use of RF-translucent electrodes typically used in

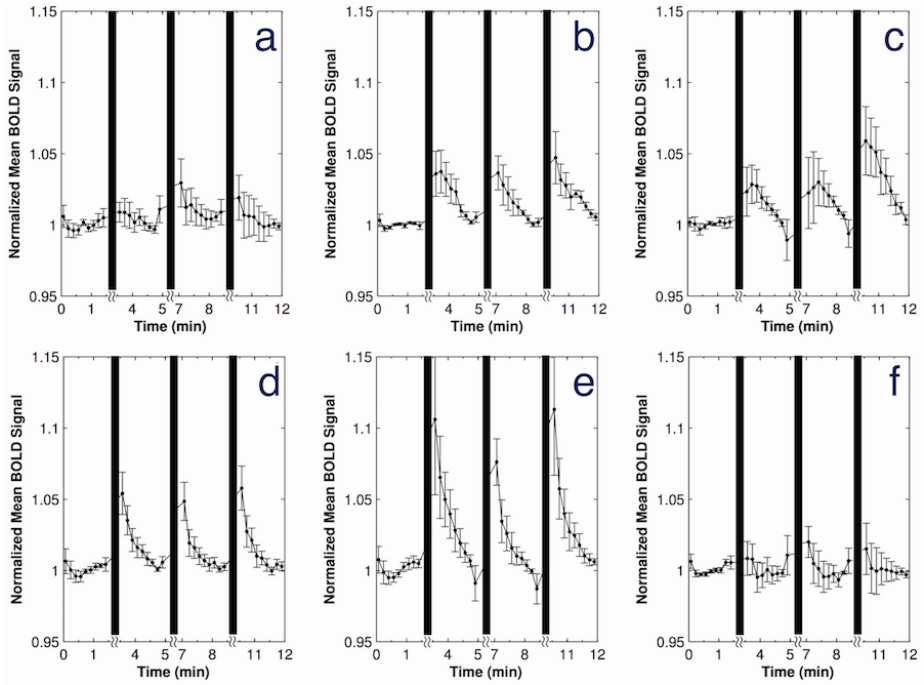

Figure 4.4: Mean± SE (n=5, with three replicates each) in vivo BOLD signal time-course, showing the effect of three successive periods of electrical muscle stimulation (EMS) on muscles of the lower leg **(a)** anterior tibialis, **(b)** lateral gastrocnemius, **(c)** medial gastrocnemius, **(d)** central soleus, **(e)** central soleus, **(f)** peroneus. Although the BOLD signal was sampled every 250ms the time points in the graphs are shown in 10s intervals to avoid cluttering.

MRI environments for recording physiological signals such as electrocardiography. As these electrodes are used primarily for recording rather than stimulating, safety and device functionality tests were required.

In order to rule out the possibility of excessive RF heating, we acquired optical temperature measurements at the electrode sites during an RF-intensive imaging sequence applied for 16 minutes. For a 10-second average SAR level of 5.4 W/kg, we observed a temperature increase of 4.7 degrees in the presence of the electrodes. Considering the MRI scanner reported 10-second average SAR for our in vivo BOLD protocol as 0.0 W/kg, we concluded the presence of electrodes would not cause any

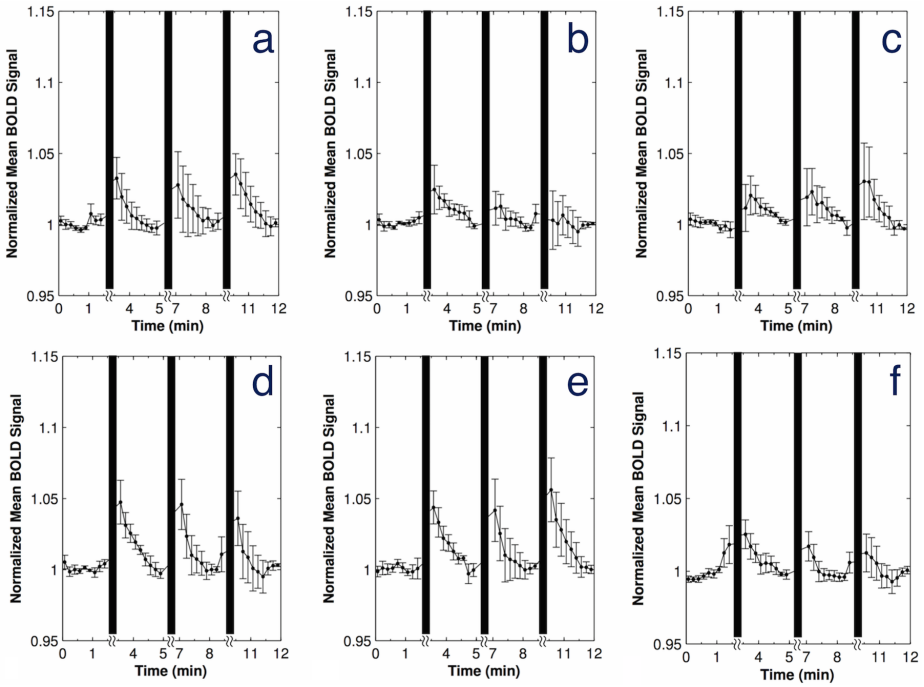

Figure 4.5: Mean±SE (n=5, with three replicates each) in vivo BOLD signal time-course, showing the effect of three periods of successive voluntary exercise on muscles of the lower leg **(a)** anterior tibialis, **(b)** lateral gastrocnemius, **(c)** medial gastrocnemius, **(d)** lateral soleus, **(e)** central soleus, **(f)** peroneus. Although the BOLD signal was sampled every 250ms the time points in the graphs are shown in 10s intervals to avoid cluttering.

RF heating concerns for human subjects. Furthermore, in the debriefing following in vivo MRI experiments presented in this study, the test subject reported no perceived change in temperature at electrode sites.

To assess the effects of EMS on BOLD signal quality, we acquired images simultaneously with EMS pulses, first on a phantom in order to eliminate potential confounding physiological processes. In comparing the signal time-course of the electrode-present condition with that of electrode-absent, EMS did not appear to alter the phantom T2* signal, whether stimulation was active or not. However, it was observed that the presence of an electrode attenuates BOLD signal spatially

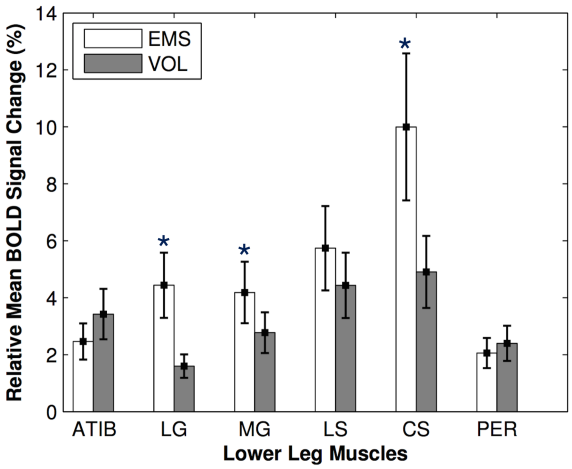

Figure 4.6: Relative in vivo BOLD signal changes obtained from averaging the three post-muscle activation rest periods of all individuals for each lower leg muscles. The EMS notably showed a greater increase in BOLD signal change for both the gastrocnemius (medial, $p<0.03$; and lateral, $p<0.02$) and central soleus ($p<0.03$). The greatest percent change in BOLD signal, following contraction, was seen for the central soleus during EMS (10.1±2.5%). This was notably greater than the voluntary activation done in the same muscle (4.9±1.2% increase). ATIB=Anterior Tibialis, LG=Lateral Gastrocnemius, MG=Medial Gastrocnemius, LS=Lateral Soleus, CS=Central Soleus, PER=Peroneus. (* = $p<0.05$)

where SNR attenuation was as high as 70% proximal to the electrode, diminishing to below 10% at 4 cm (i.e. four slices) distal from the site. This suggests the location of the desired imaging slice with respect to electrode site is important, and that to avoid large electrode-induced SNR losses, the imaging slice should be kept at least 4 cm away from the electrode.

In order to demonstrate the ability of EMS to induce muscle metabolic changes, ^{31}P MR spectroscopy was performed. Previous studies with EMS [8-10] have shown that, like in voluntary contraction, PCr is hydrolysed, releasing inorganic phosphate (Pi) to regenerate ATP levels that are depleted during contraction. The amount of PCr breakdown depends on a number of factors such as EMS intensity and frequency,

and muscle type and its fibre type composition. These previous studies were done on forearm and quadriceps muscles. Our results from calf muscle show similar behaviour, i.e. hydrolysis of PCr during delivery of EMS. The reduced PCr during EMS was greater than that of voluntary exercise which confirms our modified EMS system effectively induces metabolic changes.

Muscle BOLD signal during EMS and voluntary contractions demonstrated rapid change due to the induced contractile motion within the muscle. However, upon cessation of contraction the increased BOLD signal subsequently returned to rest state as similarly observed in other muscle BOLD studies [19, 20]. Consistent BOLD signal changes were observed after each 2-minute EMS and voluntary effort. The greatest EMS BOLD signal changes were observed in the medial gastrocnemius and lateral and central soleus muscles while peroneus muscle showed the least BOLD signal change relative to other muscles, for both EMS and voluntary contraction. As gastrocnemius and soleus are the dominant muscles responsible for ankle plantar flexion, it was not surprising the greatest BOLD signal changes were observed there. As the shapes of BOLD signal recovery curves appear reproducible following each EMS phase, and they are similar to that seen from voluntary exercise, our modified unit was deemed to be functioning as desired. Based on a recent comparison of voluntary compared to EMS activation of muscle the EMS approach provides a much more effective activation [21]. This is also evident from our results where BOLD signal change due to EMS was greater compared to voluntary exercise for all muscles investigated except anterior tibialis. This may be due to differences between the nature of EMS and voluntary muscle activation in that EMS might not have been able to activate anterior tibialis as much as voluntary effort had. The signal return

to baseline is not fully understood, however, it is most likely a combination of return to basal blood flow and volume (hence a decrease in local oxyhemoglobin) with a physical return of muscle fibres to basal/rest location [22].

The area of typical RF-translucent adhesive gel electrodes is small (about 2.2 cm in diameter) compared to regular EMS electrodes (eg. www.axelgaard.com) and would thus not be able to stimulate an entire muscle. In order to address the potential impact of electrode surface area, we decided to use rectangular copper strips with conductive adhesive to increase electrode surface area providing a more uniform muscle contraction. For this reason copper strips (area of 4.5x9 cm2 and 4.5x7 cm2, with the ground electrode being the smaller of the two) were placed on the superior and inferior heads of the gastrocnemius, respectively. The electrode sizes were iteratively decided upon by choosing a size resulting in maximal contraction with minimal EMS current; that is, a size that covered the motor point best and offered the best contraction for the least stimulus intensity. Our goal was a contracting calf muscle with enough force to induce dynamic plantar flexion forcing the foot to comfortably push against a load of 12% MVC.

The use of EMS in the study of muscle dynamics entails some constraints due to safety limits regarding intensity and frequency of stimulation. In conventional voluntary exercise studies, a percentage of maximum voluntary contraction (MVC) can be determined and subsequently used across different subjects. Calibrating EMS intensity across different subjects is challenging, as low intensities do not activate muscle contraction, while high intensities are constrained by subject pain threshold and potential injury. Furthermore, this calibration may be hampered by anatomical features such as the presence of subdermal fat, which increases EMS impedance and

limits the effect of stimulation upon the muscle. Our volunteers all had BMI values lower than 25kg/m^2 making this test relatively straightforward. However, finding a measure of EMS that can be applied proportionately to individual subjects, with varying BMI and subcutaneous fat content is a complex problem. In our study, since the participants were healthy and able to carry out voluntary ankle dynamic plantar flexion, we were able to measure MVC and use that to quantify the amount of contractile force induced by EMS. For subjects with an inability to perform voluntary contractions, a potential workaround could be the use of a muscle dynamometer to measure the amount of force induced by EMS, and to adjust the stimulation intensity to achieve the same torque among different subjects.

Choosing the frequency of EMS is another challenging aspect of this technique, as it affects how different muscle fibres are recruited [6]. For instance, EMS frequencies in the range of 2-15Hz mostly stimulate slow twitch fibres whereas fast-twitch fibres may not be stimulated below 35Hz [6]. However, relating the frequency to muscle fibre type is a popular misconception. The reason a muscle is considered to be fast or slow twitch muscle is due to the size of the supplying motor axon. The main purpose of this study was simply to demonstrate the ability of our modified EMS unit to impact muscle physiological processes as measured using BOLD signals and 31P-MRS. As we have shown here, an inexpensive modification to a standard clinical EMS system can provide safe MRI compatibility. Thus optimization of EMS protocols for catering to different frequencies can now easily be done in future studies.

There are many potential clinical uses for combining MRI with simultaneous EMS. For example, this technique could be used to examine oxygenation changes in a limb

affected by peripheral vascular disease (PVD) during stimulation, rather than the current approach of reactive hyperemia. Both BOLD MRI and ^{31}P-MRS in conjunction with EMS could be used to ascertain viable muscle within a diseased limb, thus determine the prognosis of an amputation with better certainty. Another clinical use could be to complement and refine the current diagnostic procedures for muscle disorders such as enzymatic defects or channelopathies which currently rely upon EMG and biopsy. The main advantage of this technique is that it is non-invasive. The addition of EMS-MRI to diagnostic practice could be of value in its ability to provide evidence of the extent of anaerobic metabolism following exercise. A final potential use for this technology could be in a patient who does not have the cardio-respiratory capacity to exercise, if exercise is contra-indicated medically, or if a patient has suffered neuronal damage and is unable to voluntarily contract muscle.

The potential clinical MRI application of EMS is not limited to BOLD as a means of study of muscle physiology. While BOLD MRI is capable of assessing PVD, physical parameters such as muscle length, velocity changes, and deformation are other key factors in evaluating muscle function. There have been studies such as cine phase contrast [23], anatomical imaging and registration [24,25], and diffusion tensor imaging [26] that have utilized these physical parameters in conjunction with voluntary muscle exercise to evaluate muscle function. An MRI compatible EMS system provides controlled, repeatable and reproducible muscle contraction. Hence, EMS could potentially enhance the outcome of such MRI techniques.

In conclusion, simultaneous EMS and MRI techniques such as BOLD imaging and ^{31}P- MRS were conducted in a safe manner without significant interference or heating issues using a simple set-up, thus enabling reliable quantitative and repeatable

activation of muscle.

4.3.6 References

1. Kramer JF and Mendryk SW. Electrical stimulation as a strength improvement technique: a review. J Orthop Sports Phys Ther 1982; 4:1657-1667.

2. Hortobgyi T, Scott K, Lambert J, Hamilton G, Tracy J. Cross-education of muscle strength is greater with stimulated than voluntary contractions. Motor Control 1999; 3:205-219.

3. Delitto A, Rose SJ, McKowen JM, Lehman RC, Thomas JA, Shively RA. Electrical stimulation versus voluntary exercise in strengthening thigh musculature after anterior cruciate ligament surgery. Phys Ther 1988; 68:660-663.

4. Snyder-Mackler L, Delitto A, Bailey SL, Stralka SW. Strength of the quadriceps femoris muscle and functional recovery after reconstruction of the anterior cruciate ligament: A prospective, randomized clinical trial of electrical stimulation. J Bone Joint Surg Am. 1995; 77:1166-1173.

5. Bergquist AJ, Wiest MJ, Collins DF. Motor unit recruitment when neuromuscular electrical stimulation is applied over a nerve trunk compared with a muscle belly: quadriceps femoris. J Appl Physiol. 2012; 113:78-89.

6. Filipovic A, Kleinder H, Drmann U, Mester J. Electromyostimulation- a systematic review of the influence of training regimens and stimulation parameters on effectiveness in electromyostimulation training of selected strength parameters. J Strength Cond Res. 2011; 25:3218-3238.

7. Chance B, Leigh JS Jr, Clark BJ, Maris J, Kent J, Nioka S, Smith D. Control of oxidative metabolism and oxygen delivery in human skeletal muscle: a steady-state

analysis of the work/energy cost transfer function. Proc. Nat. Acad. Sci. USA 1985; 82:8384-8388.

8. Chance B, Leigh JS Jr, Kent J, McCully K, Nioka S, Clark BJ, Maris JM, Graham T. Multiple controls of content was observed. Blood flow alterations resulting oxidative metabolism of living tissues as studied by 31P-MRS. Proc. Nat. Acad. Sci. USA 1986; 83:9458-9462.

9. Blei ML, Conley KE, Odderson IB, Esselman PC, Kushmerick MJ. Individual variation in contractile cost and recovery in a human skeletal muscle. Proc Natl Acad Sci USA. 1993; 90:7396-7400.

10. Jeneson JA, Wiseman RW, Kushmerick MJ. Non-invasive quantitative 31P MRS assay of mitochondrial function in skeletal muscle in situ. Mol Cell Biochem. 1997; 174:17-22.

11. Vanderthommen M, Duteil S, Wary C, Raynaud JS, Leroy-Willig A, Crielaard JM, Carlier PG. A comparison of voluntary and electrically induced contractions by interleaved 1H-and 31P-NMRS in humans. J Appl Physiol. 2003; 94:1012-1024.

12. Adams GR, Harris RT, Woodard D, Dudley GA. Mapping of electrical muscle stimulation using MRI. J App Physiol. 1993; 74:532-537.

13. Ogino M, Shiba N, Maeda T, Iwasa K, Tagawa Y, Matsuo S, Nishimura H, Yamamoto T, Nagata K, Basford JR. MRI quantification of muscle activity after volitional exercise and neuromuscular electrical stimulation. Am J Phys Med Rehabil. 2002; 81:446-451.

14. Noseworthy MD, Davis AD, Elzibak AH. Advanced MR imaging techniques for skeletal muscle evaluation. Sem. Musculoskel. Radiol. 2010; 14:257-268.

15. Ratkevičius A, Mizuno M, Povilonis E, Quistorff B. Energy metabolism of the

gastrocnemius and soleus muscles during isometric voluntary and electrically induced contractions in man. J Physiol. 1998;507(2):593-602.

16. Botter A, Oprandi G, Lanfranco F, Allasia S, Maffiuletti N a., Minetto MA. Atlas of the muscle motor points for the lower limb: Implications for electrical stimulation procedures and electrode positioning. Eur J Appl Physiol. 2011;111(10):2461-2471.

17. Gobbo M, Maffiuletti N a, Orizio C, Minetto M a. Muscle motor point identification is essential for optimizing neuromuscular electrical stimulation use. J Neuroeng Rehabil. 2014;11(1):17.

18. Jenkinson M, Bannister P, Brady JM, Smith SM. Improved optimisation for the robust and accurate linear registration and motion correction of brain images. NeuroImage. 2002; 17:825-841.

19. Schewzow K, Andreas M, Moser E, Wolzt M, Schmid AI. Automatic model-based analysis of skeletal muscle BOLD-MRI in reactive hyperemia. J Magn Reson Imaging. 2013;38(4):963-969.

20. Caterini JE, Elzibak AH, Michel EJ St., et al. Characterizing blood oxygen level-dependent (BOLD) response following in-magnet quadriceps exercise. Magn Reson Mater Physics, Biol Med. 2015;28(3):271-278.

21. Akbari A, Rockel CP, Kumbhare DA, Noseworthy MD. (2013) An MR-compatible solution for simultaneous electrical muscle stimulation and MR imaging at 3T. Proceedings of the International Society for Magnetic Resonance in Medicine (ISMRM). 2013; 21:3560. Salt Lake City, UT.

22. Davis AD, Noseworthy MD. Haemoglobin-derived curve fitting to post-exercise muscle bold data. Proceedings of the International Society for Magnetic Resonance in Medicine (ISMRM). 2013; 21:5311. Salt Lake City, UT.

23. Asakawa DS, Blemker SS, Gold GE, Delp SL. In vivo motion of the rectus femoris muscle after tendon transfer surgery. J Biomech. 2002;35(8):1029-1037.

24. Huijing P a., Yaman A, Ozturk C, Yucesoy C a. Effects of knee joint angle on global and local strains within human triceps surae muscle: MRI analysis indicating in vivo myofascial force transmission between synergistic muscles. Surg Radiol Anat. 2011;33(10):869-879.

25. Yaman A, Ozturk C, Huijing P a, Yucesoy C a. Magnetic resonance imaging assessment of mechanical interactions between human lower leg muscles in vivo. J Biomech Eng. 2013;135(9):91003.

26. Heemskerk AM, Sinha TK, Wilson KJ, Ding Z, Damon BM. Repeatability of DTI-based skeletal muscle fiber tracking. NMR Biomed. 2010;23(3):294-303.

Chapter 5

Dynamic Measurement of Exercise Induced Changes in Human Calf Muscle Intracellular and Total Sodium (^{23}Na) Content

Alireza Akbari M.Eng., Dinesh A. Kumbhare MD, M.Sc., FRCPC, Alex D. Bain, Ph.D., and Michael D. Noseworthy Ph.D., P.Eng.

5.1 Context of the Paper

This paper describes a novel method to non-invasively evaluate human skeletal muscle functional dynamics through changes seen in total and bound intracellular sodium content. Contracting muscle, at near real-time temporal resolution, was evaluated before, during and immediately following exercise using ^{23}Na magnetic resonance

spectroscopy (MRS). This non-invasive method is able to capture acute healthy muscle functional changes that are not possible with any other non-invasive technique. Only muscle biopsy could provide similar information, albeit at the expense of the patient/subject loosing muscle tissue (i.e. through serial biopsy).

5.2 Declaration Statement

This work is a manuscript now prepared in final form for submission to an imaging journal. Alireza Akbari coded and implemented the ^{23}Na triple quantum filtered (TQF) pulse sequence on a GE Healthcare 3Tesla MRI, built the transmit/receive split birdcage ^{23}Na radiofrequency (RF) coil, and with the help of Conrad Rockel upgraded the custom-built MRI-compatible wooden ergometer to fit and function inside the MRI (after the scanner had a major hardware and software upgraded from v.12.0 to v.22.0). Alireza Akbari also, as principle author, wrote the first draft of the manuscript, collected the data, performed analysis and created figures. Michael D. Noseworthy, as corresponding author, provided the concept for the paper, funding and advice, and performed substantial editing to prepare the manuscript for submitting for publication. Dr. Kumbhare helped with clinical advice and editing, guidance and commentary. Dr. Bain helped with editing, guidance and commentary.

5.3 Paper

Dynamic Measurement of Exercise Induced Changes in Human Calf Muscle Intracellular and Total Sodium (^{23}Na) Content

Alireza Akbari MEng[1], Dinesh A. Kumbhare MD, MSc, FRCPC[2], Alex D. Bain, PhD[3], and Michael D. Noseworthy PhD PEng[1,4]

[1]*School of Biomedical Engineering, McMaster University, Hamilton, Ontario, Canada;*
[2]*Toronto Rehabilitation Institute, Faculty of Medicine, University of Toronto, Toronto, Ontario, Canada;*
[3]*Department of Chemistry and Chemical Biology, McMaster University, Hamilton, Ontario, Canada;*
[4]*Electrical and Computer Engineering, McMaster University, Hamilton, Ontario, Canada;*

Address for correspondence:

Dr. Michael D. Noseworthy, PhD PEng

Electrical and Computer Engineering

Engineering Technology Building, Room 406

McMaster University

1280 Main Street West., Hamilton, Ontario, Canada. L8S 4K1

VOICE: (905) 525-9140 x23727

EMAIL: nosewor@mcmaster.ca

Running Title: Sodium MR spectroscopy of exercising muscle

5.3.1 Abstract

In vivo magnetic resonance spectroscopy and imaging (MRS and MRI) studies have shown that total sodium content increases in muscle, post exercise. However, dynamic assessments of intracellular and total sodium changes at the beginning of and during exercise have not ever been reported. Such information could be highly useful in noninvasive evaluation of a host of muscle diseases. In our study, triple-quantum filtered (TQF) ^{23}Na magnetic resonance spectroscopy (MRS), an indicator of tissue's bound intracellular sodium content, and single-quantum filtered (SQF) MRS, which represents total ^{23}Na, were used to assess the dynamics of healthy human calf muscles (n=9) during 2 minutes of exercise and subsequent 10 minutes of recovery. Spectra were acquired every 12 seconds. The TQF signal significantly decreased (6.8±1.3% ; $p<0.001$) during exercise, recovering immediately post-exercise to overshoot and then return to baseline. Concurrently, the SQF signal initially dipped and then increased by 3.6±0.6% ($p<0.001$) with exercise, and slowly recovered back to baseline post exercise. Our results show ^{23}Na TQF and SQF complement each other; the TQF approach is best in assessing ^{23}Na during contraction while SQF is best for assessing exercise recovery.

5.3.2 Introduction

^{23}Na is a 100% abundant naturally occurring isotope of sodium. It is the most prevalent cation in the body and as such plays a pivotal role in cellular physiological processes. In health, the body actively maintains a trans-membrane sodium gradient which keeps intracellular sodium $[Na^+]_i$ at approximately 10 to 15 mM and extracellular sodium $[Na^+]_e$ around 145 mM (1). This concentration gradient is maintained

by energy-consuming Na^+/K^+-ATPase. ^{23}Na possesses a nuclear spin quantum number of I=3/2 and a quadruple moment due to its spherically asymmetric nucleus. The quadruple moment interacts with surrounding electric field gradients (EFG) (i.e. quadrupolar interactions). In an external magnetic field, ^{23}Na nuclei can orient themselves in four possible energy states. Depending on the ^{23}Na molecular environment, there may be single, double, and triple quantum transitions occurring between energy states. In liquids, ^{23}Na quadrupolar interactions average to zero leading to mono-exponential nuclear magnetic resonance (NMR) transverse relaxation under single-quantum (SQ) transitions. In biological tissues, macromolecules and membrane surfaces exhibit an EFG that extends in space on the order of 10 nm (2). As a result, quadrupolar interactions do not average to zero and multiple-quantum (MQ) transitions with biexponential transverse relaxation are observed. A conventional single pulse- acquire 23Na sequence detects only SQ transitions, while double, and triple quantum transitions can be detected through MQ filtered (MQF) techniques (3).

Because ^{23}Na is extremely sensitive to the surrounding EFG it is a perfect candidate for the in vivo study of human tissues such as muscle since any physiological changes in skeletal muscle tissue should be reflected in altered ^{23}Na content and NMR transverse relaxation properties. Previous studies have shown altered ^{23}Na concentration following exercise in healthy subjects (4, 5,6), in subjects with diabetes (4), and in myotonic dystrophy (6). In these studies, the ^{23}Na MRI signal (i.e. SQF signal) was a reflection of tissue total sodium content (TSC), a weighted sum of intra- and extracellular sodium compartments. Hence, it is difficult to say whether altered SQF ^{23}Na signal intensity is due to changes in intra- or extracellular or both compartments.

The intracellular compartment makes up approximately 80% of tissue volume

(7), depending on tissue type. Also, relative to extracellular, the intracellular space is highly concentrated with macromolecules, up to 23% (8). As a result, ^{23}Na quadrupolar interactions are more pronounced intracellularly. Since MQF ^{23}Na MR detects only MQ transitions, it contains mostly the intracellular ^{23}Na signal (9,10) providing a means of probing intracellular physiological processes. The application of triple-quantum filtered (TQF) ^{23}Na MR spectroscopy (MRS) has previously been demonstrated in healthy human calf muscle (11) and in myotonic dystrophy (12). The same technique could also be applied in exercise physiology.

Currently, studies that investigate dynamic metabolic changes in skeletal muscle are done through serial muscle biopsies. These studies are limited by a few important factors: first, muscle biopsy leads to disruption of the cellular membrane and in vivo ionic/metabolic states. Second, the acute effect of exercise would be lost by the time the sample is examined. Third, since these methods involve biopsies, reproducibility and repeatability are difficult to ascertain because repeated measures on the same muscle piece are not possible. On the other hand, TQF ^{23}Na MRS does not have these issues. The ability of TQF ^{23}Na MRS in resolving intra from extracellular ^{23}Na signal would provide valuable non-invasive insight into intracellular physiological processes in response to exercise with a time-resolution of several seconds. Thus the goal of this study was to investigate acute effects of exercise on healthy human muscle TQF ^{23}Na signal intensity, and to compare these results with SQF ^{23}Na signal. This study provides a unique and novel means to probe dynamic changes in skeletal muscle sodium content right at the exercise onset, during, and immediately after exercise sensation.

5.3.3 Materials and Methods

All data acquisitions were performed using a GE Discovery MR750 3T (General Electric Healthcare, Milwaukee WI) with a custom-made 15cm diameter transmit/receive sodium radiofrequency (RF) surface coil. An in-house designed and built MRI compatible ergometer was used for ankle plantar flexion exercise inside the MRI bore, concurrent with MR scans. All data analysis were performed using MATLAB (Mathworks Natick, MA, USA (version R2014A)).

Subject Setup

A total of nine healthy normal subjects (7 male and 2 female, mean age = 26.3±4.5 years) were recruited. Subjects were positioned supine in the magnet bore with one leg placed in the ergometer pedal and RF surface coil horizontally positioned under the calf muscle belly. The leg and coil were immobilized using a strap tied to the either side of the MR bed. The exercise protocol consisted of a two-minute ankle plantar flexion at frequency of 0.5Hz while pushing against a load of 30% of subject's maximum voluntary contraction (MVC), as determined the day before. To investigate the effects of exercise on SQF and TQF ^{23}Na signal before, during, and after exercise, both SQF and TQF ^{23}Na MRS protocols were designed to cover a two-minute baseline, two-minute exercise, and 10-minute recovery regimes.

Sequence Parameters

For a point-to-point comparison between SQF and TQF data across time, the same acquisition parameters were used for both SQF and TQF sequences (i.e. TR = 166.7ms, number of complex points = 1024, and spectral bandwidth = 15.625kHz, hard pulse

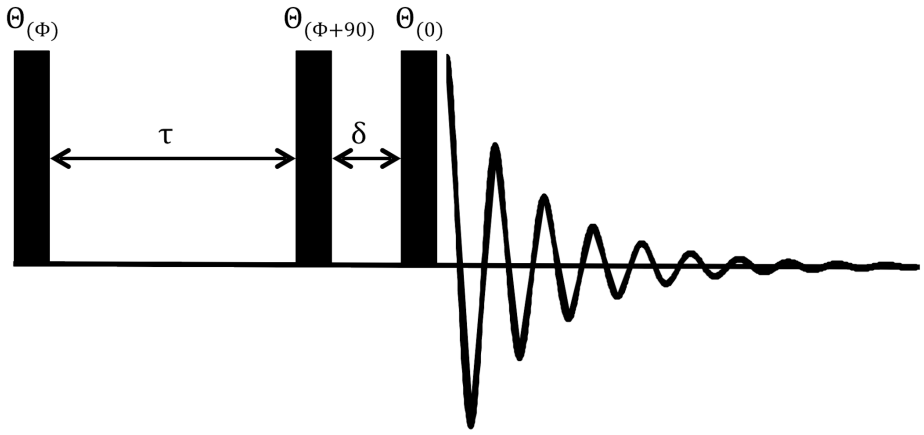

Figure 5.1: TQF ^{23}Na pulse sequence diagram consisting of three $\theta = 90°$ excitation pulses with six-step phase cycling $\phi = 30°, 90°, 150°, 210°, 270°, 330°$. The creation time τ is optimized to give maximum signal while the evolution time δ is kept as short as possible (156μs). Diagram is not to scale.

width = 500μs, flip angle = 90°). SQF ^{23}Na spectra were collected using a standard pulse-acquired vendor-provided sequence (FIDCSI). The number of signal averages was set to 6 while the radiofrequency (RF) pulse phase was alternated between 0° and 180°, between each acquisition. TQF ^{23}Na spectra were collected using a three-pulse TQF sequence with six-phase cycling steps (3): $\theta(\phi) - \tau - \theta(\phi + 90) - \delta - \theta(0) -$ Acquisition (**Fig. 5.1**), where $\theta = 90°, \phi = 30°, 90°, 150°, 210°, 270°, 330°$, and τ and δ being the creation and evolution times, respectively. Conventionally, spectroscopic areas are measured by spectral curve fitting to reduce errors due to overlapping peak shoulders in the spectrum. However, the SQF and TQF spectra each possess only one peak, simplifying curve fitting. But, in anisotropic environments such as biological tissues, the TQF ^{23}Na absorptive lineshape is more complicated relative to SQF. The TQF ^{23}Na absorptive lineshape is the difference of two Lorentzians with equal areas but different widths resulting in one central and two satellite bands (3). Hence, it is more convenient to first fit the TQF free induction decays (FIDs) to a time signal

model, Fourier transform the fitted data, and then calculate the area of the absorptive lineshape. To be consistent in post processing, the same procedure was done for SQF FIDs. As a result, the SQF FIDs were fitted to the following biexponential decay function (13,14):

$$M_{xy} = Ae^{-t/T_{2s}^*} + Be^{-t/T_{2f}^*} [\mathbf{1}]$$

where A and B are the signal intensity contributions of fast and slow component, and T_{2f}^*, and T_{2s}^* are the fast and slow transverse relaxation times in the presence of magnetic field inhomogeneity, respectively. The fitted SQF FIDs were Fourier transformed and peak areas of the absorptive lineshapes were determined. The TQF ^{23}Na FID was modeled as follows (15):

$$M_{xy} = M_0 K_{TQ}(e^{-\tau/T_{2s}^*} - e^{-\tau/T_{2f}^*})e^{\delta/T_{TQ}} cos(3\omega\delta)(e^{-t/T_{2s}^*} - e^{-t/T_{2f}^*})[\mathbf{2}]$$

where M_0 is the equilibrium longitudinal magnetization, K_{TQ} is a TQ-specific constant equal to 9/40, T_{2f}^*, and T_{2s}^* are the fast and slow transverse relaxation times in the presence of magnetic filed inhomogeneity, respectively, and T_{TQ} is the T_2^* for the TQ transition. The creation time τ and evolution time δ are pulse sequence parameters (**Fig.5.1**). The TQF signal can be maximized by optimizing τ and minimizing δ (for our scanner this was 156μs). To optimize τ, two series of TQF spectra were collected from two subjects at 10 values of τ ranging from 1 to 10ms. Each incremental value of τ was based on an average of 60 spectra acquired over 60 seconds. The value that yielded the highest signal intensity, based on peak area, was then chosen for all subsequent TQF experiments. This procedure was repeated while subjects were performing plantar flexion to see if the optimal τ would differ as a result of exercise.

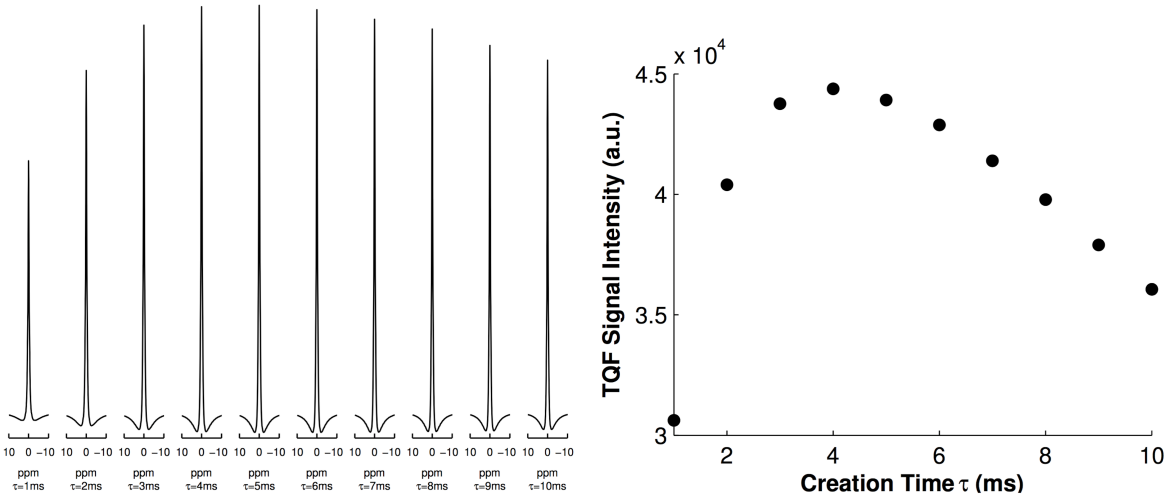

(a) (b)

Figure 5.2: Creation time τ measurements. (a) TQF ^{23}Na spectra measured with various creation times (τ=1, ... ,10 ms). The spectra were collected from subject's calf muscle at rest for 1 minute. (b) Mean TQF ^{23}Na signal intensity as a function of creation time τ. The spectra were collected from two subjects' calf muscles at rest for 1 minute and the mean of signal intensity for each creation time τ was calculated. Note that TQF ^{23}Na signal intensity reaches its maximum at $\tau = 4$ ms.

To account for potential order effects during exercise, τ values were chosen in random order, while evolution time δ was kept minimal (i.e. $\delta = 156\mu s$). After incrementing τ, the optimum value that yielded the maximal TQF ^{23}Na signal intensity was 4 ms (**Fig.5.2**). This value was then used in all subsequent experiments. Once τ, and δ were determined, equation [**2**] could be simplified:

$$M_{xy} = A(e^{-t/T^*_{2s}} - e^{-t/T^*_{2f}})[\mathbf{3}]$$

where A represents the effective value of all constant terms in equation [**2**]:

$$A = M_0 K_{TQ}(e^{-\tau/T^*_{2s}} - e^{-\tau)/T^*_{2f}})e^{\delta/T_{TQ}} cos(3\omega\delta)[\mathbf{4}]$$

The TQF ^{23}Na FIDs were fitted to [**3**]. The fitted FIDs were then Fourier transformed and peak areas were determined from the magnitude of the absorption lineshapes (Winter and Bansal (2001)).

5.3.4 Results

The TQF ^{23}Na FIDs showed a clear signal reduction during exercise, which was reproducible in all subjects. This effect was noted in the raw TQF ^{23}Na FIDs (**Fig.5.3a**) and corresponding TQF ^{23}Na absorption frequency spectra (**Fig.5.3b**). Figure 5.3c-d reflect such changes following exercise. These figures show a summation of 60 FIDs taken during the immediate minute before, the first minute during, the first minute immediately after exercise. The corresponding effect in the SQF FID was much smaller and the change from baseline was not as profound as with the TQF scans (**Fig.5.3e-f**). The QF ^{23}Na MRS measurements showed that exercise had profound and consistent effects on both SQF and TQF ^{23}Na MRS signals intensities (**Fig.5.4**). The SQF ^{23}Na signal intensity, representing total sodium content, initially dropped 2.0±0.7% (p=0.010) within the first 12 seconds of exercise. However, the signal polarity then reversed to increase during the two-minute course of exercise reaching a maximum of 3.6±0.6%, (p<0.001) 24 seconds after exercise cessation. The SQF signal returned to baseline following 16 minutes of rest. Comparatively, the intracellular sodium signal, obtained from the TQF ^{23}Na MRS amplitude, significantly dropped by 6.8±1.3% (p<0.001) in the first 24 seconds into the exercise period. The signal remained low until cessation of exercise at which point the signal recovered, overshooting baseline levels by 1.3±0.8%, albeit without statistical significance (p=0.065) 24 seconds after exercise cessation.

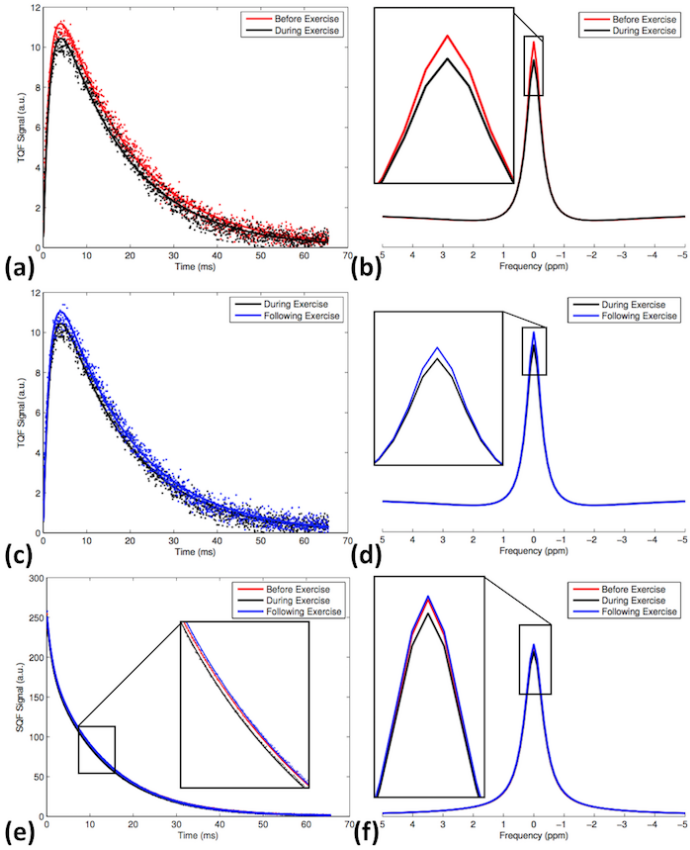

Figure 5.3: TQF and SQF FIDs and spectra under the influence of Exercise. (a,c)TQF and (e)SQF ^{23}Na FIDs acquired before (red), during (black), and following exercise (blue). The raw data is represented by dots and the fitted curve by solid lines. (b,d) The corresponding TQF and (f) SQF ^{23}Na MR spectra representing magnitude of the absorption curves, respectively.

5.3.5 Discussion

To the best of our knowledge, this is the first time dynamic non-invasive measures of muscle intracellular and total sodium during and following exercise has been shown. The study results indicate that both SQF and TQF ^{23}Na signals are affected by exercise. However, these effects manifest themselves differently in the SQF and TQF ^{23}Na signal time courses. The results suggest that TQF ^{23}Na MRS may be a very sensitive tool for assessing dynamic changes in muscle at a cellular level.

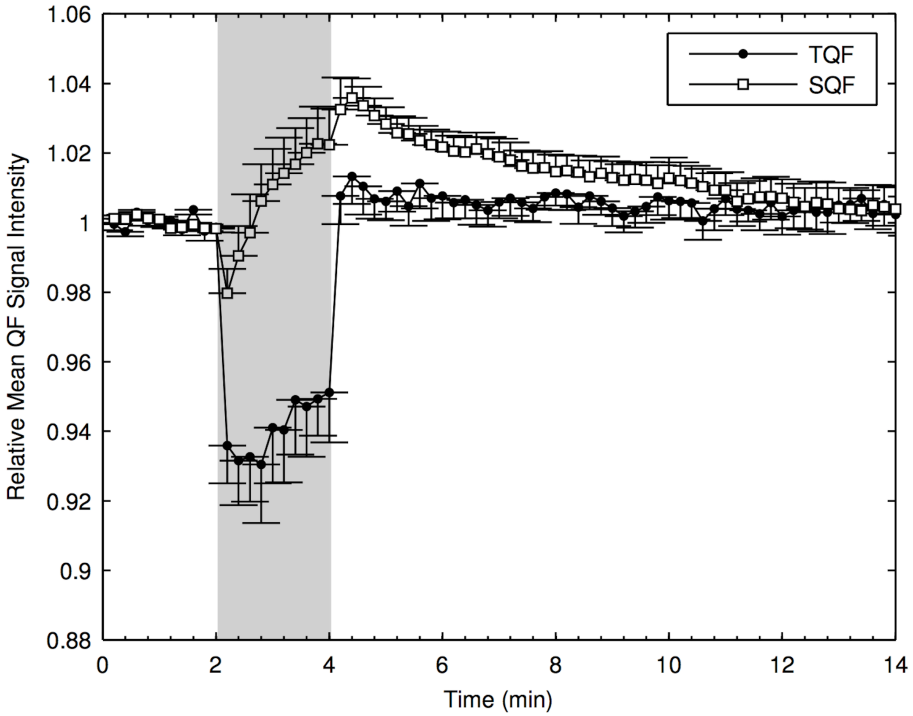

Figure 5.4: Mean±SE obtained from 9 individuals' relative SQF and TQF ^{23}Na signal intensities. The shaded area represents exercise regime at 30% subjects' MVC.

The typical reported values for T_{2f}, and T_{2s} are 1.5-2 ms and 15-30 ms, respectively (7). Hence, the optimal time that would maximize the TQF signal, denoted by the third term in eq. [2], would range from 3.8 to 6.8 ms. The results of optimum τ measurements fall within this range (i.e. 4 ms). To ensure the TQF signal acquired during exercise was maximal, optimal time τ was measured for both rest and exercise regimes. The τ values were varied in random order during TQF signal acquisition. The results confirmed that optimal τ is insensitive to muscle physiological state, i.e. resting or exercising, and exercise intensity.

The SQF ^{23}Na MRS results are in agreement with muscle physiology studies (16, 17,18) in that muscle intracellular sodium increases as a result of exercise. During the first few seconds of exercise, a small but insignificant (p=0.010) signal drop was

observed. For the remainder of the exercise, it is understood that action potentials (AP) cause the passive influx of Na^+ leading to muscle contraction. At the same time, Na^+/K^+-ATPase actively pumps Na^+ out of the cell to re-establish the sodium concentration gradient across the membrane and maintain its excitability. The net flow of Na^+ across the cell membrane depends on the intensity and the duration of exercise. Under long intensive exercise regimes, Na^+/K^+-ATPase is not able to sustain the Na^+ transmembrane gradient leading myocytes to lose their excitability and contractility which ultimately results in muscle fatigue (19). The steady increase in SQF ^{23}Na signal intensity during exercise shows there was sufficient exercise intensity and duration to result in a net influx of Na^+. Additionally, the recovery of SQF ^{23}Na signal to baseline following exercise indicates a net efflux of Na^+, driven by Na^+/K^+-ATPase, and subsequently the transmembrane concentration gradient is restored. None of the subjects reported fatigue. However there was still a statistically significant increase in SQF ^{23}Na signal intensity. If the exercise is more intense and longer in duration, the increase in SQF ^{23}Na signal intensity will likely be greater. Future studies are needed to investigate correlation between the exercise intensity and duration, and the changes in SQF ^{23}Na signal intensity.

The increase in SQF ^{23}Na intensity is in contrast with previous studies (5, 20) that reported no significant change in SQF ^{23}Na signal following exercise in healthy people. An explanation may be that both of those studies were done at lower magnetic field strengths (1.9T and 1.5T, respectively) and thus would have had lower signal to noise ratio (SNR) and reduced sensitivity. A likely more significant reason may be that for both of those studies exercise was performed outside of the magnet bore. In our study, exercise was carried out within the magnet during MR scanning. Based on

our findings, the time delay between exercise termination and start of MRI scanning is significant. Furthermore, we also show highly significant changes during exercise that were not measured in those previous studies.

The effects of exercise on SQF ^{23}Na signal intensity may also be due to increase in ^{23}Na T_2 relaxation time, explained by alteration in intracellular water fractions. Bratton et al. (21) demonstrated a decrease in intracellular bound water fraction during muscle contraction. This leads to an increase in myocyte free water resulting in a more aqueous and isotropic environment that consequently may translate into increased free Na^+ T_2 relaxation times.

We observed a decrease in TQF ^{23}Na signal intensity during exercise. This sounds counterintuitive knowing that TQF ^{23}Na signal represents intracellular ^{23}Na. However, TQF ^{23}Na detects the TQ transitions from the sodium pool interacting with macromolecules. During exercise, a decrease intracellular pH may lead to reversible conformational changes in macromolecules, liberation of bound water (22, 23, 24) and, as a consequence, mobilization of bound Na^+ to the free intracellular sodium pool. Subsequently there is a decrease in the sodium pool that potentially would interact with macromolecules resulting in decreased TQF ^{23}Na signal intensity. Macromolecules such as actin and myosin would be part of these conformational changes as they lead to muscle contraction. They would return to their resting state conformation once the exercise is ceased. The fast recovery of the TQF ^{23}Na signal to baseline within a few seconds upon exercise cessation may be attributed to this phenomenon since actin and myosin would return to their conformational resting state reestablishing the loss in bound water and Na^+, and macromolecular interactions during exercise.

Overall our results indicate that exercise affects both SQF and TQF ^{23}Na signal time-courses. The SQF ^{23}Na mean signal intensity at rest was about 4 times larger than that of TQF ^{23}Na. This is in agreement with the expected range of 2.5-4 times reported by Seshan et al. (15). Despite the fact that SQF ^{23}Na signal intensity is bigger than TQF ^{23}Na, SQF ^{23}Na MRS results is less affected by exercise relative to the effects on TQF ^{23}Na MRS. This may be due to the fact that SQF ^{23}Na signal is a volume-weighted sum of both extra- and intracellular compartments and the changes due to exercise are smaller relative to the TSC at baseline (i.e. signal background). However, TQF ^{23}Na MRS is only limited to the TQ transition part of quadrupolar interactions. The TQF ^{23}Na signal background is already smaller than that of SQF ^{23}Na signal. As a result, the magnitude of changes in TQF ^{23}Na signal intensity due to exercise, relative to the baseline signal, is higher making TQF ^{23}Na MRS more sensitive to exercise effects. This reveals the TQF ^{23}Na MRS potential applications to the study of myopathies, exercise physiology, and sports medicine.

There are a few limitations to this study. First, the time-course resolution is limited to the SNR. The time resolution in this study is 12s. Use of temporal resolution less than 12s would bring SNR down and degrade the quality of the curve fitting for TQF ^{23}Na data. However, the authors believe 12s temporal resolution is sufficient for monitoring changes in exercise studies. Second, the RF coil sensitivity is limited to the size of the coil among other factors. This study utilized an RF surface coil of 15-cm diameter to ensure capture of the gastrocnemius and soleus muscles. The use of a smaller RF coil would limit the coil's field of the view (FOV) to only local regions and eliminate the background signal leading to enhancement of the coil sensitivity to local signal changes. Finally, MRS ^{23}Na techniques are unable to attain spatial resolution

provided by ^{23}Na MRI techniques. The use of surface coils may help reduce the FOV to a more localized area, however fails to spatially resolve the signal within the FOV. As a result, the signal measured in this study combines the signal from gastrocnemius and soleus muscles and it is not possible to resolve the contribution of each individual muscle. However, ^{23}Na MRS techniques provide superior temporal resolution relative to ^{23}Na MRI techniques making them suitable to investigate dynamic physiological changes in skeletal muscle. In summary, SQF and TQF ^{23}Na MRS are affected by exercise. Due to their high temporal resolution they can monitor physiological changes during and following exercise. Particularly, the higher TQF ^{23}Na MRS sensitivity to effects of exercise and its fast recovery following exercise makes it a better ^{23}Na MRS tool for studying muscle physiological changes such as exercise and diseases.

5.3.6 References

1. Robinson JD, Flashner MS. The (Na+ + K+)-activated ATPase. Enzymatic and transport properties. Biochimica et biophysica acta. 1979;549:145-176.

2. Maudsley AA, Hilal SK. Biological aspects of sodium-23 imaging. British medical bulletin. 1984;40:165-166.

3. Jaccard G, Wimperis S, Bodenhausen G. Multiple-quantum NMR spectroscopy of S=3/2 spins in isotropic phase: A new probe for multiexponential relaxation. The Journal of Chemical Physics. 1986;85(11):6282-6293.

4. Chang G, Wang L, Schweitzer ME, Regatte RR. 3D 23Na MRI of human skeletal muscle at 7 Tesla: initial experience. European radiology. 2010;20(8):2039-46.

5. Bansal N, Szczepaniak L, Ternullo D, Fleckenstein JL, Malloy CR. Effect of exercise on (23)Na MRI and relaxation characteristics of the human calf muscle. Journal

of magnetic resonance imaging : JMRI. 2000;11(5):532-8.

6. Constantinides CD, Gillen JS, Boada FE, Pomper MG, Bottomley PA. Human skeletal muscle: sodium MR imaging and quantification-potential applications in exercise and disease. Radiology. 2000;216(2):559-68.

7. Madelin G, Lee J, Regatte RR, Jerschow A. Sodium MRI: methods and applications. Progress in nuclear magnetic resonance spectroscopy. 2014;79:14-47.

8. Fulton a B. How crowded is the cytoplasm? Cell. 1982;30(September):345-347.

9. Seshan, V., Sherry, A. D., & Bansal, N. (1997). Evaluation of triple quantum-filtered 23Na NMR spectroscopy in the in situ rat liver. Magnetic Resonance in Medicine, 38(5), 821-827.

10. Tauskela, J. S., Dizon, J. M., Whang, J., & Katz, J. (1997). Evaluation of multiple-quantum-filtered 23Na NMR in monitoring intracellular Na content in the isolated perfused rat heart in the absence of a chemical-shift reagent. Journal of Magnetic Resonance (San Diego, Calif. : 1997), 127(127), 115-127.

11. Reddy, R., Bolinger, L., Shinnar, M., Noyszewski, E., & Leigh, J. S. (1995). Detection of residual quadrupolar interaction in human skeletal muscle and brain in vivo via multiple quantum filtered sodium NMR spectra. Magnetic Resonance in Medicine, 33, 134-139.

12. Kushnir, T., Knubovets, T., Itzchak, Y., Eliav, U., Sadeh, M., Rapoport, L., ? Navon, G. (1997). In vivo 23Na NMR studies of myotonic dystrophy. Magnetic Resonance in Medicine, 37(17), 192-196.

13. Rooney, W. D., & Springer, C. S. (1991). A comprehensive approach to the analysis and interpretation of the resonances of spins 3/2 from living systems. NMR in Biomedicine, 4(March), 209-226.

14. Andrasko, J. (1974). Nonexponential relaxation of 23Na+ in agarose gels. Journal of Magnetic Resonance (1969), 16, 502-504.

15. Seshan, V., & Bansal, N. (1996). In vivo 31P and 23Na NMR spectroscopy and imaging. In M. D. Bruch (Ed.), NMR Spectroscopy Techniques (2nd ed., pp. 557-607). New York: Marcel Dekker, Inc.

16. Sjgaard, G., Adams, R. P., & Saltin, B. (1985). Water and ion shifts in skeletal muscle of humans with intense dynamic knee extension. The American Journal of Physiology, 248(9), R190-R196.

17. Fong, C. N., Atwood, H. L., & Charlton, M. P. (1986). Intracellular sodium-activity at rest and after tetanic stimulation in muscles of normal and dystrophic (dy2J/dy2J) C57BL/6J mice. Experimental Neurology, 93, 359-368.

18. Clausen, T. (2013). Quantification of Na+,K+ pumps and their transport rate in skeletal muscle: functional significance. The Journal of General Physiology, 142, 327-45.

19. McKenna, M. J., Bangsbo, J., & Renaud, J. (2008). Muscle K+, Na+, and Cl disturbances and Na+-K+ pump inactivation: implications for fatigue. Journal of Applied Physiology (Bethesda, Md. : 1985), 104, 288-295.

20 Weber, M.-A., Nielles-Vallespin, S., Huttner, H. B., Whrle, J. C., Jurkat-Rott, K., Lehmann-Horn, F., ... Meinck, H.-M. (2006). Evaluation of patients with paramyotonia at 23Na MR imaging during cold-induced weakness. Radiology, 240(2), 489-500.

21. BRATTON, C. B., HOPKINS, A. L., & WEINBERG, J. W. (1965). NUCLEAR MAGNETIC RESONANCE STUDIES OF LIVING MUSCLE. Science (New York, N.Y.), 147(3659), 738-9.

22. Fung, B. M., & Puon, P. S. (1981). Nuclear magnetic resonance transverse relaxation in muscle water. Biophysical Journal, 33(1), 27-37.

23. Ploutz-Snyder, L. L., Nyren, S., Cooper, T. G., Potchen, E. J., & Meyer, R. A. (1997). Different effects of exercise and edema on T2 relaxation in skeletal muscle. Magnetic Resonance in Medicine : Official Journal of the Society of Magnetic Resonance in Medicine / Society of Magnetic Resonance in Medicine, 37, 676-682.

24. Schmid, A. I., Schewzow, K., Fiedler, G. B., Goluch, S., Laistler, E., Wolzt, M., ... Meyerspeer, M. (2014). Exercising calf muscle T2 * changes correlate with pH, PCr recovery and maximum oxidative phosphorylation. NMR in Biomedicine, 27(November 2013), 553-560.

Chapter 6

Effects of Electrical Muscle Stimulation on Human Calf Muscle Intracellular and Total Sodium Content: A Feasibility Study

Alireza Akbari M.Eng., and Michael D. Noseworthy Ph.D., P.Eng.

6.1 Introduction

In the previous the chapter, the effects of voluntary exercise on single and triple quantum filtered (SQF, TQF) ^{23}Na MRS signal was demonstrated. SQF and TQF ^{23}Na MRS were shown to be sensitive to skeletal muscle functional dynamic activity. Because the trans-membrane sodium gradient consumes up to 50% of cellular energy (Rolfe and Brown (1997)), measurement of ^{23}Na can be used as an indicator

of muscle energetics. Assessing skeletal muscle function using voluntary contraction is easy to do inside the MRI environment and hence is the preferred approach to studying muscle function. Further, this approach is not complicated by the need for specialized MRI compatible devices. However, voluntary exercise excludes subjects with impaired or somehow diseased skeletal muscle function. For example paralysis (e.g. from spinal cord injury) precludes any ability for voluntary contraction study. Also, spastic paralysis or other coarse motor functional problem would result in inconsistent voluntary function making MRI results difficult to comprehend. One way to circumvent this problem is to induce muscle contractions using electrical muscle stimulation (EMS). In chapter 4, an MRI compatible EMS solution was introduced. This chapter details the effects of EMS on SQF and TQF ^{23}Na in calf muscle, and comparisons between stimulated and voluntary muscle contraction are shown. The results presented in this chapter are preliminary and simply intended to provide a feasible platform for future applications and studies.

6.2 Materials and Methods

All data acquisitions were performed using a GE Discovery MR750 3T (General Electric Healthcare, Milwaukee WI) with a custom-made 15cm diameter transmit/receive sodium radiofrequency (RF) surface coil. An in-house designed and built MRI compatible EMS was used to induce dynamic ankle plantar flexion inside the MRI bore, concurrent with MR scans. All data analysis were performed using MATLAB (Mathworks Natick, MA, USA (version R2014A)).

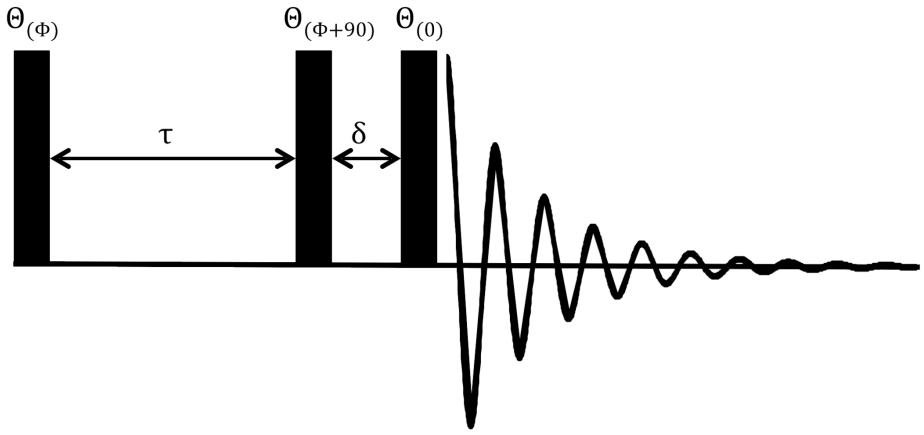

Figure 6.1: TQF ^{23}Na pulse sequence diagram consisting of three $\theta = 90°$ excitation pulses with six-step phase cycling $\phi = 30°, 90°, 150°, 210°, 270°, 330°$. The creation time τ is optimized to give maximum signal while the evolution time δ is kept as short as possible (156μs). Diagram is not to scale.

Sequence Parameters

For a point-to-point comparison between SQF and TQF data across time, the same acquisition parameters were used for both SQF and TQF sequences (i.e. TR = 166.7ms, number of complex points = 1024, and spectral bandwidth = 15.625kHz, hard pulse width = 500μs, flip angle = 90°). SQF ^{23}Na spectra were collected using a standard pulse-acquired vendor-provided sequence (FIDCSI). The number of signal averages was set to 6 while the radiofrequency (RF) pulse phase was alternated between 0° and 180°, between each acquisition. TQF ^{23}Na spectra were collected using a three-pulse TQF sequence with six-phase cycling steps (Jaccard *et al.* (1986)): $\theta(\phi) - \tau - \theta(\phi + 90) - \delta - \theta(0) -$ Acquisition (fig. 6.1), where $\theta = 90°, \phi = 30°, 90°, 150°, 210°, 270°, 330°$, and τ and δ being the creation and evolution times, respectively.

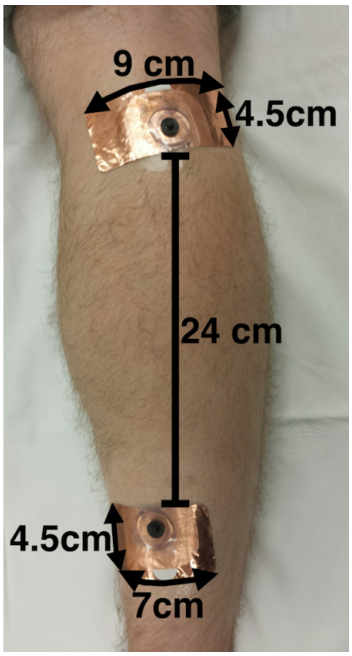

Figure 6.2: The EMS electrode cites on the calf muscle.

EMS Setup

A 30-year old healthy subject's maximum voluntary contraction (MVC) load for ankle dynamic plantar flexion was determined a few days prior to the scan. The location of the motor points were also predetermined using the stimulus threshold contour mapping technique (Botter *et al.* (2011), Gobbo *et al.* (2014)). Copper strips were placed about 24 cm away from each other on motor points of the superior and inferior heads of the medial gastrocnemius muscle (fig.6.2). The RF-translucent gel electrodes were placed on top of the copper tape and the subject's foot was fixed in the ergometer. The EMS frequency was set at 40Hz and both the current intensity and muscle load were increased until comfortable dynamic flexion was accomplished producing a 4cm displacement with each contraction. Then the stimulus intensity was increased to

125% and maintained at that level for the stimulation paradigm. The EMS parameters determined for the subject were pulse-width = 0.1ms, frequency = 40 Hz with a load =12% MVC. The ankle dynamic plantar flexion was performed such that it took 1 second to push against the load and 1 second for the foot to go back to rest position i.e. contraction rate of 0.5Hz.

^{23}Na QF MRS and EMS Protocol Development

In order to use EMS in conjunction with SQF and TQF ^{23}Na MRS, it needs to be tested for any noise introduced in the QF signal from the EMS electrode presence and activity; especially TQF that is much smaller than SQF signal. For this reason, the following four test cases are considered for each SQF and TQF acquisitions in the:

1. absence of any electrodes
2. presence of only electrodes
3. presence of electrodes attached to the EMS unit while the unit being off
4. presence of electrodes attached to the EMS unit while the unit being on

The subject was positioned supine in the magnet bore with one leg placed in the ergometer pedal and RF surface coil horizontally positioned under the calf muscle belly. The leg and coil were immobilized using a strap tied to the either side of the MR bed. SQF and TQF scans were performed under each test conditions mentioned above. Each scan took one minute to complete.

In vivo Demonstration of ^{23}Na QF MRS and EMS

To demonstrate the effects of EMS on SQF and TQF ^{23}Na signal before, and after exercise, both SQF and TQF ^{23}Na MRS protocols were designed to cover a two-minute baseline, two-minute exercise, and 10-minute recovery regimes. Based on the results of the above protocol development discussed in the next section, the EMS unit was detached from the electrodes during baseline and post-EMS regimes.

In vivo ^{23}Na QF MRS Data Analysis

The 12-second averaged ^{23}Na QF free induction decays (FIDs) were first fitted to a time signal model and Fourier transformed. The signal intensity was then determined from the area of the absorptive lineshapes (i.e. the real part of the Fourier transformed spectra). The SQF FIDs were fitted to the following biexponential decay function (Rooney and Springer (1991), Andrasko (1974)):

$$M_{xy} = Ae^{-t/T_{2s}^*} + Be^{-t/T_{2f}^*} \textbf{[1]}$$

where A and B are the signal intensity contributions of fast and slow component, and T_{2f}^*, and T_{2s}^* are the fast and slow transverse relaxation times in the presence of magnetic field inhomogeneity, respectively. The TQF ^{23}Na FID was modeled as follows (Seshan and Bansal (1996)):

$$M_{xy} = M_0 K_{TQ}(e^{-\tau/T_{2s}^*} - e^{-\tau/T_{2f}^*})e^{\delta/T_{TQ}} cos(3\omega\delta)(e^{-t/T_{2s}^*} - e^{-t/T_{2f}^*}) \textbf{[2]}$$

where M_0 is the equilibrium longitudinal magnetization, K_{TQ} is a TQ-specific constant equal to 9/40, T_{2f}^*, and T_{2s}^* are the fast and slow transverse relaxation times in

the presence of magnetic filed inhomogeneity, respectively, and T_{TQ} is the T_2^* for the TQ transition. The creation time $\tau = 4ms$ and evolution time $\delta = 156\mu s$ are pulse sequence parameters (fig.6.1). Equation [**2**] could be reduced to:

$$M_{xy} = A(e^{-t/T_{2s}^*} - e^{-t/T_{2f}^*})[\mathbf{3}]$$

where A represents the effective value of all constant terms in equation [**2**]:

$$A = M_0 K_{TQ}(e^{-\tau/T_{2s}^*} - e^{-\tau)/T_{2f}^*})e^{\delta/T_{TQ}} cos(3\omega\delta)[\mathbf{4}]$$

The TQF ^{23}Na FIDs were fitted to [**3**].

6.3 Results and Discussion

Figure 6.3 shows the effects of EMS on the SQF and TQF free induction decays (FIDs) in comparison to the case where there is no electrode present during acquisition. As demonstrated both SQF and TQF FIDs are contaminated by the EMS. However, the SQF FID is affected to a smaller degree, relative to TQF, since it is about 20 times larger in peak magnitude than TQF. Hence, careful attention must be paid to the TQF signal as it is more susceptible to EMS interference. It is evident from figure 6.3b, that TQF is greatly degraded by EMS regardless whether it is on or off. However, when the EMS was disconnected from the electrodes, the noise induced in the TQF FID was minimal (fig. 6.3d). Therefore, in such a case data collection during EMS of the muscle would be of no practical use. For this reason, the only way to assess muscle in the presence of EMS would be to compare post-EMS SQF/TQF

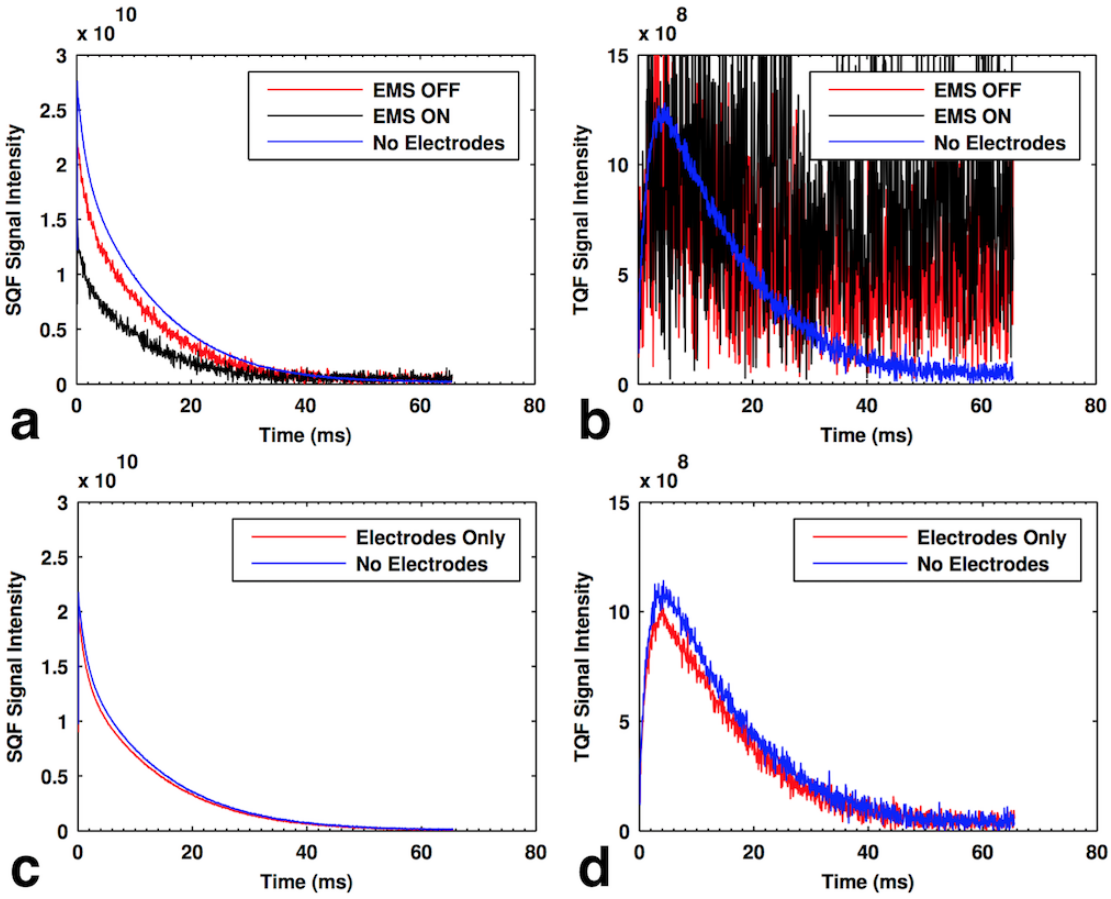

Figure 6.3: EMS effects on SQF and TQF ^{23}Na free induction decays (FIDs). a) SQF, and b) TQF FIDs when the EMS unit was connected and was OFF and ON, compared to when electrodes were absent. c) SQF, and d) TQF FIDs when only the electrodes were present compared to EMS electrodes being absent

signal time-courses to baseline values collected prior to EMS delivery. In order to keep comparison between pre- and post-EMS and between SQF and TQF acquisition consistent, the electrodes should be attached during subject set up and kept there throughout the scan. The EMS unit would then be connected to electrodes only during stimulus delivery to avoid degradation of the QF signal.

Figure 6.4 demonstrates the ^{23}Na SQF and TQF signal time-course before and following EMS as compared to the voluntary exercise results from chapter 5. Similar

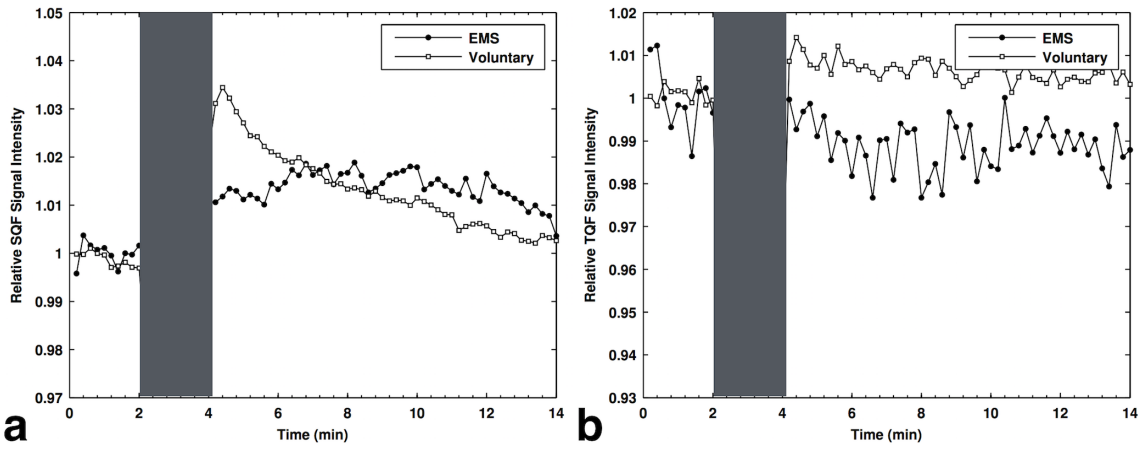

Figure 6.4: a) SQF and b) TQF ^{23}Na signal time-course before and following EMS in comparison to voluntary exercise effort. The shaded areas represent muscle activation regimes.

to voluntary exercise results, the SQF signal appeared to increase and return to baseline, although at a reduced rate, while the TQF seems to return to baseline immediately after EMS cessation. Explaining the behaviour of SQF and TQF signals following EMS and whether it is statistically significant is subject to further studies. The results as presented may be due to the mode of muscle contraction, i.e. EMS as opposed to voluntary contraction, and/or subject variability. The goal of this study was to demonstrate the feasibility of utilizing EMS in the study of muscle dynamics through SQF and TQF ^{23}Na MRS.

6.4 Conclusion

This work shows how EMS can be utilized in the assessment of skeletal muscle dynamics in combination with SQF and TQF ^{23}Na MRS. Although QF ^{23}Na data acquisition during EMS showed to be useless due to induction of profound noise in the MRI signal, post-EMS data is still able to provide potentially valuable information of skeletal

muscle dynamics. The use of EMS is advantageous due to a couple of reasons: 1) it provides a means for inducing controlled muscle contraction, and 2) it can help assess skeletal muscle in subjects/patients who have predefined conditions of impaired muscle motor function.

Chapter 7

Effects of Acquisition Window Duration on *In Vivo* Sodium Magnetic Resonance Image Quality of the Human Articular Cartilage

Alireza Akbari M.Eng., and Michael D. Noseworthy Ph.D., P.Eng.

7.1 Context of the Paper

^{23}Na MRI of the articular cartilage has been performed using various k-space acquisition techniques and T_{aq}s (acquisition window lengths). However, no investigation of T_{aq} effects on ^{23}Na image quality has been done. Therefore, in this chapter evaluation of this relationship was performed on human articular cartilage, *in vivo*, as resolution and SNR are critical for any possible diagnostic utility of the technique.

7.2 Declaration Statement

This manuscript has been prepared in final format for submission to *Magnetic Resonance in Medicine*. Alireza Akbari provided the concept for this study and implemented the density-adapted 3-dimensional projection reconstruction (DA 3D-PR) pulse sequence and, as principle author, wrote the first draft of the article, collected the data and performed analysis and created figures as appropriate. Michael D. Noseworthy provided the guidance, funding and advice, and performed substantial editing of the manuscript.

7.3 Paper

Effects of Acquisition Window Duration on In Vivo Sodium Magnetic Resonance Image Quality of the Human Articular Cartilage

Alireza Akbari MEng[1,2], and Michael D. Noseworthy PhD PEng[1,2,3]

[1]*School of Biomedical Engineering, McMaster University, Hamilton, Ontario, Canada;*
[2]*Imaging Research Centre, St. Joseph's Healthcare, Hamilton, Ontario, Canada;*
[3]*Electrical and Computer Engineering, McMaster University, Hamilton, Ontario, Canada;*

Address for correspondence:

Dr. Michael D. Noseworthy, PhD PEng

Electrical and Computer Engineering

Engineering Technology Building, Room 406

McMaster University

1280 Main Street West., Hamilton, Ontario, Canada. L8S 4K1

VOICE: (905) 525-9140 x23727

EMAIL: nosewor@mcmaster.ca

Running Title: Sodium MRI and acquisition window length

Keywords: Sodium, Magnetic Resonance Imaging, Cartilage

7.3.1 Abstract

Purpose: Sodium magnetic resonance imaging (MRI) is signal-to-noise (SNR) limited. According to sampling theory, the SNR improves by the square root of the acquisition window (T_{aq}) length when T_{aq} is increased. However, long T_{aq} leads to image blurring. The goal of this study was to study the T_{aq} length effects on *in vivo* sodium MRI of the articular cartilage image quality.

Methodology: Knee sodium images from 3 healthy volunteers were acquired using a density adapted 3-dimensional projection reconstruction (DA-3DPR) at 3Tesla. The acquisitions were performed with T_{aq} = 4, 8, 12, 16, 20, and 25 ms. The DA-3DPR point spread function (PSF) peak broadening and amplitude loss was calculated analytically under the influence of a monoexponential T2 decay. The SNR was evaluated in patellar, posterior femoral condyle, and femorotibial cartilage. The full-width-at-half-maximum (FWHM) of the slice profile across the aforementioned articular cartilage sections was calculated as a measure of the image blurring.

Results: SNR doubled in all three sections of articular cartilage, when T_{aq} was increased from 4 to 25 ms. This SNR gain was achieved at the cost of a slight blurring ($1 \pm 0mm$, mean±SE) in the cartilage.

Conclusion: The results indicate that the SNR benefit from increasing T_{aq} duration outweighs the adverse effect of image blurring.

7.3.2 Introduction

It has been shown that sodium concentration is highly correlated with glycosaminoglycan (GAG) content, a marker of osteoarthritis (OA), in the articular cartilage (1,2,3,4). For instance, patellar cartilage in vivo sodium concentration in healthy

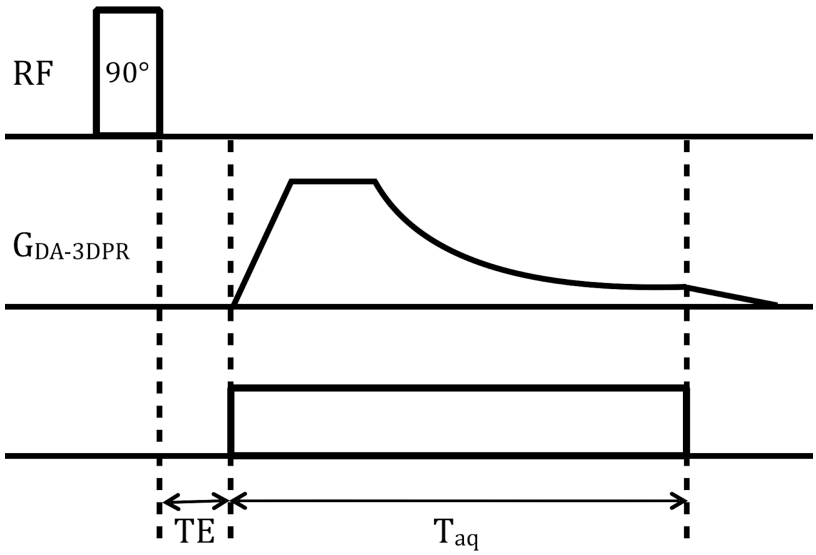

Figure 7.1: Schematic view of a density adapted 3-dimensional projection reconstruction (DA-3DPR) pulse sequence. The readout gradient, echo time, and acquisition window are indicated by $G_{DA\text{-}3DPR}$, TE, and T_{aq}.

individuals ranges between 250 to 350 mM while a lower amount is observed in subjects with early-stage OA (4). Hence, sodium MRI could play an important role in non-invasive assessment of cartilage health in early detection of OA.

Even though ^{23}Na is 100% naturally abundant, a combination of low in vivo concentration and a gyromagnetic ratio about 25% that of proton results in a reduced nuclear magnetic resonance (NMR) sensitivity such that the signal is about 22,000 times weaker than that of water (5). Another challenging issue for sodium MRI is the very short biexponential transverse relaxation. Sodium fast and slow transverse relaxation components range from 0.5 to 2.5, and 10 to 30ms, respectively, in the articular cartilage (6). These challenges make sodium MRI a difficult technique requiring long acquisition times and lower resolution to achieve adequate signal-to-noise ratio (SNR). Therefore, any techniques that help enhance either acquisition time, resolution or SNR without sacrificing the others are highly desirable. To minimize signal

losses due to short relaxation times, three-dimensional (3D) center-out k-space acquisition schemes are used that sample the spatially-encoded free-induction decay (FID) at very short echo times (TE) by eliminating the phase-encode step. For this reason, pulse sequences like 3D projection reconstruction (3DPR) (7), twisted projection imaging (TPI) (8), and 3D cones (9) are best suited for sodium MRI. Besides the use of a short TE acquisition, finding the optimal acquisition window length is critical for improving SNR. It has been shown that SNR per voxel is proportional to the square root of the acquisition window duration (T_{aq}) (10). It would seem a straight forward approach to increase SNR simply through increasing T_{aq}. However, lengthening T_{aq} results in image blurring, due to broadening of the signal point spread function (PSF), and signal amplitude loss due to PSF peak height reduction (especially true for situations with short T_2^*). Rahmer et al. (11) showed that an optimized acquisition window duration could be found that maximizes SNR with small blurring effects for short-T_2 signal decay using an ultra-short echo time (UTE) 3DPR sampling scheme. The advantage of finding an optimized length of T_{aq} is important in that it could lead to SNR improvement without affecting acquisition time or image resolution.

Sodium MRI of the articular cartilage has been demonstrated using different k-space sampling schemes at various magnetic fields (2,5,9,12). However, a study that demonstrates the effects of acquisition window on image quality is lacking. The goal of this work was to demonstrate how acquisition window duration would improve the sodium SNR in articular cartilage and whether this improvement outweighs the adverse effect of T_2^* on image quality as a result of lengthening T_{aq}. A density-adapted three-dimensional radial projection reconstruction (DA-3DPR) (13) k-space sampling scheme depicted in Fig. 7.1 was chosen because, like TPI, it provides a high SNR

efficiency, and like 3DPR, it is easy to implement and conveniently allows for adjusting T_{aq} length for various durations while keeping the same number of projections and resolution.

7.3.3 Methods

In a study approved by our institutional research ethics board a DA-3DPR scheme was implemented on a GE MR750 3T (General Electric Healthcare, Milwaukee WI) by modifying a standard FID-CSI pulse sequence. Sodium images were acquired using an in-house-built 12-rung, 18-cm inner diameter sodium quadrature birdcage coil. To evaluate the effect of acquisition window duration, 6 sets of DA-3DPR with 500, 1000, 1500, 2000, 2500, and 3125 points per projection corresponding to T_{aq} = 4, 8, 12, 16, 20 and 25 ms, respectively, were generated. The PSF of each set under the influence of T_2^*=10 ms decay, assuming monoexponential decay, was simulated for comparison with the in vivo results.

In vivo sodium MR knee images from 3 healthy volunteers were acquired with the 6 sets of DA-3DPR. The following parameters were used for all 6 sets: TE (the end of the RF pulse to the beginning of the acquisition window)/TR = 0.25/100 ms, 11310 projections, and isotropic resolution/FOV = 0.3/18cm. For a more accurate characterization of the effects of T_{aq} duration on SNR and blurring, an averaging of two was done for all of scans at the cost of longer acquisition time.

All images were reconstructed into 60 slices with in-plane resolution of 540x540 (0.33x0.33mm^2) using a non-uniform fast Fourier transformation (NUFFT) (14). To quantify the effect of readout window length on blurring, the full-width-at-half-maximum (FWHM) of a profile of sodium signal intensity across patellar, posterior

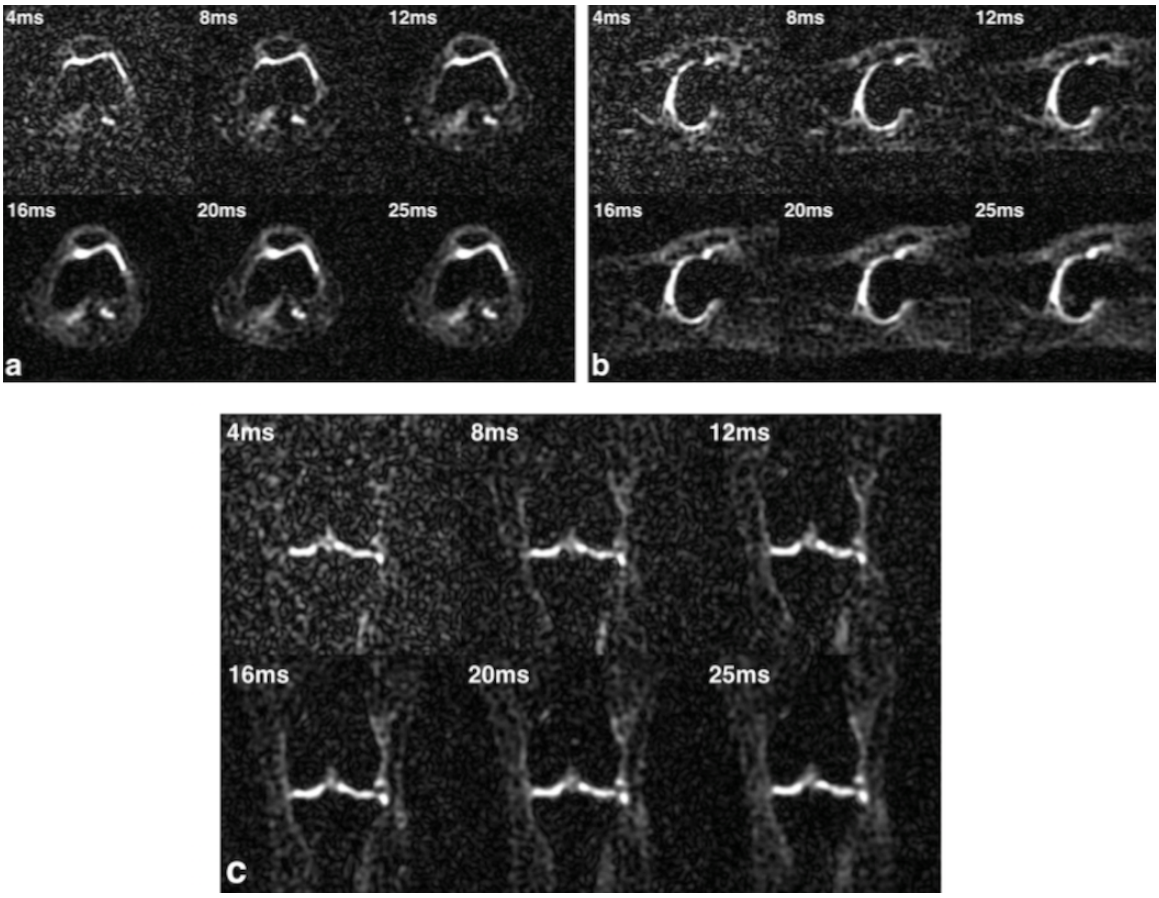

Figure 7.2: In vivo sodium images of articular cartilage obtained with various T_{aq} = 4-25ms in (a) axial, (b) sagittal, (c) coronal views.

femoral condyle, and femorotibial cartilage of the knee was measured. The SNR was calculated in the aforementioned sections of the articular cartilage according to Madelin et al. (12) in the following manner. The standard deviation (SD) of the background noise was calculated in four consecutive sagittal slices where there was no sodium signal present. The mean of the signal in each section of the cartilage were measured from a region of interest across four consecutive slices. All image reconstructions and data analyses where performed in MATLAB (Mathworks Natick, MA, USA, version R2014a).

7.3.4 Results

Because the acquisition was 3D isotropic axial, sagittal, and coronal views through the knee were reconstructed. The various T_{aq} durations are shown in Fig. 7.2a-c. The background noise dramatically decreased as T_{aq} was increased. The distribution of background noise in the region-of-interest (ROI), where there is no sodium MRI signal, obtained for SNR calculations and their corresponding SD are presented in Fig. 7.3a and b, respectively. The noise spectra exhibited classic Rayleigh distribution behaviour with a probability density function (PDF):

$$f_z(z) = \frac{z}{\sigma^2} exp[-\frac{z^2}{2\sigma^2}] \quad [1]$$

where z is the noise pixel intensity from the magnitude image and σ is the SD of the noise in real or imaginary images. The mean and SD of Rayleigh distribution E_z and σ_z , respectively, are then given by:

$$E_z = \sigma\sqrt{\pi/2}, \sigma_z = \sigma\sqrt{2-\pi/2} \quad [2]$$

Noise SD values calculated based on eq. 2 are shown in Fig. 7.3b. The noise SD was reduced by the square root of the T_{aq} duration as depicted by the fitted curve in Fig. 7.3b.

Mean SNR measurements for patellar, posterior femoral condyle, and femorotibial cartilage are shown in Fig. 7.4 for each T_{aq} duration. The SNR increased by at least a factor of 1.3, 1.6, 1.8, 1.9, and 2.0 when T_{aq} was increased from 4 to 8, 12, 16, 20 and 25ms, respectively, for each region of articular cartilage.

Figure 7.5 compares the reduction in mean in vivo sodium signal normalized to

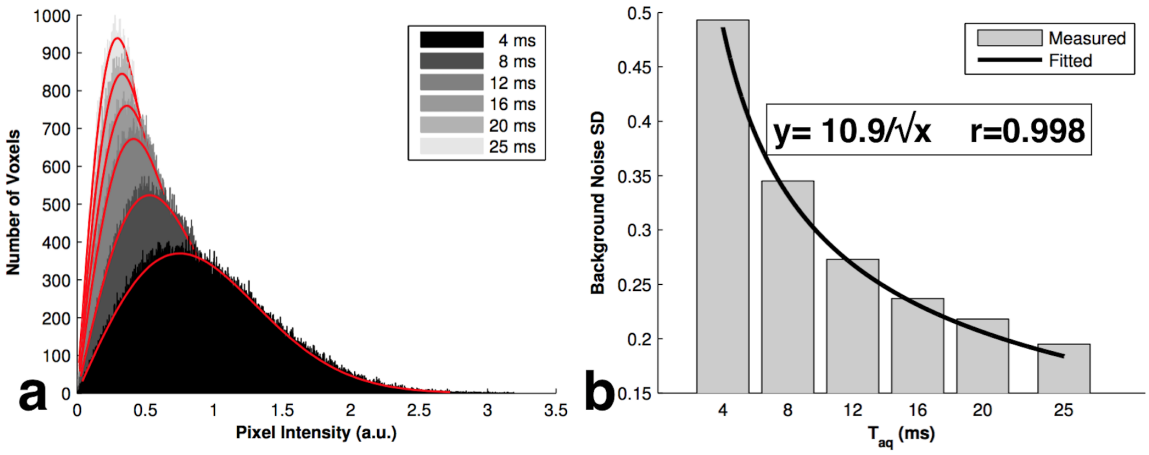

Figure 7.3: Background noise measurements. Voxel intensity distributions measured in an ROI with no MR signal in magnitude images obtained with T_{aq}=4 to 25 ms their best fit with Rayleigh distribution (red curve) (a) and corresponding measured SD (b). The solid line in b) is a fitted curve highlighting the fact that the noise SD is reduced by square root of the T_{aq} duration.

T_{aq}=4ms to the analytical PSF amplitude, when modulated by the T_{aq} length. It was noted that relative sodium signal measured in patellar, posterior femoral condyle, and femorotibial cartilage does not decay as fast as PSF amplitude. The influence of T_{aq} duration on the simulated PSF FWHM based on a monoexponential decay, with T_2^*=10 ms, is demonstrated in Fig. 7.6a. The blurring caused by T_{aq} lengthening in the three sections of the articular cartilage is shown in Fig. 7.6b-c. The FWHM, as a measure of blurring, was slightly broadened for both the PSF, by 2 pixels, and the articular cartilage, by 3±0 (mean±SE) pixels, as T_{aq} was increased from 4 to 25 ms.

7.3.5 Discussion

Sodium MRI is a known low-SNR technique. In order to achieve sufficient SNR, either resolution or acquisition time (or both) need to be sacrificed. Hence, finding ways that improve SNR without resolution and acquisition time penalties would be

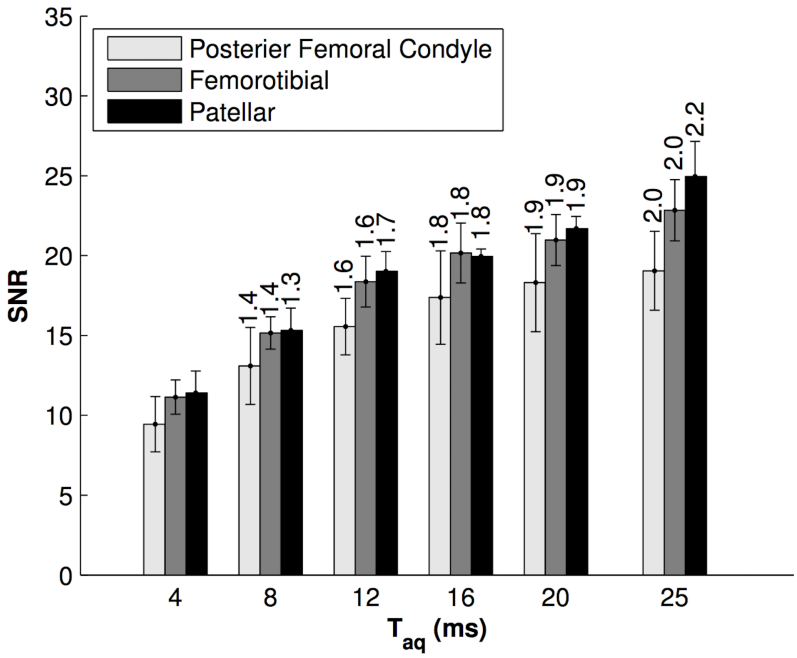

Figure 7.4: In vivo sodium SNR measurements (mean±SE) in the three sections of the articular cartilage. The SNR gain with respect to T_{aq}=4 ms is indicated by the number above each bar.

greatly valued. One way to improve SNR is to find a suitable T_{aq} that maximizes SNR while keeping the adverse effects of short transverse relaxation time on image quality minimized. Importantly, a wide range of sodium fast and slow transverse relaxation times is reported for different tissues (6). Hence, in order to minimize the adverse effects of these relaxation times in terms of signal loss and blurring, proper T_{aq} length, that is tailored to a specific tissue, may be required. This study sought to determine how lengthening T_{aq} would improve SNR in the presence of T_2^* decay in articular cartilage.

Sodium MR images obtained from the articular cartilage in this study demonstrated a considerable improvement in SNR as T_{aq} increased. This effect is similar to that presented by Nagel et al. (13). They showed SNR in sodium images of the brain,

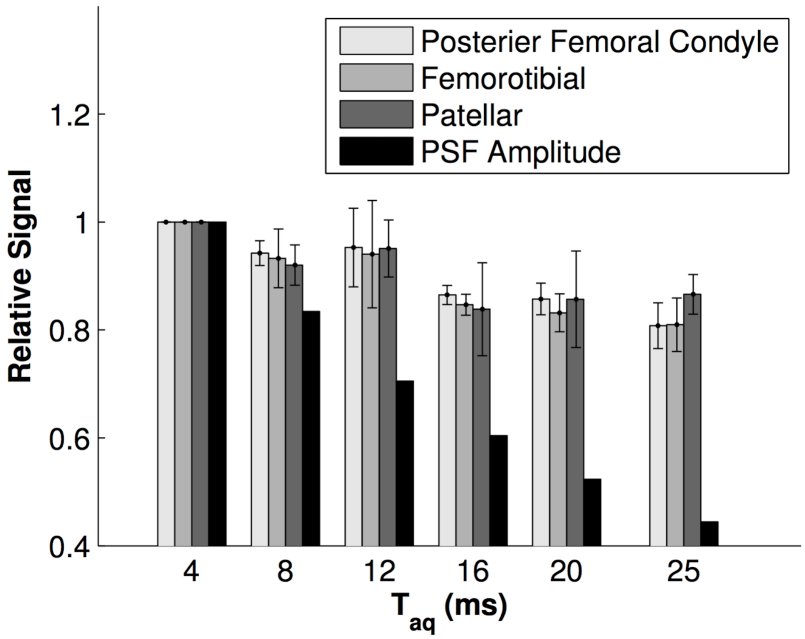

Figure 7.5: Relative in vivo sodium signal (mean±SE) loss observed in the three sections of the articular cartilage compared with the analytical signal loss in the PSF amplitude as the acquisition window is increased from 4 to 25 ms.

acquired using DA-3DPR, increased as the T_{aq} length was extended. Based on their analytical calculation, the optimal acquisition window is when $T_{aq} = 0.39T^*_{2s}$ for a biexponential decay where $(T^*_{2s})/(T^*_{2f}) = 10$. We chose a range of T_{aq} from 4 to 25 ms to find a potential optimal T_{aq} duration. However, optimal T_{aq} , over this range, was not clearly found as SNR kept increasing with only slight loss in resolution. This may be due to the wide range of the biexponential transverse relaxation times in articular cartilage. For instance, Staroswiecki et al. measured the monoexponential T^*_2 from the T^*_2 map of the patellar cartilage at 7T to be from 8.5 to 20 ms (9). Nagel et al. (13) also found it hard to identify an optimal T_{aq} duration in sodium imaging of the brain and also attributed it to wide range of sodium transverse relaxation times. Thus, depending on the tissue, there would be a point at which increased SNR would

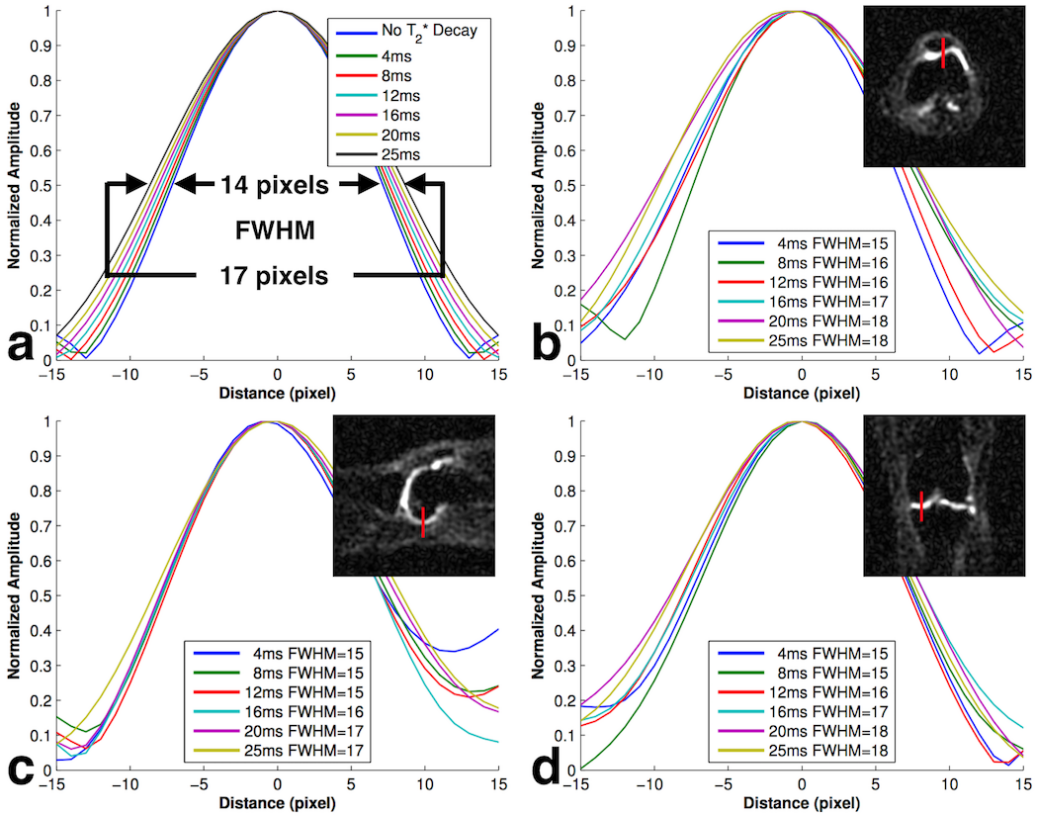

Figure 7.6: Blurring Measurements. Full-width-at-half-maximum (FWHM) measurements of the point-spread function (PSF) under T_2^*=10ms (a) and an example of in vivo FWHM measurements of intensity profile of sodium images along a line through an individual's patellar (b), posterior femoral condyle (c), and femorotibial (d) cartilage for T_{aq}=4-25ms.

lead to deleterious losses in resolution.

The analytical calculation of the PSF for the 3DPR technique does not exhibit severe blurring effects even when T_{aq} is several times greater than T_2^* decay (11). Nagel et al. showed the blurring effects are even smaller, only a few pixels, with DA-3DPR (13) compared to 3DPR especially when T_{aq} is much larger than T_2^* decay. Our results are in agreement with these. The PSF simulation under an assumed monoexponential decay of T_2^*=10ms showed only a 2 pixel broadening in the PSF

FWHM when T_{aq} was increased from 4 to 25 ms (Fig. 7.6a). Therefore, it was of no surprise when blurring in the articular cartilage thickness was also noted to be similar.

The loss in PSF amplitude was more dramatic than blurring, as T_{aq} was lengthened. The analytical amplitude loss of the PSF is based on point source calculations. The signal measurements in the articular cartilage under the influence of T_{aq} lengthening show that even though articular cartilage is thin (comparable to the PSF FWHM) it likely should not be categorized as a small object since the in vivo signal does not decrease as dramatically as PSF amplitude does. This might seem counter intuitive at first since one might think of the articular cartilage as a thin sheet of connective tissue. However, the articular cartilage extends beyond the PSF FWHM in the plane perpendicular to the cartilage thickness and consequently T_2^* does not affect SNR in that direction. Additionally, in the direction along the thickness, where the extent of cartilage is comparable to the PSF FWHM, small blurring prevents significant signal loss due to signal bleed through to adjacent pixels. Therefore, signal loss is not significantly affected by increasing T_{aq} duration. This may be further reason why an optimal acquisition window for knee sodium imaging is not as clear as predicted by a small-object model.

The noise in magnitude images takes the form of a Rayleigh distribution (15,16). In the case of a noisy image, this may lead to an overestimation of the MR signal (17). This becomes an important issue for SNR-limited applications such as sodium MRI. Our results clearly indicate two benefits from increasing the T_{aq} duration. First, the distribution of the noise shifts towards zero as the T_{aq} duration increases (Fig. 7.3a). This leads to a smaller distribution of the noise level across the image. Second, the

noise SD reduces at the same time (Fig. 7.3b) that results in less fluctuation in the MR signal. These two, together, lead to SNR enhancement and a more reliable signal measurement that is especially important for signal quantification purposes.

The results indicate when increasing T_{aq} duration the rate of reduction in the noise SD (Fig. 7.3b) is much higher than tissue signal loss (Fig. 7.5). This suggests that T_{aq} duration could be increased even further than 25 ms and yet achieve additional gain in SNR. One competing factor, however, is the blurring induced as a consequence of lengthening T_{aq} duration. Depending on the required resolution, T_{aq} could still be lengthened for more SNR gain.

7.3.6 Conclusion

This work shows that increasing T_{aq} duration leads to significant SNR improvements in the articular cartilage at the cost of only minor image blurring. If minimal blurring is inconsequential for the diagnostic purpose of the imaging one could take advantage of the SNR gain, important for SNR-limited applications such as sodium MRI.

7.3.7 References

1. Lesperance LM, Gray ML, Burstein D. Determination of fixed charge density in cartilage using nuclear magnetic resonance. J Orthop Res. 1992;10(30):1-13.

2. Reddy R, Insko EK, Noyszewski E a, Dandora R, Kneeland JB, Leigh JS. Sodium MRI of human articular cartilage in vivo. Magn Reson Med. 1998;39(5):697-701.

3. Shapiro EM, Borthakur A, Gougoutas A, Reddy R. 23Na MRI accurately measures fixed charge density in articular cartilage. Magn Reson Med. 2002;47(2):284-291.

4. Wheaton AJ, Borthakur A, Shapiro EM, et al. Proteoglycan loss in human

knee cartilage: quantitation with sodium MR imaging–feasibility study. Radiology. 2004;231(3):900-905.

5. Wang L, Wu Y, Chang G, et al. Rapid isotropic 3D-sodium MRI of the knee joint in vivo at 7T. J Magn Reson Imaging. 2009;30(3):606-614.

6. Madelin G, Lee J, Regatte RR, Jerschow A. Sodium MRI: methods and applications. Prog Nucl Magn Reson Spectrosc. 2014;79:14-47.

7. Nielles-Vallespin S, Weber MA, Bock M, et al. 3D radial projection technique with ultrashort echo times for sodium MRI: Clinical applications in human brain and skeletal muscle. Magn Reson Med. 2007;57:74-81.

8. Boada FE, Gillen JS, Shen GX, Chang SY, Thulborn KR. Fast three dimensional sodium imaging. Magn Reson Med. 1997;37(5):706-715.

9. Staroswiecki E, Bangerter NK, Gurney PT, Grafendorfer T, Gold GE, Hargreaves BA. In vivo sodium imaging of human patellar cartilage with a 3D cones sequence at 3 T and 7 T. J Magn Reson Imaging. 2010;32(2):446-451.

10. Haacke EM, Brown RW, Thompson MR, Venkatesan R. Magnetic Resonance Imaging: Physical Principles and Sequence Design. New York: A John Wiley and Sons; 1999.

11. Rahmer J, Brnert P, Groen J, Bos C. Three-dimensional radial ultrashort echo-time imaging with T2 adapted sampling. Magn Reson Med. 2006;55(5):1075-1082.

12. Madelin G, Babb JS, Xia D, Chang G, Jerschow A, Regatte RR. Reproducibility and repeatability of quantitative sodium magnetic resonance imaging in vivo in articular cartilage at 3 T and 7 T. Magn Reson Med. 2012;68(3):841-849.

13. Nagel AM, Laun FB, Weber MA, Matthies C, Semmler W, Schad LR. Sodium MRI using a density-adapted 3D radial acquisition technique. Magn Reson Med.

2009;62(6):1565-1573.

14. Fessler J a. On NUFFT-based gridding for non-Cartesian MRI. J Magn Reson. 2007;188(2):191-195.

15. Bernstein M a, Thomasson DM, Perman WH. Improved detectability in low signal-to-noise ratio magnetic resonance images by means of a phase-corrected real reconstruction. Med Phys. 1989;16(5):813-817.

16. Gudbjartsson H, Patz S. The Rician distribution of noisy MRI data. Magn Reson Med. 1995;34(6):910-914.

17. Henkelman RM. Measurement of signal intensities in the presence of noise in MR images. Med Phys. 1985;12(2):232-233.

Chapter 8

Random Volumetric *k*-space Trajectories for Sodium (^{23}Na) Magnetic Resonance Imaging

Alireza Akbari M.Eng., Konrad Anand, Christopher Anand Ph.D., and Michael D. Noseworthy Ph.D., P.Eng.

8.1 Introduction

3-dimensional (3D) centre-out k-space sampling schemes such as 3D projection reconstruction (3DPR) (Nielles-Vallespin *et al.* (2007)) and twisted projection imaging (TPI) (Boada *et al.* (1997)) are at the heart of *in vivo* sodium (^{23}Na) magnetic resonance imaging (MRI). These acquisition schemes offer ultra-short echo times making them ideal for imaging short T_2 species such as ^{23}Na. In this chapter a random k-space sampling scheme is introduced. In the previous chapter the use of a density-adapted

3D projection reconstruction (DA-3DPR) (Nagel *et al.* (2009)) in ^{23}Na MRI of the knee was demonstrated. This method is called density adapted because it samples k-space with uniform sampling density. Although this method is very signal-to-noise ratio (SNR) efficient it is not efficient in terms of sampling k-space. This is because each trajectory traverses a straight radial line in k-space, hence, a large number of trajectories are required to fully cover all of k-space to satisfying the Nyquist sampling criterion. However, if each single trajectory could twist and turn then a greater section of k-space would be covered per trajectory leading to a higher duty cycle and less number of trajectories and, hence, more efficient sampling. The TPI sampling scheme is a good example of such a high duty cycle capability. However, Nagel *et al.* (Engel *et al.* (2015)) showed there are ways that schemes with even higher duty cycles could be achieved leading to a fewer required number of trajectories, and hence a shorter scan time. In order to lessen scan time even more, the number of projections can be reduced even further (i.e. under-sampled) at the cost of inducing aliasing artefacts in the image domain. However, aliasing can be minimized if under-sampling is done in a pseudo-stochastic fashion leading to incoherent summation of the resultant aliasing artefacts (Tsai and Nishimura (2000)). This was the basis for the DURGA sequence used in proton MR imaging (Curtis and Anand (2008)). The work discussed in this chapter demonstrates the feasibility of a novel random non-Cartesian k-space sampling scheme for *in vivo* ^{23}Na MRI that reduces scan time while dramatically reducing aliasing artifacts caused by under-sampling.

8.2 Methods

8.2.1 Pseudo-random Trajectory Generation

The trajectories were generated individually. Conventionally, the minimum number of required k-space trajectories is determined by the Nyquist criterion. However, this criterion cannot be used here because the scheme is meant to under-sample k-space. For this reason, the point spread function was used to assess the severity of the aliasing artefacts and determine the required number of trajectories. Each individual trajectory was subject to the maximum allowed gradient amplitude (50 $\mathrm{mT.m^{-1}}$) and slew rate (200 $\mathrm{T.m^{-1}.s^{-1}}$), and a maximum radial k-space extent (k_r=1.67 $\mathrm{cm^{-1}}$) corresponding to a 0.3cm isotropic resolution. The design of the trajectory path planning was subject to the optimization of PSF of each individual trajectory. The optimization process is described in details in Curtis and Anand (2008).

8.2.2 Image Reconstruction

One advantage of conventional Cartesian sampling schemes is that they sample k-space uniformly. This makes image reconstruction trivial because a simple discrete fast Fourier transform, which requires the samples to be equally spaced, can be used to transform from the spatial frequency to spatial domains. However, a non-Cartesian k-space acquisition faces two problems. First, the non-uniform sampling density of k-space leads to signal intensity variation in the image because areas where the sampling density is higher results in a higher spatial frequency energy as compared to low-density areas. For this reason, the sampling density needs to be compensated for by what is referred to as density compensation function (DCF). This is the case for

3-dimensional centre-out k-space acquisition schemes. A DCF can easily be obtained for schemes such as 3D-PR, TPI and their derivatives since these trajectories follow an analytical solution. However, this is not the case for a stochastic (or pseudo-stochastic) sampling acquisition scheme and thus needs to be calculated numerically. For this reason, volumes of Voronoi cells around k-space sampling locations were used for calculation of the DCF (Rasche *et al.* (1999)). The second problem is that, in order to reconstruct the images, a simple discrete fast Fourier transform cannot be applied to non-Cartesian samples. A non-uniform Fourier transform is a direct method to reconstruct the image, $m(\mathbf{r})$, according to the following equation:

$$m(\mathbf{r}) = \sum_j \omega(\mathbf{k}_j) s(\mathbf{k}_j) e^{i2\pi \mathbf{k}_j \mathbf{r}} \quad [1]$$

where, $s(\mathbf{k}_j)$ is the sampled signal at the corresponding k-space location denoted by $\mathbf{k}_j$ with a DCF value of $\omega(\mathbf{k}_j)$. This method is referred to as the conjugate phase reconstruction (Macovski (1985)) and the weighted correlation method (Maeda *et al.* (1988)). However, this method as presented in eq. 1 is computationally slow. Hence, a non-uniform fast Fourier transform (NUFFT) is required. For this purpose, a NUFFT that is based on a min-max interpolation (Fessler and Sutton (2003)) is utilized to speed up the reconstruction process.

All image reconstructions and data analysis were performed in MATLAB (Mathworks Natick, MA, USA (version R2014A)).

8.2.3 Simulation Experiments

MRI k-space acquisition schemes, including Cartesian and non-Cartesian, conventionally follow Nyquist sampling criterion in order to avoid aliasing artifacts. If this criterion is not fulfilled the aliasing artifacts strongly contaminate the MR image. However, this effect can be lessened if k-space is irregularly under-sampled. The degree to which aliasing artefacts are minimized depends on how random the sampling is performed. Furthermore, the resultant final SNR depends on how frequently the centre of k-space is sampled (i.e. as the maximum energy is located at the centre the trajectories are best to sample more frequently that region and hence the design is not totally stochastic). In order to assess the ability of the proposed random acquisition scheme in minimizing aliasing artefacts, it was compared to Cartesian regularly and randomly under-sampled schemes. The comparison set included(**Fig.8.1**):

1. Fully sampled Cartesian k-space
2. Regularly under-sampled Cartesian k-space
3. Randomly under-sampled Cartesian k-space
4. Randomly under-sampled non-Cartesian k-space (i.e. the case proposed by this work).

In order to quantitatively assess the degree of aliasing artefact incoherence, the point spread function (PSF) of all cases were simulated and compared. A simulated phantom was then sampled and digitally reconstructed for all four cases. The fully sampled case contained 3600 trajectories while the remaining under-sampled cases included 400 trajectories, i.e. 9 times under-sampled with respect to the fully sampled case. The trajectory length was kept the same for all cases.

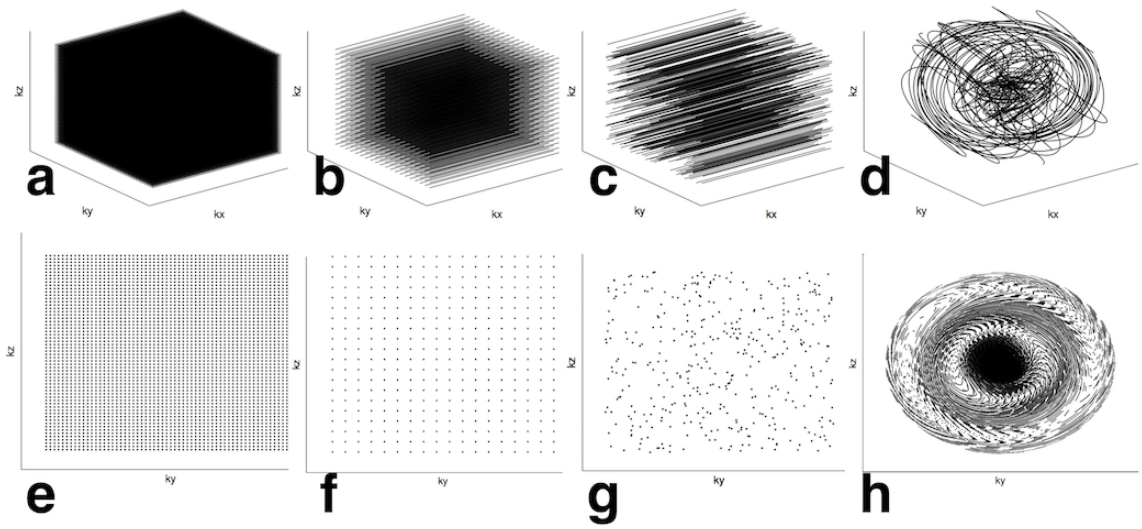

Figure 8.1: K-space acquisition schemes used to investigate how different under-sampling patterns manifest itself as aliasing artifacts in the MR image domain. The 3-dimensional views of a) fully sampled, b) regularly, and c) randomly under-sampled Cartesian, and d) randomly under-sampled non-Cartesian schemes along with their 2-dimensional views through the ky-kz plane (e-h), respectively, are depicted here. For better visualization, only a subset of randomly under-sampled non-Cartesian trajectories is shown in its 3D view. Nonetheless the statistically greater passage near the centre of k-space is evident.

8.2.4 MRI Experiments

The pseudo-stochastic set of trajectories was used to obtain *in vivo* ^{23}Na MR images. The Cartesian sets were not considered for MRI experiments. One reason was that a pulse sequence implementation was needed and, hence, it required significant time for implementation, testing, and debugging. Another reason was that the MR feasibility and performance of the proposed k-space acquisition scheme was in question and the PSF simulation comparisons were deemed to be sufficient to demonstrate the effects of aliasing for each set.

Sodium MRI was performed using a GE MR750 3T (General Electric Healthcare,

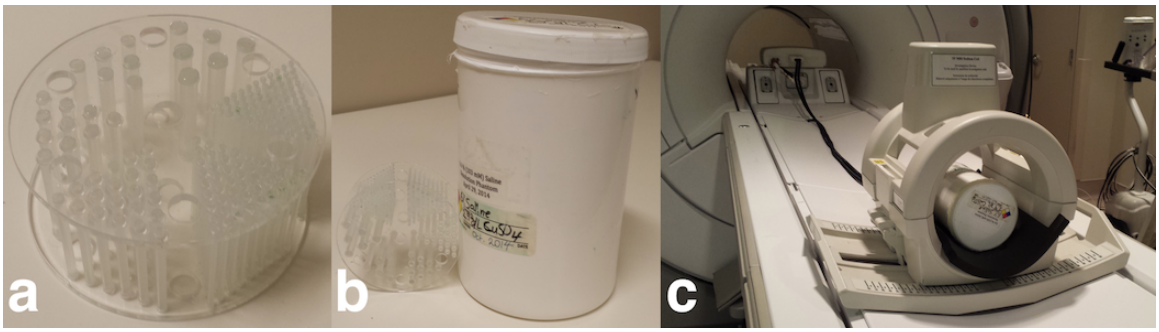

Figure 8.2: Resolution rod-phantom (a) placed in a plastic container filled with 0.6% saline and doped with 2.9 g/L copper sulfate (b) used for resolution performance of the proposed k-space acquisition scheme. The phantom and RF birdcage coil on MR bed (c).

Milwaukee WI) and an in-house-made 12-pole quadrature sodium birdcage coil. The pulse sequence consisted of a single $500\mu s$ hard pulse, TE/TR = 0.46/75 ms, flip angle = 90°, NEX=64, 2000 samples per trajectory, sampling rate of $4\mu s$/sample, leading to a total scan time of 32 minutes. The trajectories were designed for a nominal isotropic resolution of 3 mm. A resolution rod-phantom (Model ECT/DLX/MP, Data Spectrum Corp., Durham, North Carolina) containing plexiglass rods of 1.2, 1.6, 2.4, 3.2, 4.0, and 4.8 mm diameter immersed in a container (height/diameter = 16/10 cm) filled with 0.6% saline and doped with 2.9 g/L copper sulfate was used to measure the actual achievable resolution. An axial T_2-weighted proton image (TE/TR = 1.69/5.42 ms, flip angle = 30°, slice thickness=5mm) of the rod-phantom was used to compare with the same axial slice in sodium MR image of the phantom for resolution assessment (**Fig.8.2**). Sodium images of two healthy knees were then acquired to demonstrate *in vivo* utility. In order to assess image quality *in vivo*, SNR in patellar, femoro-tibial, and posterior condyle cartilage was measured according to Madelin *et al.* (2012b).

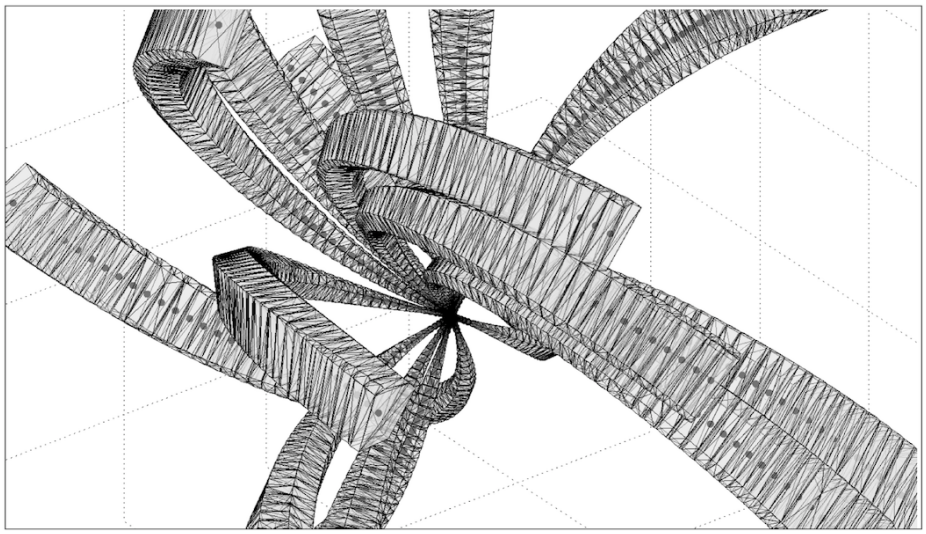

Figure 8.3: Randomly sampled k-space trajectory Voronoi diagram. The density compensation function (DCF) was determined from the volume that each sampled point takes up in k-space. The solid dots in the figure represent the sampled points in k-space and the their surrounding polygons represent their volume. Only 14 representative trajectories (out of a total 400) are shown for visualization purposes.

8.3 Results

Figure 8.3 demonstrates the Voronoi diagram used for calculating the DCF of the randomly sampled non-Cartesian trajectory set. Figure 8.4 shows the PSF measurements of the sampling cases (**Fig.8.4a-h**) and the reconstructed images of a simulated phantom using each one (**Fig.8.4i-l**). Figure 8.5 shows acquired MRI data for assessment of the proposed randomly sampled non-Cartesian acquisition scheme in a resolution phantom. *In vivo* sodium knee MR images acquired from two healthy subjects using the proposed sampling scheme are shown in figure 8.6. The SNR in patellar, femoro-tibial, and posterior condyle cartilage was measured to be 10.6 ± 1.1, 10.5 ± 2.0, 9.6 ± 1.2 (mean $\pm$ SE), respectively.

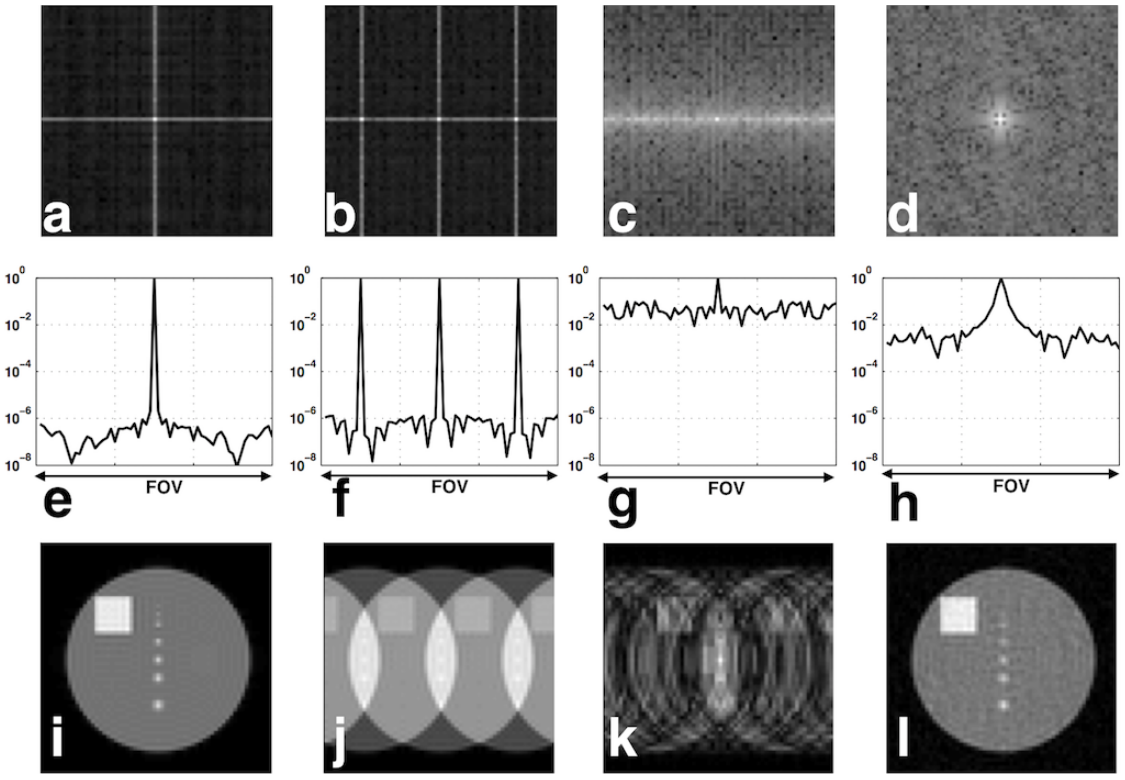

Figure 8.4: A 2D representation through the zy-plane of the point spread function (PSF) measurements of a) fully sampled, b) regularly under-sampled, and c) randomly under-sampled Cartesian, and d) randomly under-sampled non-Cartesian k-space sampling cases, and their 1D PSF representation through the y-direction (e-h), respectively. The reconstructed images sampled from a simulated phantom using the k-space sampling scheme are also shown (i-l).

8.4 Discussion

The work proposed here describes a novel randomly sampled non-Cartesian k-space acquisition and demonstrated its *in vivo* use and how effectively this approach minimizes aliasing artifacts due to under-sampling. The presented acquisition strategy samples k-space non-uniformly and thus needs density compensation to produce images with uniform intensity. This is an inherent requirement of centre-out, non-Cartesian acquisition schemes that, if not addressed, leads to reduced SNR efficiency,

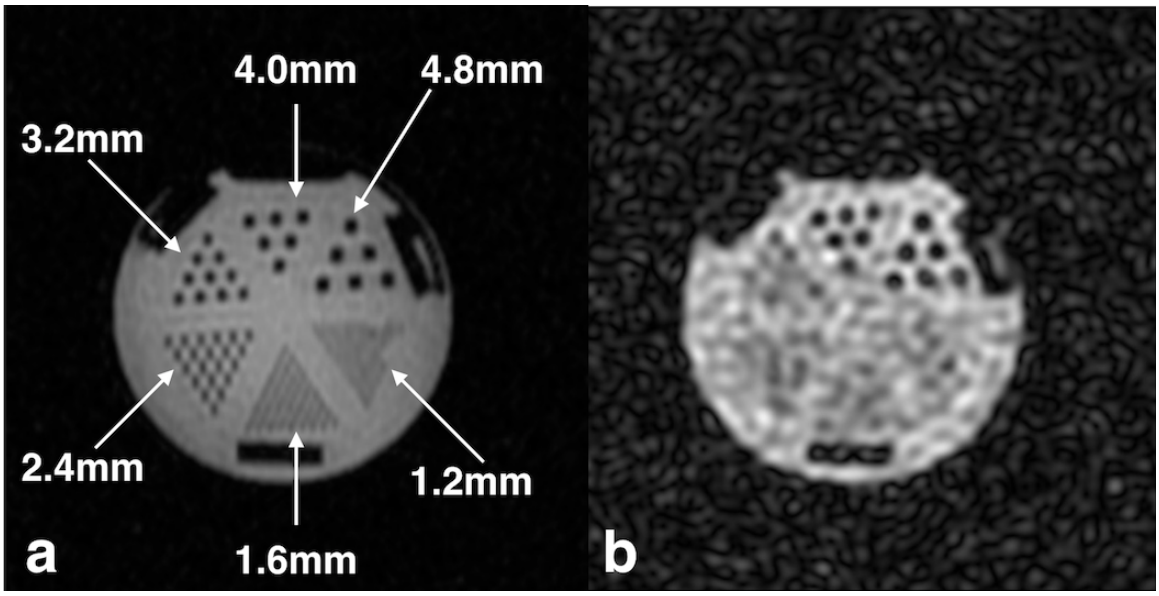

Figure 8.5: Physical testing of a MRI resolution using a plexiglass rod-phantom immersed in 0.6% saline. An axial T_2-weighted proton (a) image of the phantom is presented along with its corresponding axial sodium image (b). The resolution phantom plexiglass rods of 1.2, 1.6, 2.4, 3.2, 4.0, and 4.8 mm in diameter are clearly visible on proton image. The actual resolution achieved by random non-Cartesian k-space acquisition was 4.0 mm.

η. The random non-Cartesian acquisition achieved an SNR efficiency of 78% that is higher than that of 3DPR with $\eta \approx 75\%$ (Nagel *et al.* (2009)). However, η could be significantly improved that is very important for a low-SNR application such as ^{23}Na MRI. Acquisition schemes such as TPI and DA-3DPR were proposed to address this issue. Fortunately, this could also be addressed in the case of the random non-Cartesian acquisition and is the subject of the future work.

Under-sampling of k-space leads to aliasing artifacts in the reconstructed image. The pattern in which under-sampling is done determines how the underlying aliasing artifact would manifest itself in the reconstructed image. A regularly under-sampled

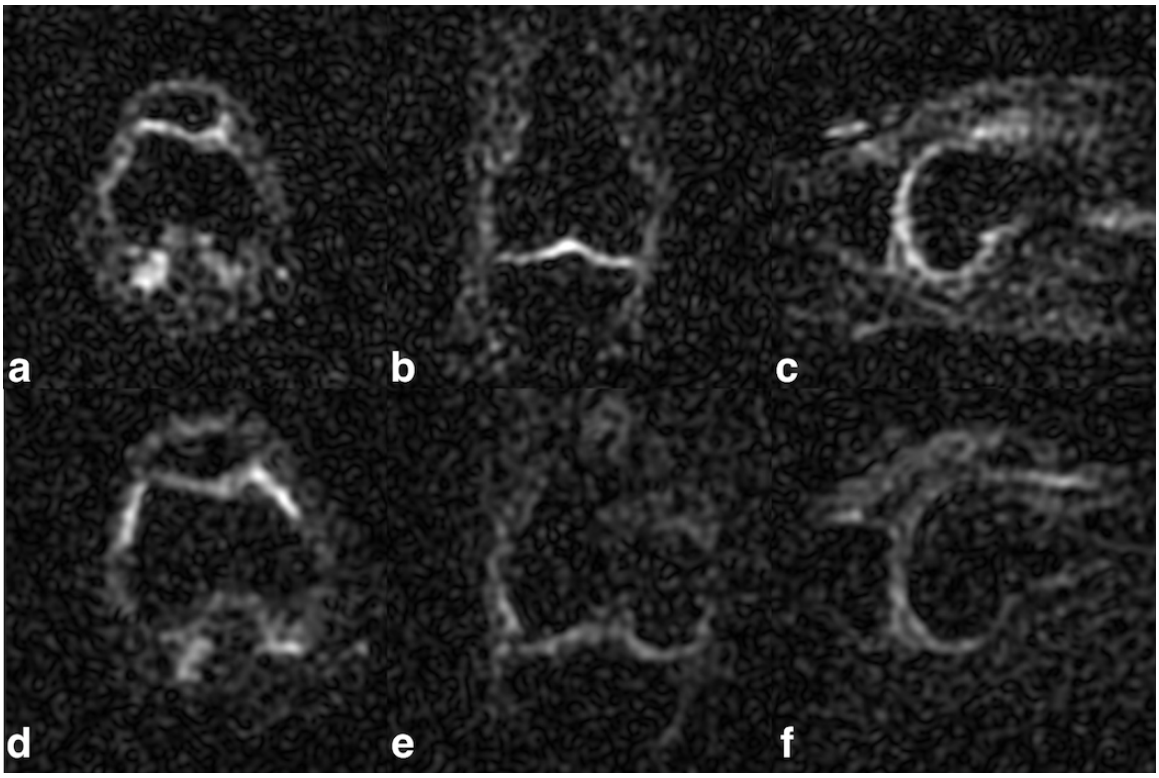

Figure 8.6: *In vivo* axial (a and d), coronal (b and e), and sagittal (c and f) views of ^{23}Na MRI of two healthy subjects.

k-space pattern would lead to a more coherent aliasing artifact while a randomly sampled k-space pattern does otherwise. The k-space sampling scheme PSF could predict the way aliasing artifacts appear in the image and help quantify the level of coherence. The random non-Cartesian sampling scheme has proved to effectively break the aliasing artifact coherence down and turn it into a background benign noise-like pattern. This means scan time reduction by means of under-sampling comes at the cost of reduced SNR. However, the results from a random non-Cartesian PSF simulation indicated that the noise-like aliasing artifact level was below 1% of the maximum PSF peak, while this amount was below 10% in the case of random Cartesian sampling.

The superiority of the random non-Cartesian k-space acquisition over its Cartesian counterpart in minimizing aliasing artifact coherence demonstrates that it may be a desired candidate for ^{23}Na MRI. To date this scheme has not been attempted with proton MRI.

The results from the resolution phantom revealed that the actual resolution achieved by the random non-Cartesian acquisition was 4mm while the trajectories were designed for a nominal isotropic resolution of 3mm. The inconsistency may be due to a few reasons. One possible source of resolution loss could be that ^{23}Na has short biexponential transverse relaxation T_2^* during the readout leading to signal loss and blurring in the image (Rahmer *et al.* (2006)). Another possible source of inconsistency may be the gradient delays that may vary for different gradient trajectories. However this is likely a minor culprit as these delays would only be on the order of a few microseconds.

The *in vivo* images obtained by the proposed novel acquisition method demonstrate ^{23}Na MRI feasibility using this method. The SNR achieved in the articular cartilage was approximately 10. It is hard to compare the SNR with other acquisition methods because of differences in pulse sequence parameters and hardware. The *in vivo* results from DA-3DPR, described in the previous chapter, showed an SNR of about 15 in articular cartilage. One possible explanation for this is that the SNR efficiency of DA-3DPR is about 99% whereas the proposed acquisition scheme possesses an $\eta = 78\%$. Another reason may be because of the longer TR=100ms used for DA-3DPR that allows more time for longitudinal magnetization recovery. The Madelin *et al.* (2012b) knee study, performed using a 3T MRI, also reported higher SNR measurements. This may be due to a shorter echo time (TE=0.15ms from the

end of RF pulse to the beginning of the acquisition window) used during acquisition and/or bigger voxel size (4mm isotropic resolution) used to perform NUFFT for image reconstruction. Staroswiecki *et al.* (2010) reported an SNR of 11.3 measured at 3Tesla in patellar cartilage. This value was achieved while the voxel size used was smaller 1.3x1.3x4.0 mm^3. One possible explanation for the higher SNR in that study may be due to their use of a 10cm diameter transmit/receive surface coil. Surface coils are well known to result in higher SNR, relative to volume coils (e.g. birdcage), through Faraday's Law of Induction. Furthermore, they used a 3D cones pulse sequence that is a derivative of a TPI sequence with high SNR efficiency. Nonetheless, considering parameters used here, the preliminary *in vivo* results obtained through random non-Cartesian acquisition looks promising in ^{23}Na MRI.

The proposed acquisition method may still need increased number of averaging to achieve an acceptable SNR. However, the advantage of this method is that it could cover k-space with less number of trajectories and hence acquire k-space samples in shorter time. This may be instrumental in fast imaging applications such as cardiac or abdominal imaging where k-space needs to be sampled as fast as possible and at the same time, to improve SNR, the acquisition can be repeated as many times as required.

8.5 Conclusion

A stochastic non-Cartesian 3D sampling scheme remarkably reduced the aliasing artefacts caused by under-sampling. The *in vivo* results confirm the feasibility of this scheme for ^{23}Na MRI. This scheme effectively minimizes aliasing artifacts caused by under-sampling and reduces the total scan time through a high sampling-duty cycle

with fewer trajectories. The proposed k-space acquisition possesses an SNR efficiency of 78%. This SNR efficiency could by enhanced by about 22% if it is generated with highly uniform sampling density.

Chapter 9

Conclusions and Future Directions

^{23}Na MRI has gained increased attention due to advancements in MR hardware, acquisition, and reconstruction methods (Madelin *et al.* (2014)). However, it is still considered 'preclinical' because of the great number of challenges remaining. Fortunately, this means there is still a great deal of work to be done. Despite the huge potential application in medicine ^{23}Na MRS is unfortunately almost a forgotten tool since it has a very simple looking one-peak spectrum that does not seem to be very interesting, compared to ^{1}H and ^{31}P spectra. However, as demonstrated in previous chapters, ^{23}Na MRS is a powerful tool in probing muscle function. This could be of incredible utility in studying pathologies like muscle channelopathies that other MR molecular species can not probe directly. This chapter reiterates the contributions made in the previous chapters and finishes with a list of things that need to be addressed in future work.

9.1 Contributions

- EMS provides a controlled and reproducible means of inducing muscle contraction. This work demonstrated an MRI-compatible EMS that could allow the study of acute effects of muscle contraction right in the bore of MRI. It also demonstrated the use of such a device in conjunction with SQF and TQF ^{23}Na MRS of the calf muscle. This may be instrumental in assessing skeletal muscle conditions in subjects with impaired muscle motor function.

- ^{23}Na plays an important role in skeletal muscle contraction. For the first time, this work demonstrated how SQF and TQF ^{23}Na MRS techniques could be used to monitor changes in total and intracellular bound ^{23}Na changes under muscle contraction. These techniques could potentially utilize ^{23}Na as a biomarker to study myopathies such as muscular channelopathy that is considered to be caused by genetic mutation of voltage-gated sodium channels in muscle cells (Madelin *et al.* (2014)) or disease like diabetes that is known to alter muscle microvasculature and is linked to decreased activity in Na^+/K^+-ATPase (Clausen (2003)).

- ^{23}Na MR images experience blurring and low SNR due to ^{23}Na short biexponential T_2^*. This work has demonstrated that, under the same scan time, ^{23}Na MR knee images with higher SNR can be achieved by increasing the acquisition window at only minimal blurring cost. If higher SNR is not the goal then the scan time could be reduced and still reach the same SNR as before by increasing the acquisition window. High SNR images would lead to a more accurate ^{23}Na quantification in the knee cartilage as a biomarker of the cartilage integrity

(Wheaton *et al.* (2004)). Or, a shorter scan time would lead to improved patient comfort and saving healthcare dollars.

- ^{23}Na MRI requires long scan times partly due to a large number of k-space trajectories. This work demonstrated non-Cartesian random k-space acquisition that covers the k-space with smaller number of trajectories while keeping the aliasing artifacts minimized. This acquisition scheme may be a highly desired candidate for reducing scan time.

9.2 Future Direction

- This work demonstrated the feasibility of using EMS in the study of muscle dynamics through SQF and TQF ^{23}Na MRS. This method should be used in a larger population of healthy people to ensure the consistency of the effects observed. It would be interesting to see how EMS and voluntary exercise with SQF and TQF ^{23}Na MRS results differ in subjects with pathologies such as diabetes and channelopathies. If the method proves to be sensitive to such pathologies, they could serve as an indispensable non-invasive method in assessment and treatment monitoring.

- Random k-space acquisition proposed in this work demonstrated its superior efficacy in minimizing aliasing artifacts. However, as presented, this acquisition technique does not have as high of a SNR efficiency like DA-3DPR and TPI. The next step for such an acquisition scheme is to design trajectories in such a way that sampling density is held constant. That way, it could offer an additional SNR improvement.

- Compressed sensing (CS) MRI is based on MR image reconstruction from significantly under-sampled MR measurements (i.e. k-space trajectories) (Lustig *et al.* (2007), Lustig *et al.* (2008)). Signal sparsity and random sampling are two main criteria for CS in MRI. Sodium MR images are sparse in image and spatial frequency domains. Madelin *et al.* (2012a) has already demonstrated the application of CS in sodium MRI by randomly under-sampling a 3-dimensional projection reconstruction scheme. Pseudo-random non-Cartesian k-space acquisition sampling inherently satisfies the randomness of MRI measurements. Hence, as a future work, CS could be of potential SNR improvement if utilized in conjunction with pseudo-random non-Cartesian k-space acquisition.

9.3 Conclusion

This work demonstrated how ^{23}Na MRS could be exploited to non-invasively reveal *in vivo* functional information in human skeletal muscle. It also demonstrated techniques that improve ^{23}Na MR image quality. ^{23}Na MR could play a complementary role to ^{1}H MRI in diagnosis, prognosis and treatment monitoring of a host of varying diseases since it provides uniquely different metabolic and structural information. For example, ^{23}Na MRI could be instrumental in early detection of OA by revealing the amount of sodium in articular cartilage. Also, the maintenance of a trans-membrane sodium gradient in all cells and the movement of sodium ions during neuronal or muscle activation can be explored in health and disease. However, due to long scan times and low SNR, sodium has not yet made a foothold in the clinical world. However, with the emergence of higher field whole body MRI (7 and 9 Tesla) there may be promise for bringing ^{23}Na MRI within clinically acceptable scan time requirements.

Bibliography

Andrasko, J. (1974). Nonexponential relaxation of 23 Na^+ in agarose gels. *Journal of Magnetic Resonance (1969)*, **16**(3), 502–504.

Boada, F., Gillen, J., Shen, G., Chang, S., and Thulborn, K. (1997). Fast three dimensional sodium imaging. *Magn Reson Med*, **37**(5), 706–715.

Botter, A., Oprandi, G., Lanfranco, F., Allasia, S., Maffiuletti, N. A., and Minetto, M. A. (2011). Atlas of the muscle motor points for the lower limb: implications for electrical stimulation procedures and electrode positioning. *Eur J Appl Physiol*, **111**(10), 2461–71.

Clausen, T. (2003). Na^+-k^+ pump regulation and skeletal muscle contractility. *Physiol Rev*, **83**(4), 1269–324.

Clayton, D. and Lenkinski, R. (2003). MR imaging of sodium in the human brain with a fast three-dimensional gradient-recalled-echo sequence at 4 T. *Academic Radiology*, **10**(4), 358–365.

Constantinides, C. D., Gillen, J. S., Boada, F. E., Pomper, M. G., and Bottomley, P. A. (2000). Human Skeletal Muscle: Sodium MR Imaging and Quantification—Potential Applications in Exercise and Disease 1. *Radiology*, **216**(2), 559–568.

Curtis, A. T. and Anand, C. K. (2008). Random volumetric MRI trajectories via genetic algorithms. *Journal of Biomedical Imaging*, **2008**, 6:1–6:6.

Engel, M., Benkhedah, N., and Nagel, A. M. (2015). Density-Adapted Spiral MRI sequence for ^{23}Na imaging. In *Proceedings of the 23rd Annual Meeting of ISMRM*, number 2443, Toronto, ON, Canada.

Fessler, J. A. and Sutton, B. P. (2003). Nonuniform fast fourier transforms using min-max interpolation. *Signal Processing, IEEE Transactions on*, **51**(2), 560–574.

Gobbo, M., Maffiuletti, N. A., Orizio, C., and Minetto, M. A. (2014). Muscle motor point identification is essential for optimizing neuromuscular electrical stimulation use. *J Neuroeng Rehabil*, **11**, 17.

Gurney, P. T., Hargreaves, B. A., and Nishimura, D. G. (2006). Design and analysis of a practical 3d cones trajectory. *Magnetic resonance in medicine*, **55**(3), 575–582.

Jaccard, G., Wimperis, S., and Bodenhausen, G. (1986). Multiple-quantum NMR-spectroscopy of S=3/2 spins in isotropic-phase - A new probe for multiexponential relaxation. *Journal of Chemical Physics*, **85**(11), 6282–6293.

Lauterbur, P. (1973). Image formation by induced local interactions: Examples employing nuclear magnetic resonance. *Nature*, **242**(5394), 190–191.

Levitt, M. H. (2001). *Spin dynamics: basics of nuclear magnetic resonance*. John Wiley & Sons.

Liao, J., Pauly, J., Brosnan, T., and Pelc, N. (1997). Reduction of motion artifacts in cine MRI using variable-density spiral trajectories. *Magn Reson Med*, **37**(4), 569–575.

Lustig, M., Donoho, D., and Pauly, J. M. (2007). Sparse MRI: The application of compressed sensing for rapid mr imaging. *Magn Reson Med*, **58**(6), 1182–95.

Lustig, M., Donoho, D. L., Santos, J. M., and Pauly, J. M. (2008). Compressed sensing MRI. *Signal Processing Magazine, IEEE*, **25**(2), 72–82.

Macovski, A. (1985). Volumetric NMR imaging with time-varying gradients. *Magn Reson Med*, **2**(1), 29–40.

Madelin, G., Chang, G., Otazo, R., Jerschow, A., and Regatte, R. R. (2012a). Compressed sensing sodium MRI of cartilage at 7t: preliminary study. *J Magn Reson*, **214**(1), 360–5.

Madelin, G., Babb, J. S., Xia, D., Chang, G., Jerschow, A., and Regatte, R. R. (2012b). Reproducibility and repeatability of quantitative sodium magnetic resonance imaging in vivo in articular cartilage at 3 T and 7 T. *Magn Reson Med*, **68**(3), 841–9.

Madelin, G., Lee, J.-S., Regatte, R. R., and Jerschow, A. (2014). Sodium MRI: Methods and applications. *Progress in Nuclear Magnetic Resonance Spectroscopy*, **79**, 14–47.

Maeda, A., Sano, K., and Yokoyama, T. (1988). Reconstruction by weighted correlation for MRI with time-varying gradients. *IEEE Trans Med Imaging*, **7**(1), 26–31.

Maudsley, A. A. and Hilal, S. K. (1984). Biological aspects of sodium-23 imaging. *Br Med Bull*, **40**(2), 165–6.

Nagel, A. M., Laun, F. B., Weber, M.-A., Matthies, C., Semmler, W., and Schad, L. R. (2009). Sodium MRI Using a Density-Adapted 3D Radial Acquisition Technique. *Magn Reson Med*, **62**(6), 1565–1573.

Nagel, A. M., Weber, M.-A., Borthakur, A., and Reddy, R. (2013). Skeletal muscle MR imaging beyond protons: With a focus on sodium MRI in musculoskeletal applications. In *Magnetic Resonance Imaging of the Skeletal Musculature*, pages 115–133. Springer.

Navon, G., Shinar, H., Eliav, U., and Seo, Y. (2001). Multiquantum filters and order in tissues. *NMR in Biomedicine*, **14**(2), 112–132.

Nielles-Vallespin, S., Weber, M.-A., Bock, M., Bongers, A., Speier, P., Combs, S. E., Wöhrle, J., Lehmann-Horn, F., Essig, M., and Schad, L. R. (2007). 3d radial projection technique with ultrashort echo times for sodium MRI: clinical applications in human brain and skeletal muscle. *Magn Reson Med*, **57**(1), 74–81.

Rahmer, J., Börnert, P., Groen, J., and Bos, C. (2006). Three-dimensional radial ultrashort echo-time imaging with T_2 adapted sampling. *Magn Reson Med*, **55**(5), 1075–82.

Rasche, V., Proksa, R., Sinkus, R., Börnert, P., and Eggers, H. (1999). Resampling of data between arbitrary grids using convolution interpolation. *IEEE Trans Med Imaging*, **18**(5), 385–92.

Reddy, R., Shinnar, M., Wang, Z., and Leigh, J. (1994). Multiple-quantum filters of spin-3/2 with pulses of arbitrary flip angle. *Journal of Magnetic Resonance Series B*, **104**(2), 148–152.

Rolfe, D. F. and Brown, G. C. (1997). Cellular energy utilization and molecular origin of standard metabolic rate in mammals. *Physiol Rev*, **77**(3), 731–58.

Rooney, W. D. and Springer, Jr, C. S. (1991). A comprehensive approach to the analysis and interpretation of the resonances of spins 3/2 from living systems. *NMR Biomed*, **4**(5), 209–26.

Seshan, V. and Bansal, N. (1996). In vivo ^{31}P and ^{23}Na NMR spectroscopy and imaging. In M. D. Bruch, editor, *NMR Spectroscopy Techniques*, chapter 10, pages 557–573. Marcel Dekker New York, 2 edition.

Staroswiecki, E., Bangerter, N. K., Gurney, P. T., Grafendorfer, T., Gold, G. E., and Hargreaves, B. A. (2010). In vivo sodium imaging of human patellar cartilage with a 3D cones sequence at 3 t and 7 t. *J Magn Reson Imaging*, **32**(2), 446–51.

Tsai, C. M. and Nishimura, D. G. (2000). Reduced aliasing artifacts using variable-density k-space sampling trajectories. *Magn Reson Med*, **43**(3), 452–8.

Wheaton, A. J., Borthakur, A., Shapiro, E. M., Regatte, R. R., Akella, S. V. S., Kneeland, J. B., and Reddy, R. (2004). Proteoglycan loss in human knee cartilage: quantitation with sodium MR imaging–feasibility study. *Radiology*, **231**(3), 900–5.

Winter, P. M. and Bansal, N. (2001). Triple-quantum-filtered ^{23}Na NMR spectroscopy of subcutaneously implanted 9L gliosarcoma in the rat in the presence of TmDOTP$^{5-1}$. *Journal of Magnetic Resonance*, **152**(1), 70–78.